University of Washington
Department of Civil and Environmental Engineering

ASSESSMENT OF REQUIRED ACCURACY OF DIGITAL ELEVATION DATA FOR HYDROLOGIC MODELING

Tracy Kenward
Dennis P. Lettenmaier

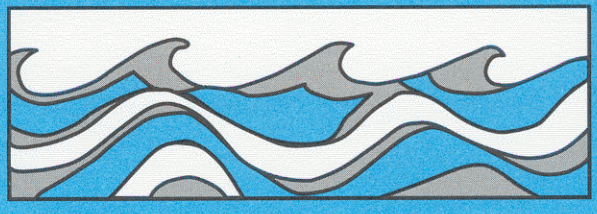

Water Resources Series
Technical Report No.153
February 1997

Seattle, Washington
98195

Department of Civil Engineering
University of Washington
Seattle, Washington 98195

ASSESSMENT OF REQUIRED ACCURACY OF DIGITAL ELEVATION DATA FOR HYDROLOGIC MODELING

Tracy Kenward
Dennis P. Lettenmaier

Water Resources Series
Technical Report No. 153

February 1997

ABSTRACT

The effect of vertical accuracy of Digital Elevation Models (DEMs) on hydrologic models is evaluated by comparing three DEMs and resulting hydrologic model predictions applied to a 7.2 km^2 USDA - ARS watershed at Mahantango Creek, PA. The highest resolution (considered to be most accurate) of the three DEMs is a 5 m product derived by automated stereocorellation from low altitude aerial photography. The other two DEMs were the standard 30 m USGS 7.5' DEM, and a 30 m DEM produced by NASA's Jet Propulsion Laboratory using interferometric processing of Spaceborne Imaging Radar-C (SIR-C) imagery. The high resolution (5 m) DEM was resampled to a 30 m resolution using a method that constrained the spatial structure of the elevations to be comparable with the USGS and SIR-C DEMs. This resulting 30 m DEM was used as the reference product for subsequent comparisons. Spatial fields of directly derived quantities, such as elevation differences, slope, and contributing area, were compared to the reference product, as were hydrologic model output fields derived using each of the three DEMs at the common 30 m spatial resolution.

A statistical analysis of the difference between the USGS and reference DEMs found that the USGS DEM had a systematic error created during the DEM production process, as well as vertical error structure related to the topographic attributes of the watersheds. The SIR-C DEM was initially 50.5 meters lower than the reference product at the basin outlet, and was therefore uniformly elevated to match the USGS basin outlet elevation. The adjusted SIR-C DEM differed from the reference DEM by -34.3 to +48.1 m over the watershed, while the range of the USGS DEM differences from the reference was -22.1 to +27.0 m. ARC/INFO algorithms were used to delineate the watershed boundaries and to determine topographic parameters from each DEM. The watershed area of the USGS DEM was within 0.04 percent of the reference product's area, while the SIR-C DEM was 3.6 percent larger. The inaccuracies in the USGS and SIR-C DEMs were apparent in the drainage network which was visible in spatial images of elevation, slope and contributing area. The valley network was poorly defined and there were more meandering drainage channels in the USGS and SIR-C DEMs as compared to the reference product.

A spatially distributed, physically based hydrologic model was used to simulate runoff production in the Mahantango Basin for the four year period beginning October 1, 1983, using each of the DEMs. Mean annual runoff volumes for simulations that used the USGS and SIR-C DEMs were 0.3 and 7.0 percent larger, respectively, than simulations produced using the reference DEM. Differences observed in direct comparisons of topographic parameters were reflected in simulated spatial distributions of depth to saturation and runoff production; specifically, these properties were much less spatially coherent in simulations that used the USGS and SIR-C DEMs as compared to the reference. There differences were in turn reflected in the shape and timing of simulated runoff hydrographs; the USGS and SIR-C DEMs produced lower peak flows and higher base flows than the reference, with the differences most pronounced for the SIR-C product.

Table of Contents

Appendices

List of Figures

List of Tables

Acknowledgments

The research described in this report is based on the Masters thesis of the first author, and was supported in part by Charles Howard & Associates Ltd., Victoria, B. C., Canada and by the National Aeronautics and Space Administration under Grant NAGW 4712 to the University of Washington. The advice of University of Washington Professors Stephen Burges and David Montgomery, who served on the first author's thesis committee, is greatly appreciated.

Thanks also go to the many people who provided the data used in this study. Mr. Terry Troutman and Dr. Bil Gburek (Pasture Systems & Watershed Management Research Laboratory, USDA-ARS, Klingerstown, PA) supplied meteorological and streamflow data. Dr. Richard White (Earth System Science Center, Pennsylvania State University) assisted us in obtaining the high resolution and USGS DEMs and corresponding metadata files from their NASA/EOS data base. Mr. Vince Caruso (Mapping Applications Center, USGS, Reston, VA) provided a description of processing of USGS DEMs. Professor Ana Barros and Mr. Rajat Bindlish (Department of Civil Engineering, Pennsylvania State University) developed the fractal interpolation scheme and provided the code based on their scheme which was used to aggregate the high resolution DEM. Dr. Eric Fielding (NASA/JPL) produced the SIR-C DEM. Messrs. Mark Zion (Princeton University) and Niko Verhoest (University of Ghent) prepared the soil and vegetation data. Mr. Eric Warner (Pennsylvania State University) provided the check-point elevations and Dr. Tom Seybert (Pennsylvania State, Wilkes-Barre Campus), provided background information on the Mahantango Basin.

1. Introduction

Developments in the acquisition, processing and storage of digital data have greatly increased the availability and reliability of digital elevation models (DEMs). The emergence of Geographical Information Systems (GISs) has provided a tool to analyze and manipulate spatial information such as DEMs, land use, soil and vegetation data. This capability has led hydrologic computer models to evolve towards spatially distributed simulations of watershed conditions based on physical processes.

Digital elevation data are widely available in the United States in different formats, resolution and accuracy. The primary source of these data is the U.S. Geological Survey's (USGS) series of one, three and 30 arc-second DEMs which are derived from digitization of contour maps and aerial photography. DEMs are also being derived by other agencies for specialized purposed from low altitude aerial photography, radar imagery, interferometry and altimetry. These new data sources combined with improved DEM production processes provides high resolution data over small areas (from low altitude aerial photography and laser altimetry) or greater spatial coverage at a lower resolution (from radar and interferometry onboard spaceborne platforms). The greater coverage of remotely sensed products is particularly advantageous for global and large-scale studies.

Distributed hydrologic models require elevation data to model topographic controls on incoming short-wave radiation, precipitation, air temperature, and downslope water movement. These data are required over a spatial grid meshed at resolutions typically in the range of 10 - 100 m. Previous studies have found hydrologic models to be sensitive to the horizontal resolution of DEMs resulting from the influence of horizontal resolution on the computed slope and hydrologic fluxes (Zhang and Montgomery, 1994; Wolock and Price, 1994). The quality of elevation data from "non-standard" sources, space and airborne sensors, such as radar and laser altimetry, brings into question how the vertical accuracy of these data will affect hydrologic predictions.

1.1 Objectives

The objectives of this thesis are:

a) to determine how the vertical accuracy of DEMs affect spatial and temporal predictions of runoff and hydrological fluxes;

b) to compare DEMs from different sources to determine the spatial structure of differences in elevation and derived topographic parameters;

c) to assess the viability of a spaceborne, interferometric-based DEM for hydrological modeling.

1.2 Approach

Three DEMs and resulting hydrologic model predictions were examined for the study site. The high resolution product is a 5 m DEM produced by Photo Sciences, under contract to Pennsylvania State University from low altitude aerial photography. The 5 m data were resampled to a 30 m resolution using a method that preserved the spatial structure of the elevations and gradients. The resulting 30 m DEM is used as the reference for comparison with two DEMs from other sources. The standard 30 m USGS 7.5' DEM and a third DEM produced by NASA/Jet Propulsion Laboratory (JPL) using interferometric processing of a pair of Spaceborne Imaging Radar-C (SIR-C) images (30 m) were compared to the reference product both in terms of directly derived quantities such as elevation differences, slope, and contributing area and indirectly through comparative evaluation of hydrologic modeling results.

Vertical errors were calculated as the difference of the USGS and SIR-C DEMs from the reference elevations. The spatial structure of the difference images were examined and systematic errors in the USGS DEM were evaluated by comparison of derived topographic parameters in light of information provided by the USGS about the DEM production process.

The Distributed Hydrology-Soils-Vegetation Model (DHSVM), is a spatially distributed, physically based hydrologic model (Wigmosta et al, 1994). It was calibrated to the Mahantango Creek

Experimental watershed as defined by the reference DEM and was used to simulate watershed conditions, state of the water table (soil moisture and depth to water table) and spatial distribution of fluxes (runoff, evapotranspiration) for a four year period using each DEM. The resulting runoff time-series and spatially distributed hydrological fluxes were compared to determine how the vertical accuracy of the topographic data affected model predictions.

1.3 Digital elevation models

Digital Terrain Models (DTMs) are ordered arrays that represent the spatial distribution of terrain attributes. Digital Elevation Models (DEMs) are a subset of DTMs that represent the spatial distribution of elevation, and hence define a topographic surface. The elevation data can be structured as a) regularly-spaced rectangular or angular grids, b) triangular irregular networks, or c) contour-based networks. The three representations are shown schematically in Figure 1.

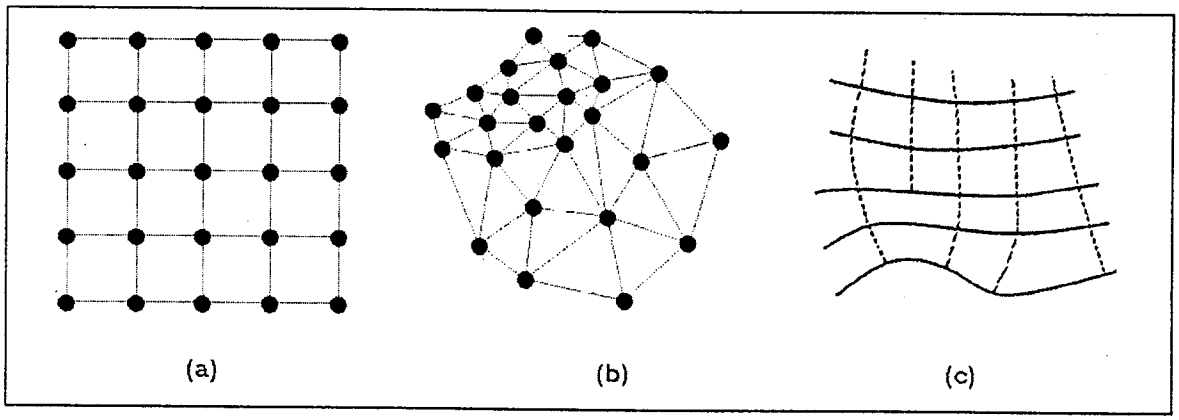

Figure 1. DEM network structure (adapted from Moore et al, 1991)

Triangular Irregular Networks (TINs) are stored as sets of x, y, and z coordinates taken at "surface-specific" locations where there are abrupt changes of slope. The neighbors of each point are also designated and the resulting surface is modeled as a set of contiguous non-overlapping triangular facets with vertices of known elevation. TINs have the advantage of representing geomorphic features with a minimum of points by retaining only the topographically relevant features. However, each point requires

the storage of the three spatial coordinates and six pointers. Pointers are required either from each sample point to all linked points or from each triangular element its three vertices and three adjacent triangles (Palacios-Velez and Cuevas-Renaud, 1986).

Contour-based networks are formed from digitized contour lines and are stored in vector form as digital line graphs (DLGs). Data are given as x, y coordinates along contour lines of specified elevation. The resulting surface is formed of irregular polygons bounded by adjacent contour lines and the orthogonal streamlines. Contour-based networks require a large amount of data storage in order to capture the non-linear behavior of the contours. From a hydrological standpoint, they are most advantageous in cases where overland flow is important, e.g. in urban areas, as contours represent equi-potential lines and the orthogonal streamlines are no flow boundaries.

Grid-based networks use a regularly-spaced triangular, rectangular or angular grids. The most widely used structures are square-grid networks in degrees (latitude and longitude) or in linear dimensions. Grid sizes range from less than 10 meters with availability for small areas, up to 10 km data, which are available globally. Grid-based networks have the disadvantage of not capturing features in the terrain that occur between grid points. This results in a loss of information as abrupt changes in elevation can not be well represented, nor can upslope flow paths that are not smooth be well represented. Further, it is difficult to determine the specific contributing area when it is not much larger than the grid cell area. A higher horizontal grid resolution reduces the impact of these problems but results in additional computational time and redundancies in areas of smoother terrain (Moore et al, 1991). Square grids are more computationally efficient and easier to implement than TINs and contour-based networks and have become the standard for data distribution and in hydrologic modeling. They are, therefore, the focus of this study.

1.3.1 Standard DEM sources

Digital elevation data for the United States are produced by the U.S. Geological Survey (USGS) as part of the National Mapping Program (USGS, 1993). USGS DEMs are available in several standard formats:

a) 30 m horizontal resolution square grid cast on a Universal Transverse Mercator (UTM) projection which covers a standard USGS 7.5 minute map series quadrangle

b) 3 arc-second angular grid which provides coverage of a 1 by 1 degree geographical block

c) 30 arc-second angular grid Digital Chart of the World (DCW) data

The 30 m resolution, 7.5 minute UTM DEMs are available for selected quadrangles, which are indicated on a graph published biannually by USGS. These data are currently available for about 70% of the conterminous U.S. and are used in hydrologic models of small to moderate size catchments. Digital elevation data are classified as Level 1, 2 or 3 depending on the data source, with Level 3 being the most accurate. Approximately 50% of the available DEMs are classified as Level 1, which are derived from automated or manual scanning of National High-Altitude Photography Program (NHAP) photographs (1:80,000 scale). The remaining DEMs are classified as Level 2 and are derived from digitizing map contour overlays (1:24,000 scale USGS quadrangle maps). Level 3 data are available only for some experimental watersheds (<1% of available DEMs) and are derived from automated scanning of National Aerial Photograph Program (NAPP) photographs.

3 arc-second DEMs for 1 by 1 degree blocks are available for all of the contiguous United States, Hawaii, and portions of Alaska, Puerto Rico, and the Virgin Islands. These data are most appropriate for hydrological modeling of 100 to 1000 km^2 catchments. Elevations are derived either from cartographic or photographic sources (1:24,000 - 1:250,000 scale). Elevations from photographic sources are derived by manual and automated correlation techniques. Elevations from cartographic sources are derived by processing digitized hypsographic features into the required matrix form and interval spacing. The 3 arc-

second production process is similar to that of the 30 m, 7.5 minute DEMs but at a coarser scale and lower resolution. The available higher resolution 30 m, 7.5 minute DEMs have been aggregated to a 3 arc-second resolution through a cooperative project between the USGS and the U.S. Defense Mapping Agency but these DEMs are currently not available to the general public.

30 arc-second DEMs with global coverage are currently being produced by the U.S. Geological Survey's Earth Resources Observation Systems (EROS) Data Center (USGS, 1996a). North America, Africa, Japan, Madagascar and Haiti are complete and available to the public by anonymous ftp; data sets for South America, Europe and Asia are under development. These data are most appropriate for macro-scale models. Applications include automated estimation of drainage networks at the continental scale (Miller and Russell, 1992) and estimation of sub-grid variation in elevation for orographic precipitation models (Leung and Ghan, 1995). Elevation data are derived primarily from the Defense Mapping Agency 1:1,000,000 scale Digital Chart of the World (DCW) contour and hydrology data. The Australian National University Digital Elevation Model (ANUDEM) was used to reconcile the DCW hydrographic information and hypsography to generate a hydrologically realistic DEM (Hutchinson, 1989). The North American DEM was derived by aggregating 3 arc-second DEMs to the desired 30 arc-second resolution.

1.3.2 Higher resolution DEMs

Higher resolution DEMs can sometimes be obtained for specific watersheds. These are developed as needed and the production and resolution of the digital elevation data are determined by the imagery available for the site.

For some experimental watersheds, aerial photography has been obtained from low altitude flights flown specifically for the purpose of collecting topographic information. Stereo-correlation photogrammetric methods can be applied to these data to produce DEMs of much higher vertical accuracy than models based on the high altitude flights of the National Mapping Program used in the standard USGS DEMs. These DEMs have the advantage of being of high vertical and horizontal resolution. The

low altitude photography must be obtained and processed into a DEM on a site specific basis, which is both costly and time-consuming.

Some experimental work has been done on construction of DEMs from satellite imagery. The European earth-observing satellite system, Satellite Pour l'Observation de la Terre (SPOT), produces stereo pairs from the parallax created by combining two images of the same area acquired on different dates. DEMs have been constructed directly from this imagery using automatic stereo-correlation, similar to the processing of manual photogrammetry. SPOT 3 is currently in orbit and will be followed by SPOT 4 which is scheduled for launching in late 1997. Most recent work has been in the development of SPOT 5 to be launched late in 2001. The specifications of SPOT 5 call for a planimetric accuracy of 10 m and an elevation accuracy of 5 m. This accuracy is compatible with conventional mapping standards at 1:50,000 scale (USGS, 1996b). Satellite imagery has the advantage of being readily available for large areas.

Aircraft and spaceborne radar imagery are currently being explored as a replacement for traditional aerial photography. Radar measures the strength and return time of microwave signals that are emitted by a radar antenna and reflected off a distant surface or object. The length of the radar antenna determines the resolution of the image in the flight direction. The longer the antenna, the finer the resolution in this direction. Synthetic Aperture Radar (SAR) refers to a technique used to synthesize a very long antenna by combining echoes received by the radar as it moves along its flight track. SAR is particularly applicable to airborne and spacecraft applications where the physical dimensions of the antennae are constrained. DEM accuracy is dependent on the navigational accuracy of the flight. Radar has the advantage that it can be used to map areas inaccessible to aerial photography due to darkness or adverse weather conditions.

Interferometric methods can be used to obtain accurate measurements of wavelengths for precise length measurements. The interferometer splits an electromagnetic beam into two parts and recombines them to form an interference pattern after they have traveled over different paths. The National Aeronautics and Space Administration, Jet Propulsion Laboratory (NASA/ JPL) has developed an aircraft

radar interferometer, Topographic Synthetic Aperture Radar (TOPSAR), that uses a synthetic aperture radar and interferometry to produce topographic maps rapidly. Interferometric TOPSAR surface maps are constructed by comparing the phase differences between radar images from two antennae mounted nearly vertically on the left side of a NASA DC-8 aircraft (Zebker et al, 1992). Elevation errors for the TOPSAR system range from 1 to 3 meters with a horizontal resolution of 5 to 10 meters.

The Spaceborne Imaging Radar-C/X-band Synthetic Aperture Radar (SIR-C/X-SAR) is an imaging radar system developed as a joint project of NASA, the German Space Agency (DARA) and the Italian Space Agency (ASI). X-SAR provides single frequency, single polarization (vertical) data, while SIR-C provides multi-frequency, multi-polarization radar data. Interferometric methods can be used to create topographic maps from the SIR-C data over very large areas. The system was flown aboard the NASA space shuttle Endeavor on flight SRL-1, shuttle mission STS-59,April 9 - 20, 1994, and flight SRL-2, shuttle mission STS-68, September 30 - October 11, 1994. An additional flight is currently being scheduled with the intention of covering 80% of the earth's surface (-60° to +60° latitude) in 11 days. Elevation errors for the SIR-C/X-SAR system range from 8 to 10 meters with a horizontal resolution of 30 meters.

TOPSAR and SIR-C/X-SAR observations are a precursor for a possible earth-orbiting SAR mounted on a satellite. One proposal, Topographic Satellite (TOPSAT), calls for two nearly identical spacecraft that would be launched and operated in tandem. The L-band (25 cm wavelength) radar system on the TOPSAT satellites would be able to acquire a global topographic map of the earth with height resolution of 2 to 5 meters for ground resolution pixels with sizes of 30 meters. Research is currently being directed towards developing a physically smaller, low power system with an inflatable antennae in the Advanced Radar Technology Program (ARTP SAR). This smaller system would be less costly than the proposal for two TOPSAT spacecrafts.

Radar altimetry mounted on board satellites such as U.S. Navy Geodetic Satellite (GEOSAT), European Remote-Sensing Satellites (ERS-1 and ERS-2) and NASA/ JPL Ocean Topography Experiment

(TOPEX)/Poseidon have been used to measure sea surface elevations (DEOS, 1996). The altimeter sends radar signals to ocean surfaces and collects the return pulse. The returned power as a function of travel time is called the waveform and provides information on the height of the satellite above the surface. Combined with a precisely computed orbital altitude, this gives the surface elevation above a well-defined geocentric reference frame. TOPEX/Poseidon is the most recent altimeter carrying satellite and is equipped with two experimental altimeters, one French and one American. The U.S.-made altimeter measures the sea surface with an accuracy claimed to be 2 cm. Measurements over water are much more accurate than over land which has the complication of vegetation coverage and differing soil types. Current applications are focused on measurements of the ocean surface and gravity anomalies but, with improving technology, satellite altimetry may be used to collect digital elevation data over land if the influence of vegetation and other surface coverage can be eliminated.

Laser altimeter systems have recently been developed to provide high-resolution, geo-located measurements of vegetation vertical structure and ground elevations beneath dense canopies. These systems can provide sub-meter accuracy measurements of earth surface topography at spatial sampling scales as small as 1 m, and typically in the 2 - 15 m range. The Scanning Lidar Imager of Canopies by Echo Recovery (SLICER) developed by NASA is one example of airborne laser altimetry (Blair and Harding, 1996). SLICER is capable of measuring both the round-trip travel time of individual laser pulses and the back-scattered laser "echoes" that are received by the altimeter. A waveform results from the reflection of a single laser pulse from multiple targets at varying heights, including returns from the highest elements of the canopy and from the ground. The waveform is digitized to provide a measure of the vertical distribution of vegetation surface area and the underlying ground's height distribution introduced by surface slope and roughness. Images are collected continuously along the flight track at a width of 20 laser beams, each of 10 - 15 m diameter. The laser footprints are geo-located by combining the laser ranging data with aircraft position, obtained from a differential kinematic Global Positioning System (GPS) trajectory, and laser pointing knowledge, obtained from an Inertial Navigation System. This

technology is currently only applicable to small study areas (typically the swath width is ~200m). It could be used as a control within a larger area when combined with elevation data from other sources.

1.4 Hydrologic modeling

Hydrologic models attempt to describe the response of a watershed to precipitation and all forms of energy input. Models differ in the way they represent the physical processes of the hydrologic cycle and the watershed characteristics, both spatially and temporally. Physical processes may be represented empirically, conceptually or explicitly. This latter modeling approach is referred to as physically based. Lumped models treat the watershed as one or more homogeneous land segments whereas distributed models explicitly represent spatial variability by dividing the watershed into a grid and modeling each grid cell individually. Models which maintain a water balance over the catchment at each time step can be used to simulate continuously over long periods of time, whereas event models simulate individual single events and require specification of initial conditions for each event.

Major developments in hydrologic modeling began in the 1960's as the advent of digital computers made hydrologic simulation computationally feasible. Earlier models were concerned with predicting water quantities, such as runoff volumes and discharges, at a catchment outlet. Models were predominantly lumped and did not address the spatial variability of hydrologic processes and catchment parameters (Moore et al, 1991).

The Stanford Watershed Model (SWM) was one of the earliest hydrologic models. It is a conceptual, lumped, continuous model. The basin may be divided into sub-areas which are simulated separately. The responses of each sub-area are combined to determine the outflow from the entire catchment. This allows some representation of spatial variations within the basin. The water quantity routines in SWM evolved into the Hydrologic Simulation Package FORTRAN (HSPF) which is maintained and distributed by the U. S. Environmental Protection Agency (EPA).

The rising popularity of water quality models in the 1970's required the ability to simulate sediment and nutrient transport within landscapes. Surface and subsurface flow characteristics, such as flow depth and velocity, are the driving mechanisms in transport models. Lumped models which do not consider the effects of topography on the hydrologic process are unable to define the spatial variability of these parameters adequately (Moore et al, 1991). Recent grid-based hydrologic models, such as the Systeme Hydrologique Europeen model (SHE) and the Distributed Soil-Hydrology-Vegetation Model (DHSVM), attempt to provide this information by using digital elevation data and spatial definitions of catchment characteristics, such as vegetation and soil type, to simulate spatially varying hydrologic processes. The response of each grid cell is simulated and then aggregated by routing flow from element to element. Behavious within each grid cell is assumed to be homogenous.

Some spatially distributed models reduce computational demands by simplifying the definitions of the hydrologic processes. TOPOG is an example of a conceptual, distributed model which simulates saturated area based on a steady state drainage condition (O'Loughlin, 1986). Indexing can also be used to avoid the complexities of a fully distributed model. Spatial variability of soil moisture is represented by the distribution function of some parameters, referred to as an index, while other parameters are lumped as a single homogeneous value (Moore and Hutchinson, 1991). The best known indexing scheme is the topographic index used by TOPMODEL (Beven and Kirkby, 1979) which results from certain assumptions, notably quasi-steady flow in the saturated zone. Because TOPMODEL has been so widely used, a brief overview is provided in the following section.

1.4.1 TOPMODEL

TOPMODEL (Beven and Kirkby, 1979) is a topographically based model which uses the probability distribution of a topographic index to represent the spatial distribution of soil moisture. This model has been widely used in hydrologic studies, including investigations on spatial scale effects, topographic effects on water quality, climate change and identification of hydrologic flow paths.

The topographic index, λ_i, is defined at each grid cell, i, as:

$$\lambda_i = \ln\left(\frac{a_i}{T_i \tan\beta_i}\right) \quad (1)$$

where a is the upslope contributing area, per unit contour length, to a grid cell, T is the soil transmissivity and tan β is the local slope angle. The index represents the tendency of flow to accumulate at any point (in terms of a) and the tendency for gravitational forces to move this water downslope (in terms of tan β as an approximate hydraulic gradient). It is used as a basis for the prediction of source areas, saturation excess, overland flow and subsurface flows.

TOPMODEL makes the critical assumption that locations within a catchment with the same topographic index are hydrologically similar. This assumption is based on the relationship between the average depth to the water table, $\bar{z}$, and a local depth, z_i:

$$z_i - \bar{z} = \frac{1}{f}\left[\lambda - \ln\left(\frac{aT_e}{T_i \tan\beta}\right)\right] \quad (2)$$

where λ is the expected value of the topographic index for the catchment, T_i is the soil transmissivity and $\ln(T_e)$ is the spatial average of $\ln(T_i)$. If the variance of the topographic index is greater than that of local transmissivity, then the predicted patterns of water table depths and resulting saturated contributing area are dependent on the topographic index.

TOPMODEL computations are distributed statistically according to the probability distribution of the topographic index. The index is discretized and a water balance is performed for each interval of the distribution. Local water-table depth is computed from the index and modified by capillary fringe effects, evapotranspiration through the root zone, and recharge through the unsaturated zone to give an estimate of the local soil moisture. Predicted hydrographs are composed of a subsurface, lumped saturated response and saturation-excess runoff generated from dynamic source areas. There is no explicit routing of either subsurface or surface flows. Predicted water-table patterns will follow the outline of the topographic index with saturated source areas expanding and contracting as the water balance of the model changes. Since

the topographic index is determined solely by the topography, all variables computed by TOPMODEL can be mapped back to a specific location (Beven and Kirkby, 1979; Quinn et al, 1995).

1.4.2 DHSVM

The Distributed Soil-Hydrology-Vegetation Model (DHSVM) was developed by Wigmosta et al (1994) to provide an integrated representation of hydrology-vegetation dynamics at the topographic scale described by digital elevation data. Unlike TOPMODEL, DHSVM is a distributed, physically based model which models each grid cell individually and explicitly routes subsurface (saturated zone) moisture between cells.

DHSVM maintains a detailed water and energy balance at each node in the grid, using a two-layer canopy model for evapotranspiration, an energy balance model for snow accumulation and melt and a two-layer rooting zone model, with a saturated subsurface flow model which explicitly predicts the lateral distribution of water. Digital elevation data are used to describe topographic controls on meteorological input data and to predict downslope water movement. At each time step, the model provides a simultaneous solution to the energy and water balance equations for every grid cell in the watershed.

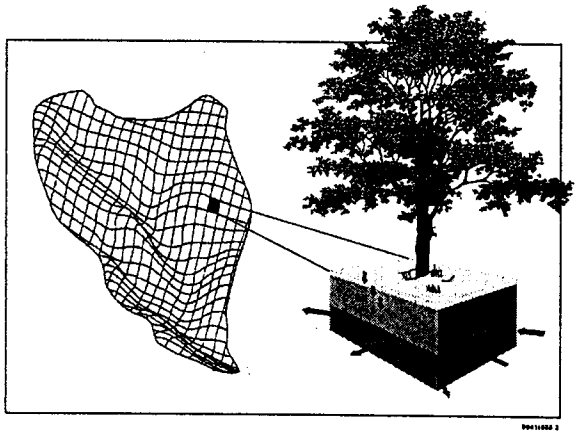

Figure 2. DHSVM representation of a land segment

Topography affects the spatial distribution of short-wave radiation due to the effects of shading, shadowing and reflection from surrounding terrain. The two-stream radiation model of Dubayah et al (1990) is used to predict the topographic effect on incoming solar radiation. Air temperature varies with elevation according to an assumed lapse rate. Precipitation can also be distributed over the basin using either a lapse rate or a more sophisticated orographic model based on air flow over topography.

Surface cover and soil properties are defined for each grid cell. The land surface can consist of overstory vegetation, understory vegetation and soil. The model calculates evaporation and transpiration independently for each vegetation layer. Evaporation of intercepted water is assumed to occur at the potential rate; transpiration from dry vegetative surfaces is calculated using a Penman-Monteith approach. The overstory is allowed to remove water from both the upper and lower soil zones while the understory can only remove water from the upper zone. The overstory and understory canopies attenuate wind speed and solar radiation based on cover density and leaf area index.

Precipitation on each grid cell is partitioned into rain or snow based on air temperature. The snowpack energy balance includes snowmelt, refreezing and changes in the snowpack heat content to compute snow temperature in a 2-layer scheme with a thin surface layer. The snowpack mass balance simulates the volume of liquid water and ice within the snowpack. Water is removed from the snowpack when the liquid phase exceeds the current liquid water storage capacity of the snowpack. The snowpack, if present, is assumed to completely cover both the understory and the soil, and to either completely cover the overstory or remain entirely below it depending on the local vegetation height. Surfaces covered by snow do not contribute evapotranspiration and radiation absorption and reflectance is based on the snow rather than the vegetation.

The soil column is modeled as a two layer rooting zone. The upper layer thickness is equal to the average rooting depth of the understory vegetation; the lower layer extends from the bottom of the upper layer to the average overstory rooting depth. All canopy throughfall and snowmelt enters the soil column where it percolates downward based on Darcy's law. Moisture may leave the soil column due to soil

evaporation (from upper zone only), overstory vegetation transpiration, understory vegetation transpiration (from upper zone only), as saturated subsurface flow, or saturated overland flow. Saturated overland flow is generated when a rising water table reaches the ground surface. In the version of DHSVM used for this study, surface runoff is routed to the basin outlet using the unit hydrograph formulation of Maidment et al (1993). Subsequent changes to the model have introduced an overland routing algorithm which imposes explicit stream channels on the DEM (Bowling et al, 1996; Nijssen et al, 1996b; Perkins et al, 1996).

Grid cells are hydrologically linked to adjacent cells through a quasi-three dimensional saturated sub-surface transport scheme which redistributes soil moisture explicitly on a pixel-by-pixel basis. Water is distributed between adjacent grid cells according to the local hydraulic gradients which are approximated by local ground surface slope slopes as calculated from the digital elevation model. A cell receives water from its upslope neighbors and discharges to its downslope neighbors. The rate of discharge is calculated as the product of the estimated soil transmissivity, ground surface slope between cells, and the width of the flow path.

Wigmosta et al (1994) describe a test application of DHSVM to the 2900 km^2 Middle Fork Flathead River basin in northwestern Montana. DHSVM has also been applied to the Snoqualmie River watershed in western Washington with modifications that incorporated an orographic model to distribute precipitation, a surface snow layer, a channel routing scheme and revised representation of vegetation affect on aerodynamic resistance under the forest canopy (Storck et al, 1995). Other applications of DHSVM include the Little Naches and Cabin Creek Basins, Washington, for the purpose of predicting the effects of forest harvest on streamflow (Wetherbee and Lettenmaier, 1996).

Detailed observations of moisture and energy fluxes at Boreal Ecosystem-Atmosphere Study (BOREAS) tower flux sites were used by Nijssen et al (1996a) to evaluate DHSVM's ability to model latent and sensible heat fluxes in the 574 km^2 White Gull Creek catchment located in Manitoba, Canada. Average seasonal heat fluxes and the diurnal cycle in the latent heat fluxes were accurately modeled. A

phase shift was observed in simulated sensible heat and net radiation flux simulation that was attributed to the soil heat flux algorithm which may not be applicable to the Boreal region. An improved soil thermal model is currently being developed to address this issue. Arola and Lettenmaier (1996) compared predictions using DHSVM to point values computed using a macro-scale equivalent model (MSE) to determine the sub-grid affects on energy and moisture fluxes at the GCM (General or Global Circulation Model) scale. Major differences were observed in predictions of snow water equivalent that were attributed to the lack of representation of topographic effects (shading and shadowing) on solar radiation in the MSE.

An on-going application of DHSVM to Hard Creek and Ware Creek, Washington (Bowling et al, 1996) investigates the effects of logging roads on overland flow. For this purpose, an overland flow routing routine has been added to DHSVM. Subsurface flow and precipitation that enters a pixel on the pre-defined stream channels is routed through the channel to the basin outlet using Muskingum routing (Nijssen et al, 1996; Perkins et al, 1996).

1.5 Investigations of the hydrologic effects of DEM resolution

Although the effect of vertical accuracy of DEMs on hydrologic predictions has received relatively little attention, the effects of horizontal resolution have been addressed in some recent studies. For instance, Zhang and Montgomery (1994) examined high resolution contour maps of two small catchments (Mettman Ridge, Oregon, 0.3 km^2 and Tennessee Valley, California, 1.2 km^2) to assess the effect of DEM horizontal resolution on topographic parameters and hydrologic simulation. DEMs of increasing grid size were constructed from the higher resolution data by averaging elevation data within the grid cell. Cumulative frequency distributions of local slope ($\tan \beta$), drainage area per unit contour length (a) and TOPMODEL topographic index, $\ln(a/\tan \beta)$, were calculated based on a steepest descent method which defines the downslope direction according to the orientation of the lowest of the eight neighboring cells. Increasing grid size resulted in a smoothing effect which decreased slopes, increased

contributing areas and increased topographic indexes. Simulations of saturated area with TOPOG, a spatially distributed model based on a steady state drainage condition (O'Loughlin, 1986), predicted increased saturation areas with increased grid size. The index based TOPMODEL (Beven and Kirkby, 1979) predicted increased peak discharges due to the increased topographic index which resulted from increased grid size. A similar study by Wolock and Price (1994) examined 71 areas in Pennsylvania and found that a coarser digital elevation data resolution was associated with higher minimum, mean, variance, and skew values of the ln ($a/\tan \beta$) distribution which tended to decrease the mean depth to the water table and increase the ratio of overland flow to total flow and the variance, skew and maximum daily flows predicted by TOPMODEL.

The effects of vertical resolution on geomorphologic parameters used in hydrologic models has been examined by Gyasi-Agyei et al (1995). High resolution DEMs of two natural and two artificial catchments were degraded to lower vertical resolution by successively truncating the last digit of the elevation data up to a vertical resolution of one meter. Geomorphologic parameters were then extracted from all DEMs and compared to determine the effects of the change in vertical resolution. The distributions of the TOPMODEL topographic index did not show any significant differences between the different DEMs although the individual pixel slope, area and topographic index did vary.

2. The Mahantango Experimental Watershed

The WE-38 watershed on Mahantango Creek, Pennsylvania (Figure 3), was chosen as the study site because of the available digital elevation data for this area. WE-38 is a U.S. Department of Agriculture - Agricultural Research Service (USDA - ARS), Northeast Watershed Research Center, experimental watershed located in Klingerstown in eastern Pennsylvania. Records of streamflow, precipitation, and daily maximum and minimum temperature at two meteorological stations date to 1967. Mahantango Creek is within the non-glaciated portion of the Appalachian Ridge and Valley Physiographic Province and is a tributary to the Susequehanna River approximately 50 km north of Harrisburg, PA.

The watershed area is 7.2 km^2 and rises from 216 to 493 meters with slopes ranging from 0° to 25.6° with a basin average of 7.7° Land use is 43% cropland, 56% forest and 1% bare surfaces. Forests are located predominantly in the northern ridges and are a mixture of oak, maple, hickory and other hardwoods. Crops rotate between corn, wheat, hay and meadow. There are no urban, industrial or mining areas within the watershed (Pionke and Kunishi, 1992).

The basin climate is temperate and humid. The watershed hydrologic budget was estimated by Pionke et al (1988) based on precipitation and streamflow measurements for 1973 to 1979. The mean annual precipitation is 1128 mm of which evapotranspiration accounts for 479 mm, surface runoff, 229 mm and baseflow, 420 mm. Runoff zones are mostly permanent grass with some pasture. All groundwater discharges to streamflow upstream of the WE-38 weir. The basin is represented by 8000 pixels on a 30 m grid in the DEM.

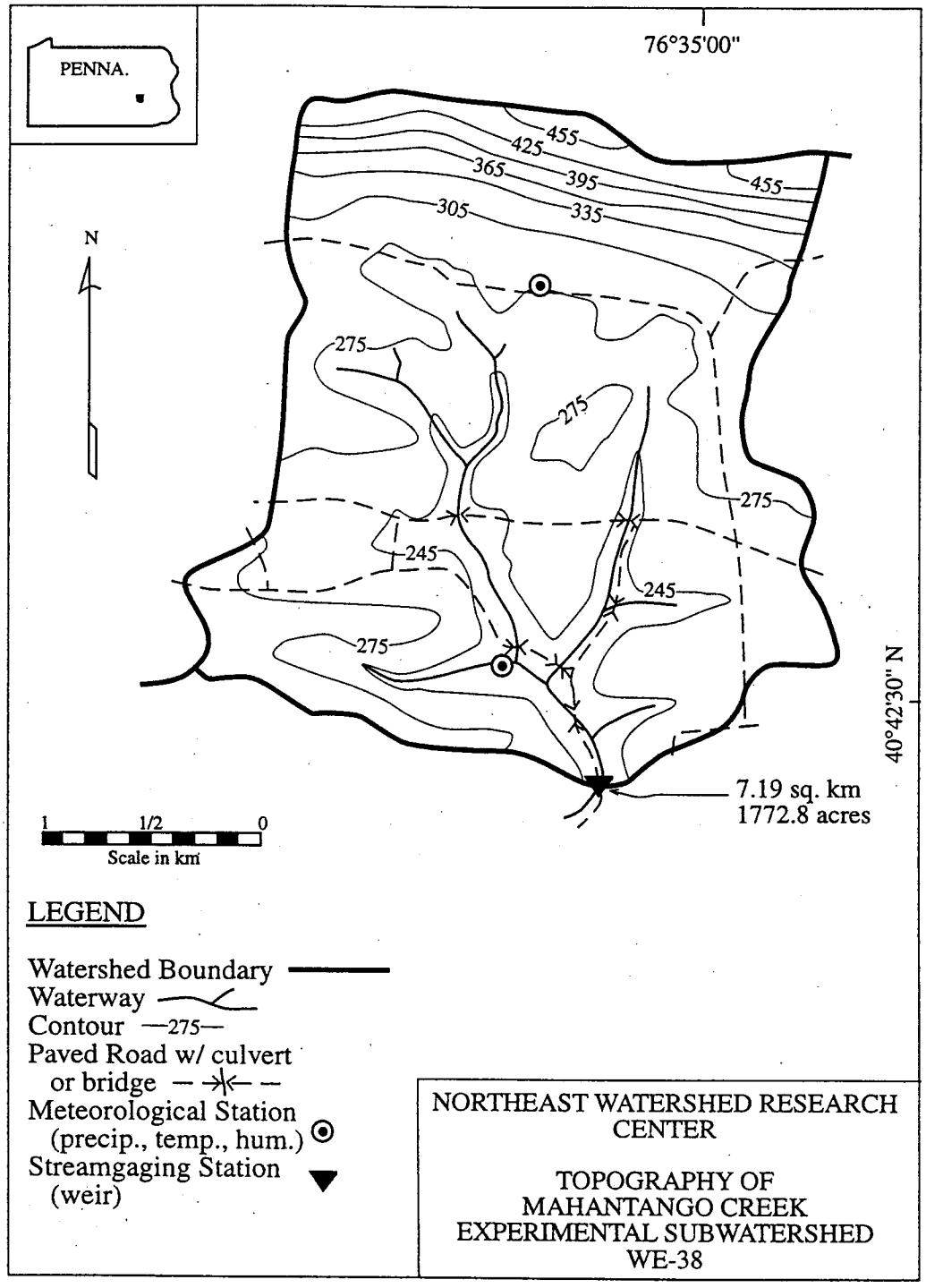

Figure 3. **Mahantango Creek experimental sub-watershed, WE-38**

The 420 km^2 Mahantango Creek Basin encompasses the WE-38 experimental watershed and is the primary research site of the Northeast Watershed Research Center, which has conducted numerous hydrologic investigations there. These studies have examined the hydrology, chemistry and geomorphology of the catchment.

The chemical and hydrologic responses of a 9.9 ha sub-area of the experimental watershed were studied by Pionke et al (1988) to determine the streamflow production mechanisms. They found that during storms, the source area cycles from (1) baseflow-dominated to (2) rainfall diluted baseflow, to (3) surface-runoff-dominated flow, to (4) progressively subsurface-discharge-dominated flow and back to (1) normal base flow in response to changes in seep zone areas and the ratio between surface runoff and seepage. This cyclic behavior was confirmed by an analysis of the chemical characteristics of the streamflow, based on P, PO_4, NO_3 and NH_4 concentrations, which reflected the characteristics of the expected dominant component of the flow. These results supported the variable source area concept which states that most surface runoff occurs from small saturated areas within the watershed where precipitation excess is generated. Source areas include seep zones which were found to be dynamic and readily generated in the Mahantango catchment, expanding substantially and quickly in response to rainfall.

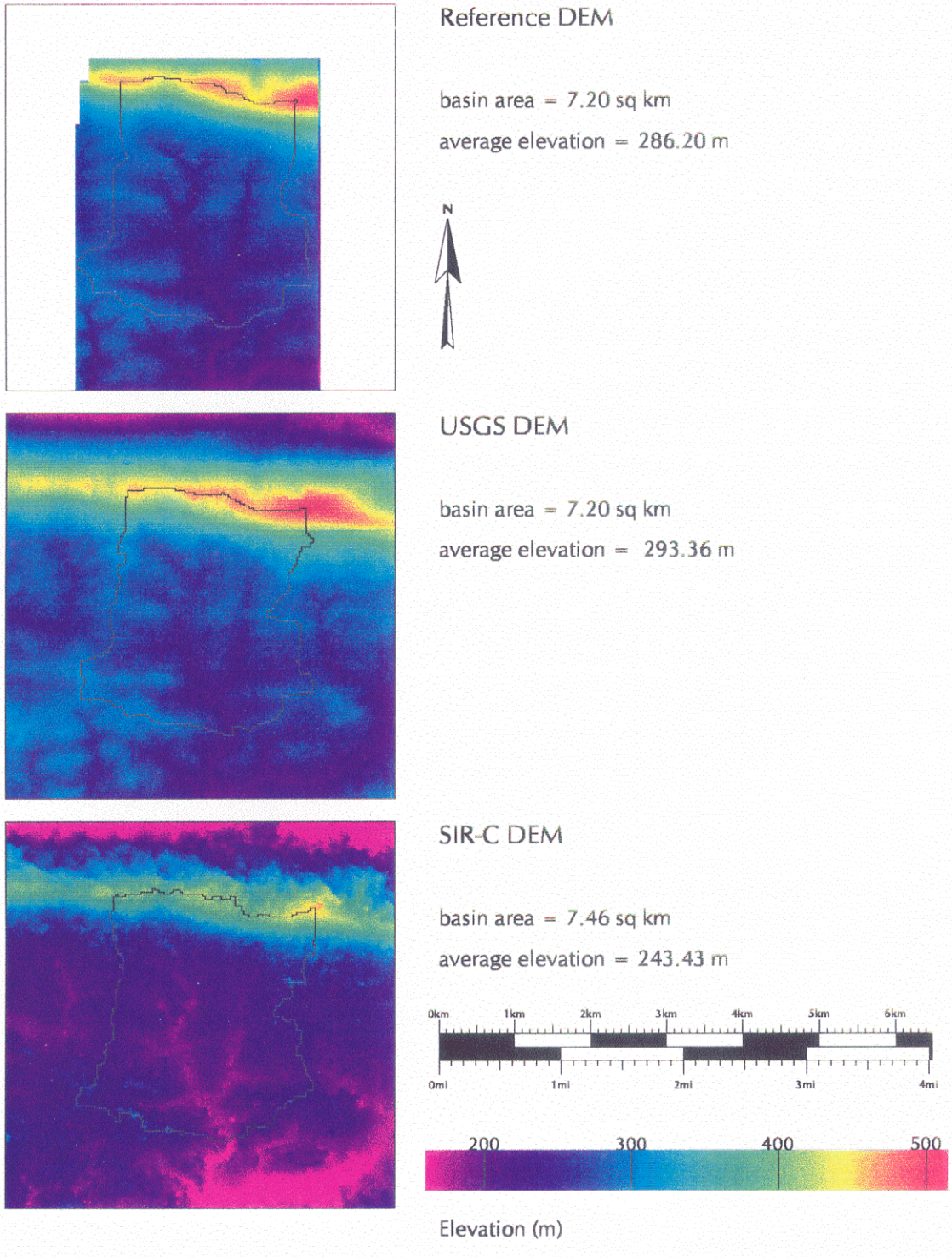

Figure 4. **Digital Elevation Models of the Mahantango Basin**

2.1 High resolution DEM

The high resolution DEM used in this study was developed by Photo Sciences, Inc. under contract to Pennsylvania State University. It was derived from aerial stereophotographs for an area roughly covering the WE-38 intensive study area. The DEM was provided at a horizontal resolution of 5 m, a vertical resolution of 0.1 m with and an estimated maximum vertical error of less than 0.5 m. Under closed vegetation canopy, which comprises 56% of catchment area, the vertical error is larger.

The aerial photographs were acquired from flights at 3600 feet above mean terrain on April 21, 1994 at a map scale of 1:4000. Kinematic GPS was used to collect high accuracy horizontal coordinates simultaneously for the center point of each photograph. Nine first order USGS bench marks in the WE-38 area were used as check points. The DEM production process used by Photo Science, Inc. is described as follows based on information provided by Richard White (1996). The photos were used as input to a Zeiss P3 analytical stereo data capture system which scanned the data in sections, creating separate models for each photo pair. Models were selected with UTM northings and eastings at multiples of 5 m and scans were performed along east-west lines separated by 15 m. Elevation values were recorded every 15 m along each scan using automated stereoplotters. Scan lines for some adjacent models were offset by 5 m relative to each other. The data were densified to a 5 m horizontal resolution to construct a common grid, using linear interpolation along each scan line and at right angles to the scan lines. Each data point represents the average grid cell elevation.

This high resolution DEM was downloaded from Pennsylvania State's EOS database (White, 1996). For the present research, the DEM was aggregated from 5 m to a coarser resolution of 30 m to construct a reference DEM that was comparable with the USGS and SIR-C DEMs as described in Section 3.2.

2.2 USGS DEM

The 30 m USGS 7.5' DEM for the Mahantango Creek watershed lies within the Valley View, PA, 7.5' quadrangle, North American Datum of 1927 (NAD-27) (Figure 5). This DEM is classified as Level 1, the least accurate and oldest of the available DEMs. Level 1 DEMs comprise 70 to 80% of current USGS 30 m products. The Valley View DEM was derived from automated scanning of quadrangle-centered photographs using the Gestalt Photo Mapper II (GPM2). The vertical resolution is 1 m with a claimed maximum absolute elevation error of 50 m and a maximum error relative to the surrounding grid cells of 21 m (USGS, 1993).

The GPM2 models are a by-product of an orthophoto production process and were originally created to register the orthophoto maps. The Gestalt Photomapping System is described in detail by Kelly et al (1977) and can be summarized as follows:

- a 47 x 52 regularly distributed grid of points is measured for each 9 x 8 mm area of each photograph, referred to as a patch
- an iterative process is used to scan and correct for parallax at each of the points within the patch
- points are compared to overlapping areas of previous patches (20-50%) to ensure edge-matching
- parallax values are converted to ground heights with corresponding horizontal coordinates
- patches are combined to cover a USGS 7.5' quadrangle and are regridded to the standard format
- DEMs are smoothed to remove any large edge effects

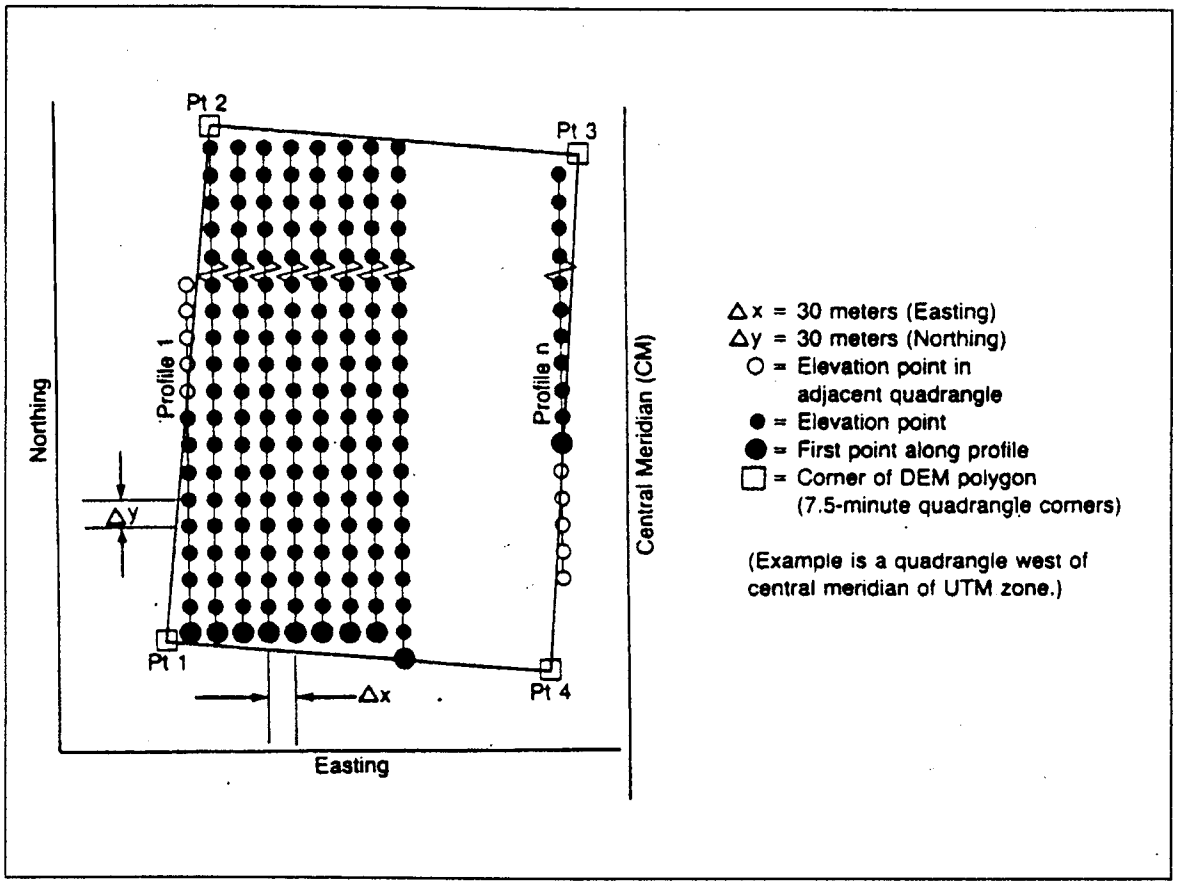

Figure 5. **Structure of a 7.5' USGS DEM, 30 m UTM grid (USGS, 1993)**

2.3 SIR-C based DEM

A third DEM was provided by Eric Fielding (NASA/JPL) based on a pair of SIR-C images that were collected onboard the NASA space shuttle Endeavor on October 8 & 9, 1994. The shuttle flew at an altitude of 215 km in a circular orbit and a 57 degree inclination. The SIR-C antenna is composed of two planar arrays of radiators for each frequency (L-band, 23.5 cm, and C-band, 5.8 cm). Each array receives vertically- and horizontally-polarized transmitted waves so that images of the magnitude of radar backscatter are acquired in four polarization combinations: HH (Horizontally-transmitted, Horizontally-received), VV (Vertically-transmitted, Vertically-received), HV, and VH.

The average of three polarizations (HH, HV and VV) was used to develop the Mahantango DEM. The use of multiple polarizations reduces the noise in the finished product. Interferometric methods were used by NASA/JPL to process the data using PCI software, a commercial product. Vertical control points were selected from the Mahantango USGS 3 arc-second DEM and the horizontal control points were taken from the 30 m USGS 7.5' DEM . The SIR-C DEM is a preliminary product that was provided for the purposes of this research.

3. Horizontal Aggregation

It was necessary to aggregate the high resolution DEM from a 5 m to 30 m horizontal resolution to create a reference DEM that was comparable with the USGS and SIR-C 30 m DEMs. Several methods were considered for accomplishing the aggregation and these are discussed briefly below.

3.1 Standard methods

The simplest resampling approach is to average the elevations contained within a coarser grid cell. This method preserves the overall volume of topographic features but suppresses peaks and valleys, resulting in a smoothing effect. The 5 m WE-38 DEM was aggregated by averaging for comparison with other methods.

A more sophisticated method known as envelope orography attempts to reduce the smoothing effect of averaging by adding an increment to the averaged grid elevation. This increment is defined as a constant multiplier of the sub-grid-scale standard deviation of the higher resolution elevation data about their mean. For an idealized two-dimensionally sinusoidal mountain range, an increment of 2.0 times the sub-grid standard deviation will raise the averaged height to the original peak elevation (Wallace et al, 1983). Envelope orography has the advantage of being resolution dependent, i.e. finer horizontal resolutions are associated with smaller increments. While this method captures topographic peaks, low elevation plains and valleys are not well modeled and total orographic volume is not preserved.

3.2 Fractal interpolation scheme

Bindlish and Barros (1996) proposed a modified fractal interpolation scheme to aggregate topographical data while preserving the spatial structure of the elevations and orographic gradients. The 5

m high resolution DEM was aggregated using this scheme as implemented in computer code developed by Bindlish and Barros as follows:

- the topographic data were converted from the spatial domain to frequencies and corresponding amplitudes in the Fourier domain using a Fast Fourier Transform (FFT) algorithm
- the fractal dimension, D, and roughness coefficient of the 5 m data were calculated from the slope and intercept of the log-log plot of the mean power spectral density function respectively, as discussed in Appendix A
- a Brownian random surface was created at a 5 m resolution and transformed to match the fractal dimension and roughness factor of the high resolution DEM
- the transformed Brownian surface was used as a weighting function to aggregate the 5 m DEM to a 30 m resolution
- a correction term based on the standard deviation of the elevations was added to the 30 m DEM

The use of 2D Fourier transforms requires that the data be structured in an n x n grid of order 2 ($n=2^m$). The extent of such a matrix over the entire research watershed also included areas outside of the watershed where high resolution digital elevation data were not available. Two methods of grid extraction were tested, filled area and piecewise aggregation.

3.2.1 Filled area method

The filled area method aggregated the digital elevation data over the smallest n x n matrix of order 2 that gave full basin coverage. A 1024 x 1024 matrix was found to encompass the entire WE-38 watershed. The grid cells within this matrix that were outside the available data were filled with artificial data. Two fill values, zero and the average elevation of the basin, were tested to determine the effect of the selected fill value on the final DEM. The fractal dimension and roughness coefficient were calculated

from the largest matrix of order 2 that would fit within the available digital elevation data, a 512 x 512 pixel area (Figure 6).

Results of the two resamplings were compared to determine effects of the fill value. Elevations varied only at the edges of the DEM coverage area and did not effect elevation data within the basin. A fill value of zero was selected for the final resampling.

3.2.2 Piecewise aggregation method

An alternative method to filling a large matrix with artificial data was to separate the available digital elevation data into smaller n x n matrices of order 2. Four 128 x 128 pixel areas and six 256 x 256 pixel areas were required to cover the watershed area (Figure 6). The fractal dimension and roughness coefficient were calculated for each piece from the high resolution digital elevation data and used to aggregate from 5 to 30 meters using the fractal interpolation method. The resulting pieces were joined to produce a DEM that covered the entire watershed.

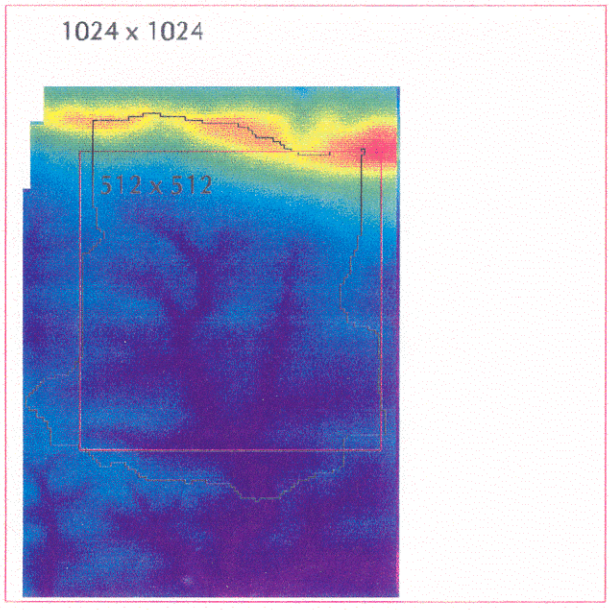

Filled Area Aggregation

1024 x 1024 area aggregated with fractal D of 512 x 512

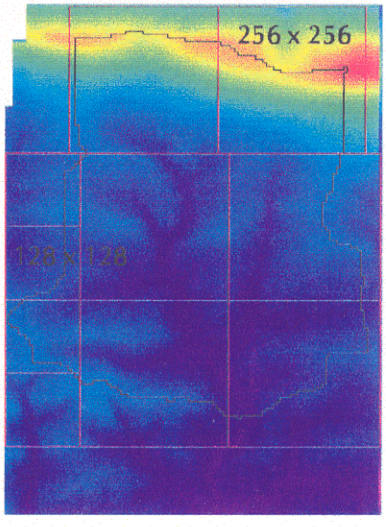

Piecewise Aggregation

each 256x256 and 128x128 segment is aggregated based on its own fractal D

Elevation (m)

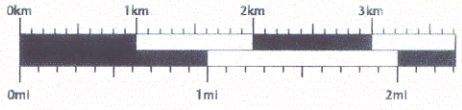

Figure 6. Data Matrices used during fractal aggregation

3.2.3 Sensitivity analysis

The fractal dimension, D, of the data can be calculated by power spectrum analysis. D is determined from the slope of the linear portion of the log-log plot of the power spectral density against the radial wave number (Bindlish and Barros, 1996). The power spectrum for the 512 x 512 pixel sub-area used in the fractal aggregation of high resolution DEM is shown in Figure 7. As the definition of the linear portion of this curve is imprecise, D depends on the interpretation of the spectrum.

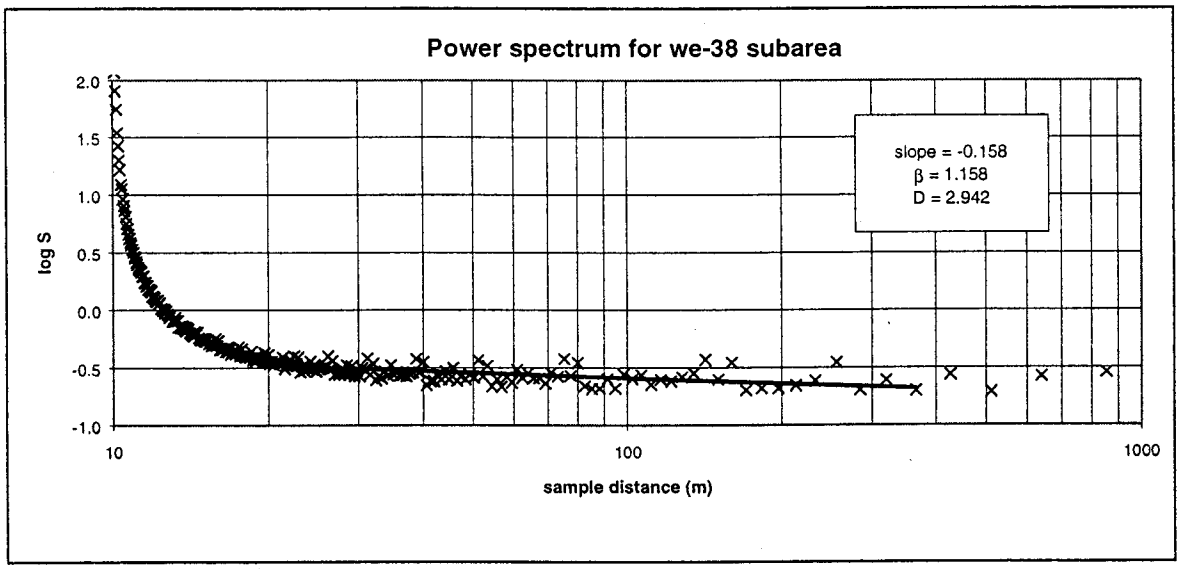

Figure 7. Power spectrum for Mahantango Creek research watershed sub-area

A 256 x 256 pixel sub-area at the southeast corner of the basin was repeatedly resampled to a coarser resolution using a range of fractal dimensions to determine the sensitivity of the fractal interpolation method to this parameter. The high resolution data in this sub-area were found to have a D of 2.785. Data were aggregated using fractal dimensions of 2.0, 2.5, and 3.0. Differences between the aggregated elevations due to the change in D ranged from -0.1 m to +0.1 m, as displayed in Table 1. Larger changes to the fractal dimension resulted in elevation differences in more grid cells although these differences were small (±0.1 m).

Table 1. Sensitivity of fractal interpolation to fractal dimension, D[1]

Fractal Dimension	*-0.1 m <=ΔEL <= 0.0 m*	*0.0 m<= ΔEL <= +0.1 m*
2.0	0.80 % of grid cells	0.63% of grid cells
2.5	0.26% of grid cells	0.28% of grid cells
3.0	0.40% of grid cells	0.55% of grid cells

The roughness coefficient is determined from the value of the power spectral density at a frequency of 1 cycle/pixel and represents the average squared amplitude. Changes to the roughness coefficient result in a raising or lowering of the surface that is used as a weighting function. This does not affect the aggregation of high resolution to a coarser resolution.

3.3 30 m reference DEM

The two methods of applying the fractal interpolation scheme, filled area and piecewise aggregation, gave similar results except at the edges of matrices used in the piecewise method. The edge effect could be reduced by overlapping the segments and discarding the outer portion of each area.

Aggregation using the fractal scheme has the advantage of maintaining the continuity of topography over the basin but may result in some smoothing as local changes in topographic structure may not be captured. The piecewise area approach is more cumbersome and errors in the estimation of the fractal dimension and roughness based on amplitudes and frequencies calculated with FFT algorithm become larger for smaller matrices. For this reason, the filled area method was chosen to aggregate the 5 m high resolution DEM to a 30 m reference DEM for comparison with the USGS and SIR-C 30 m DEMs.

---

[1] Differences are the aggregated elevation based on the indicated fractal dimension, D, less the results of the resampling with a D of 2.785

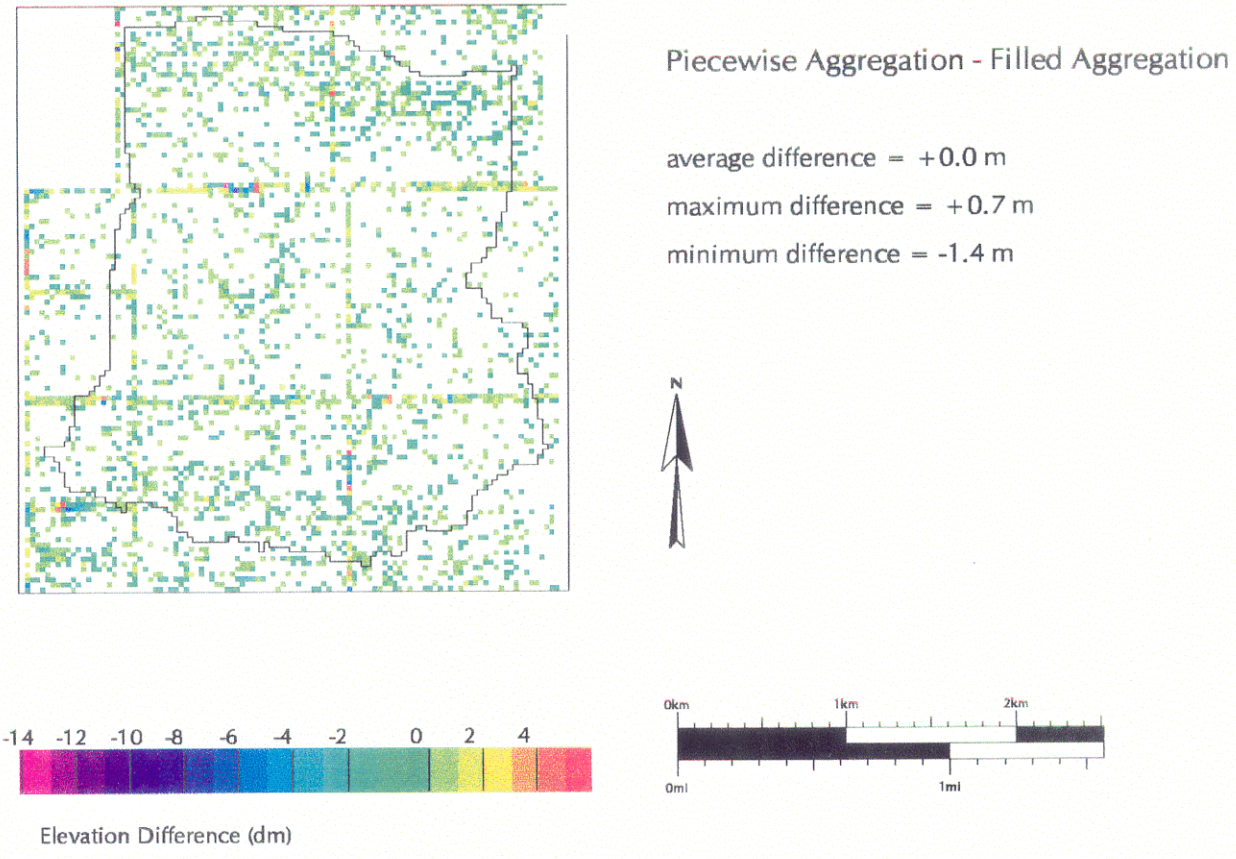

Figure 8. **Elevation differences due to fractal aggregation method**

4. DEM Comparison

The reference, USGS and SIR-C DEMs were compared to determine the range and nature of their differences. Elevation and elevation-dependent topographic parameters were examined numerically and spatially. A number of programs are available for digital terrain analysis and can be used to calculate basin topographical parameters. The Geographical Resources Analysis Support System (GRASS) of the U.S. Army Construction Engineering Research Laboratories (USACERL) and ARC/INFO, a commercial production available from Environmental Systems Research Institute, Inc. (ESRI) are two such programs.

4.1 Watershed extent and outlet

ARC/INFO algorithms were used to determine the watershed area and the elevation of the basin outlet as defined by each DEM. The DEMs were first checked for pixels which did not drain (sinks), which were eliminated by elevating the sink pixels. DEMs which have been processed to remove sinks are subsequently referred to as "filled" to distinguish them from the raw products. Flow direction and contributing area were also calculated as discussed in Section 4.4.

The outlet of the Mahantango Creek experimental sub-watershed is USDA-ARS weir WE-38, located at 365,856.0 E, 4,507,017.5 N, meters UTM. The outlet in each DEM was selected as the pixel that was closest to the known location of the weir and on the stream channel as represented in the DEM. Outlet and basin average elevations for the SIR-C DEM (Table 2) indicated that the datum for this DEM was apparently inconsistent with the USGS and reference DEM datums. Discussions with Eric Fielding (NASA/JPL) suggested that the vertical datum for the checkpoints used in the SIR-C DEM production (WGS72) does not correctly align with the NAVD29 vertical data used for the USGS DEM. To resolve this difference, all values in the SIR-C DEM were elevated by 50.5 m, the difference in basin outlet elevation between the SIR-C and reference DEMs.

The filled USGS DEM and the filled and elevated SIR-C DEM were used for all subsequent DEM comparisons with the reference DEM and for the hydrologic simulations.

For each DEM, drainage area was determined as the contributing area upstream of the outlet. For the USGS and reference DEMs, the drainage areas agreed to within 0.04%. The SIR-C DEM resulted in a 3.6% larger drainage area than the reference DEM.

Table 2. Watershed area and elevation

	Reference DEM	*USGS DEM*[2]	*SIR-C DEM*[3]
Drainage Area	7.20 km^2	7.20 km^2	7.46 km^2
Sinks Filled	5 pixels	110 pixels	358 pixels
Outlet Elevation	215.9 m	238.0 m	215.9 m
Average Elevation	286.2 m	293.7 m	294.3

Visual inspection of the DEMs reveals deficiencies in the USGS and SIR-C DEMs (Figure 9). The reference DEM produces a sharp image that clearly defines the valley network whereas the USGS and SIR-C images at the same 30 m resolution appear more scattered. The watershed boundaries differ considerably between the three images, becoming more irregular as the vertical resolution decreases. The basin delineation differs the most on the east side of the basin where a sharp notch in the USGS and SIR-C DEMs appears as a round bay-like shape on the reference DEM.

[2] Values are based on the filled USGS DEM

[3] Values are based on the filled and elevated (+50.5 m) SIR-C DEM

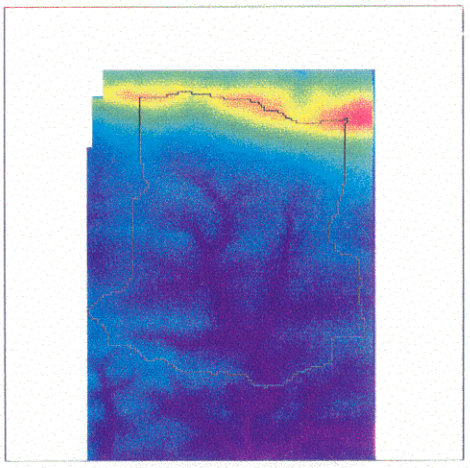

Reference DEM

basin area = 7.20 sq km

average elevation = 286.2 m

outlet elevation = 215.9 m

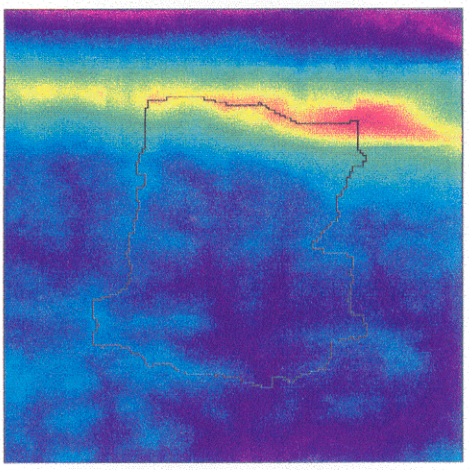

Filled USGS DEM

basin area = 7.20 sq km

110 sink pixels filled

average elevation = 293.7 m

outlet elevation = 238.0 m

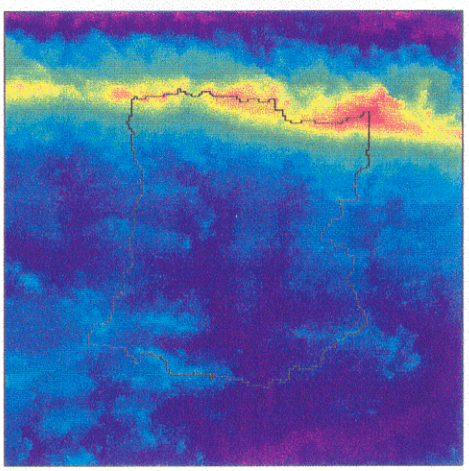

Filled & Elevated SIR-C DEM

basin area = 7.46 sq km

358 sink pixels filled

average elevation = 294.3 m

outlet elevation = 215.9 m (forced)

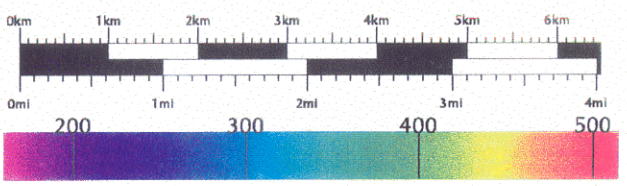

Figure 9. Adjusted Digital Elevation Models

4.2 Elevation check points

Nine check points were acquired from the WE-38 study area to obtain an estimate of the point elevation error of the DEMs. The horizontal positions of the check points were established with GPS by Eric Warner (Pennsylvania State University), using a Trimble receiver and differential correction with data from an established base station. This permitted an x, y accuracy of approximately 2.5 m.

Vertical elevations at the check points were surveyed with a Sokkia Set 4BII total station (Warner and Troutman, 1996). The station uses an active ranging system between the generating source at the station and the prism located above the point of interest. The system can theoretically determine elevation differences of less than 0.01 m. The elevation measurement for the ground control is limited by the quality of the USGS benchmark elevations used as initial points. These benchmarks are accurate to about 0.1 m in the vertical.

Table 3. Check point descriptions (taken from Warner and Troutman, 1996)

Point	*Easting m UTM*	*Northing m UTM*	*Description*
1	365921.8	4507831.3	gully North of Y
2	365774.5	4507102.1	driveway near weir
3	365479.1	4507193.6	near trees on hill
4	366777.1	4507760.9	North power pole
5	365369.2	4509311.2	West of Line Mt. Rd Y
6	364453.9	4509517.9	North West corner, Tree line
7	365675.1	4507427.3	Y intersection
8	366779.3	4507661.3	South pole
9	366364.4	4509095.5	Line Mt. Rd Y

Table 4. Check point elevations

Point	*Surveyed elevation*[4] *(m)*	*High resolution 5 m DEM*	*Reference 30 m DEM*	*USGS filled*	*SIR-C filled and elevated*
1	232.03	232.3	231.8	238	236.1
2	223.37	222.9	224.0	238	225.5
3	266.60	267.0	264.3	267	242.7
4	260.20	259.3	259.4	263	270.2
5	282.36	282.7	281.4	282	272.1
6	284.12	297.2	297.1	306	300.8
7	225.94	229.1	227.5	238	241.8
8	268.35	268.2	269.6	270	283.3
9	283.77	283.9	283.4	285	290.5

Differences between the surveyed elevations and those in the corresponding grid cell of each DEM are displayed in Table 5. Elevations are within 1.0 m of the WE-38 5m DEM except for points 6 and 7. Point 6 was located at the tree line and errors may be due to photogrammetric difficulties in determining the ground elevation next to the canopy. Point 7 was on a roadway and should not have been difficult to locate.

The 5 m DEM is more accurate when compared to point elevations than the coarser resolution DEM although the errors are only slightly larger for the reference DEM as compared to the 5m high resolution product. The reference digital elevation data are significantly closer to point elevations than either the USGS or the SIRC-C DEMs.

[4] Check point elevations taken from Warner and Troutman, 1996.

Table 5. Elevation differences in meters at check points

Point	*Surveyed Elevation (m)*	*High resolution 5 m DEM*	*Reference 30 m DEM*	*USGS filled*	*SIR-C filled and elevated*
1	232.03	0.3	-0.2	6.0	4.1
2	223.37	-0.5	0.6	14.6	2.1
3	266.60	0.4	-2.3	0.4	-23.9
4	260.20	-0.9	-0.8	2.8	10.0
5	282.36	0.3	-1.0	-0.4	-10.3
6	284.12	13.1	13.0	21.9	16.7
7	225.94	3.2	1.6	12.1	15.9
8	268.35	-0.2	1.3	1.6	15.0
9	283.77	0.1	-0.4	1.2	6.7
	mean absolute difference	2.1	2.3	6.8	11.6
	mean difference	1.8	1.3	6.7	4.0
	standard deviation	4.4	4.5	7.8	13.5

4.3 Spatial Elevation Differences

Elevation differences were calculated between the reference DEM and either the USGS DEM or the SIR-C DEM on a pixel-by-pixel basis. It is assumed in this study that the reference DEM is representative of the true elevations on the watershed and that the differences are due to the errors in the lower accuracy products. Differences are displayed spatially in Figure 11 and as frequency distributions in Figure 12 and Figure 13. The range of SIR-C differences was greater than those of the USGS DEM. The mean difference was lower but this is artificial as the SIR-C elevations were forced to agree with reference

DEM at the basin outlet. The USGS differences display a spatial pattern which is investigated in detail in Section 5.

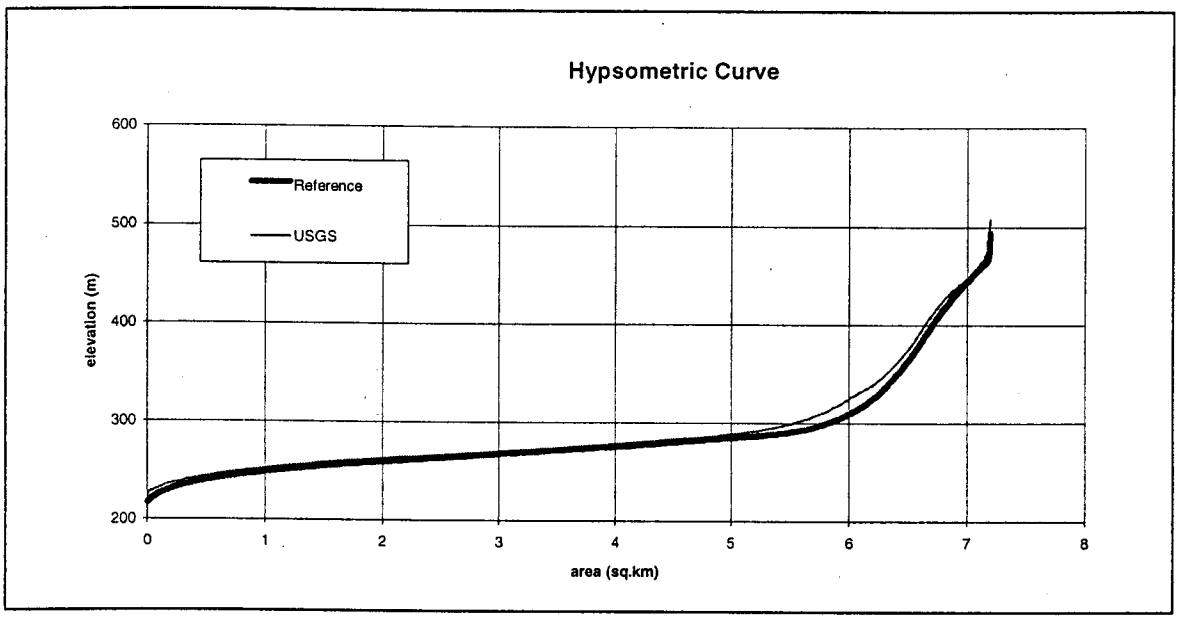

Figure 10. Mahantango basin hypsography

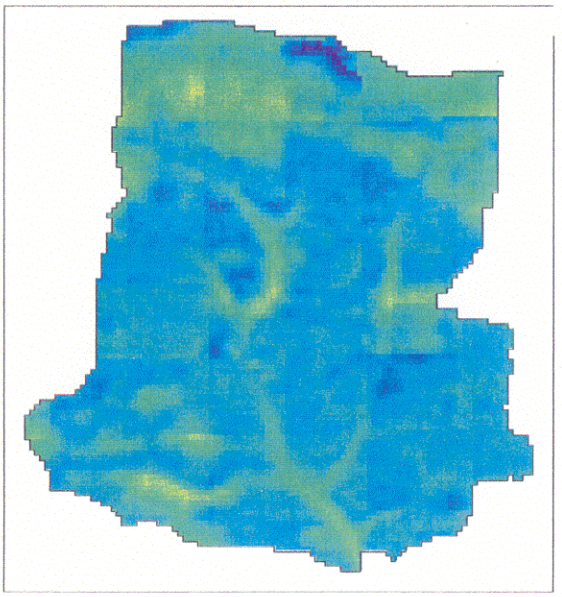

Filled USGS - Reference

average difference = +6.0 m

maximum difference = +27.0 m

minimum difference = -22.1 m

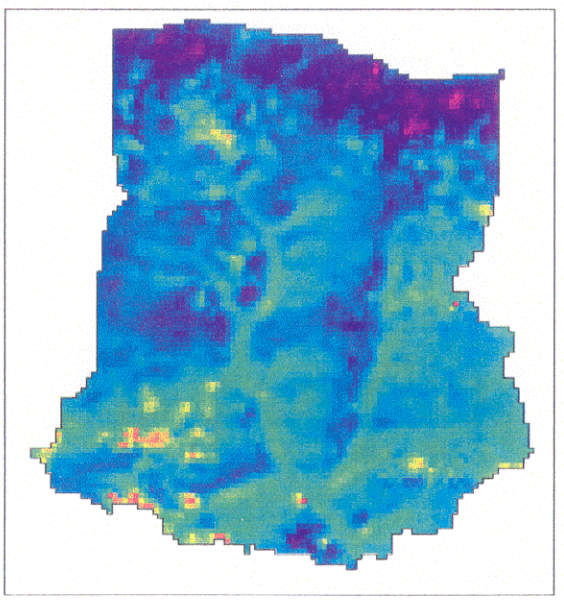

Filled & Elevated SIR-C - Reference

average difference = +1.0 m

maximum difference = +48.1 m

minimum difference = -34.3 m

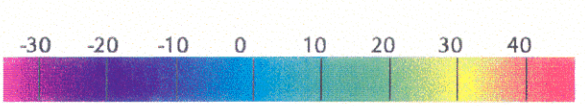

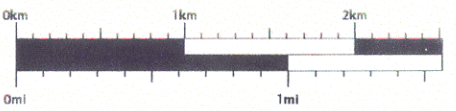

Figure 11. Spatial distribution of elevation difference

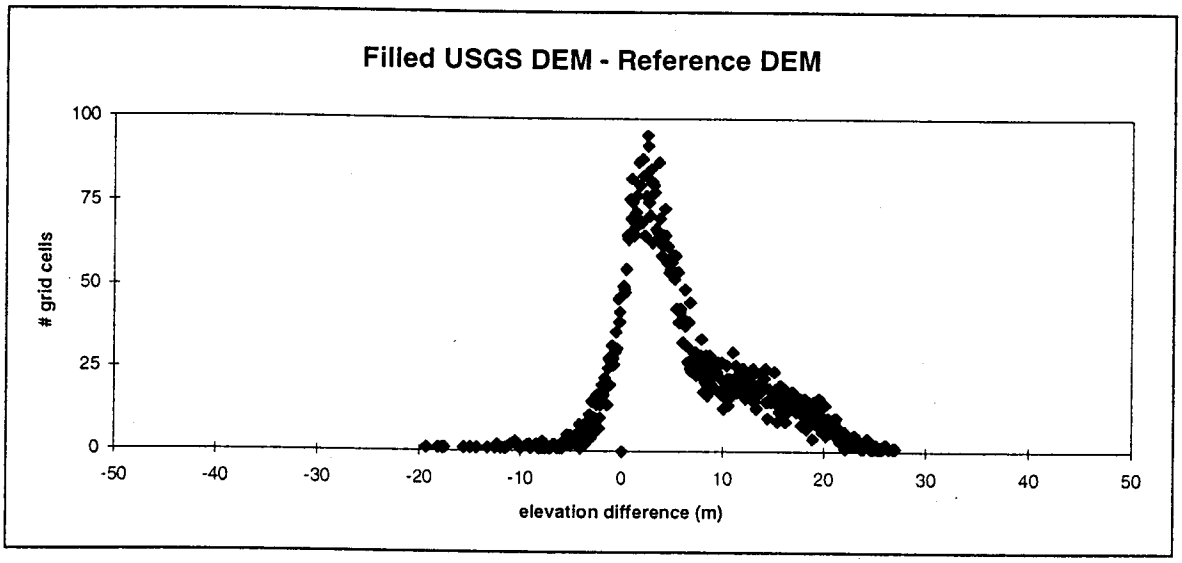

Figure 12. USGS elevation differences

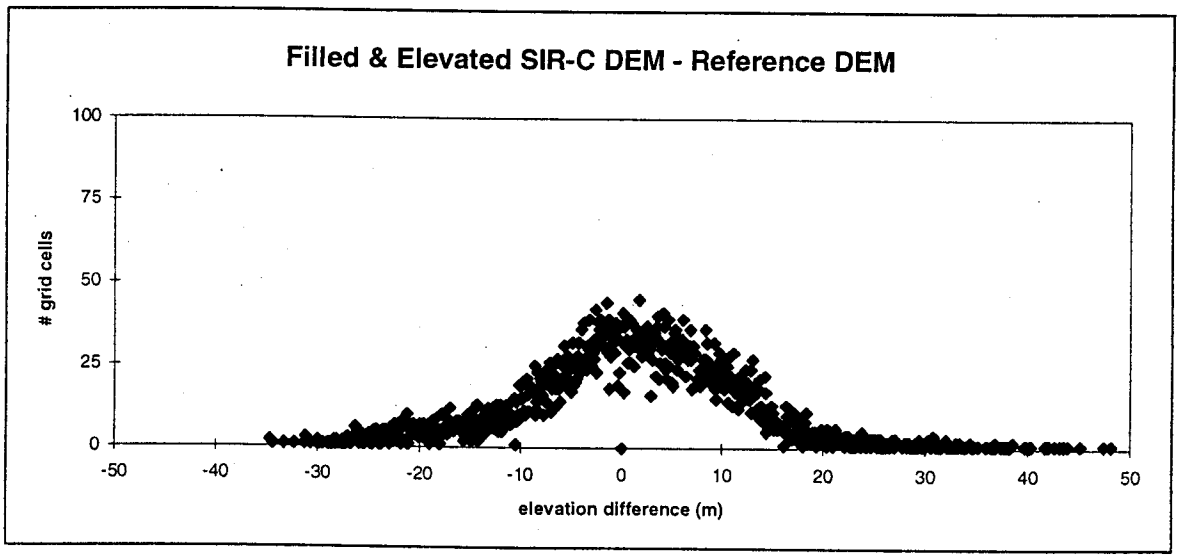

Figure 13. SIR-C elevation differences

4.4 Topographic Parameters

Topographical attributes such as slope, aspect, specific catchment area (upslope area draining across a unit width of contour), aspect, flow path length and profile curvature can be calculated directly from the DEM or from a surface fitted to the point elevation data. The TOPMODEL topographic index (see Section 1.4.1) was calculated from the elevations as it combines slope and drainage patterns, and is related to hydrological behavior.

Many algorithms have been suggested to calculate slope and contributing area. These methods can result in substantially different spatial and statistical distributions. Contributing area depends on the direction of flow from each pixel. Single flow direction algorithms distribute flow from each pixel to one of the eight adjacent cells, usually selected by the steepest descent method which directs flow to the lowest neighbor. Quinn et al (1991) suggested a multiple direction algorithm which weights the distribution of flow between all adjacent, downslope cells by the gradient of each downhill flow path and contour length. A more detailed approach, suggested by Costa-Cabral and Burges (1994), traces the two dimensional, aspect driven flow over the surface. If a flow line enters a pixel then all cells it has previously passed through are defined to be topographically upstream from the pixel and are included in calculation of the total contributing area to the pixel.

Slope, contributing area and topographic index were calculated for the reference (30 m aggregated high resolution), filled USGS and filled and elevation adjusted SIR-C DEMs using ARC/INFO algorithms as displayed in Figure 14 -Figure 21. The ARC/INFO algorithm calculates slope based on the method of steepest descent. The USGS and SIR-C DEMs exhibited larger ranges in slope than the reference DEM. The USGS DEM resulted in parameters that were closer to the reference product than the SIR-C DEM. The differences were apparent in spatial images of the topographic parameters. The valley network seen in the slope image is much more defined in the reference DEM than in the USGS product, and both are more clearly defined than the SIR-C DEM. The SIR-C image appears to be scattered,

resulting from abrupt changes in elevation. The drainage network defined by contributing area is more meandering than with the other DEMs. Differences in topographic index were mainly at the lower end of the distribution, which is not as hydrologically significant because the associated areas produce saturation excess relatively infrequently.

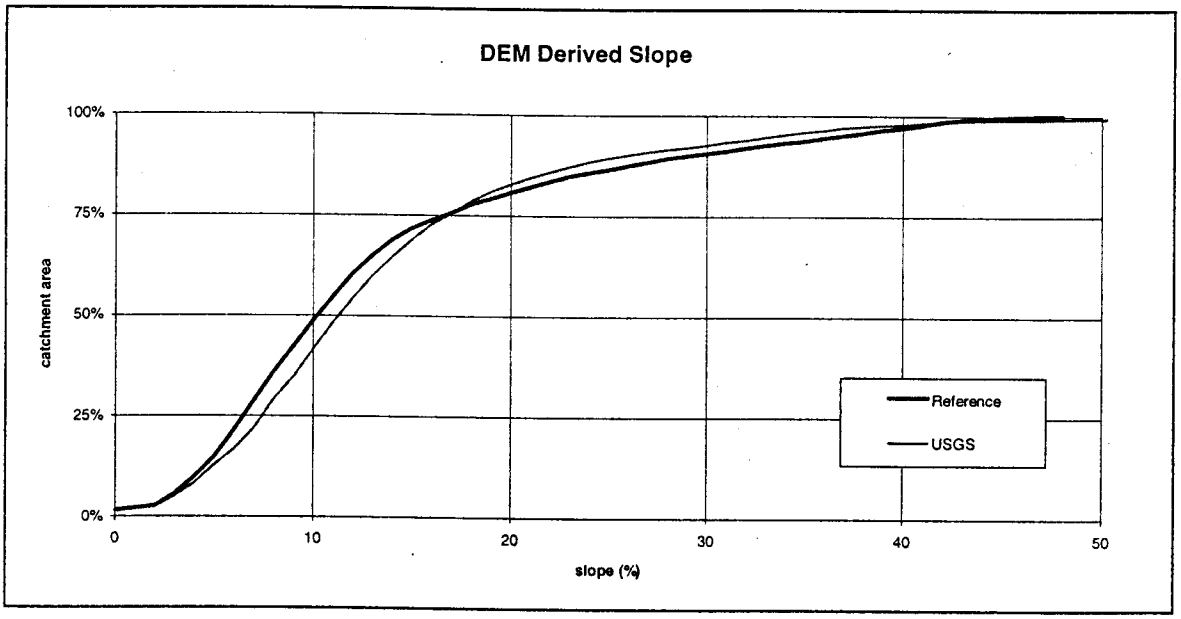

Figure 14. Cumulative distribution of slope

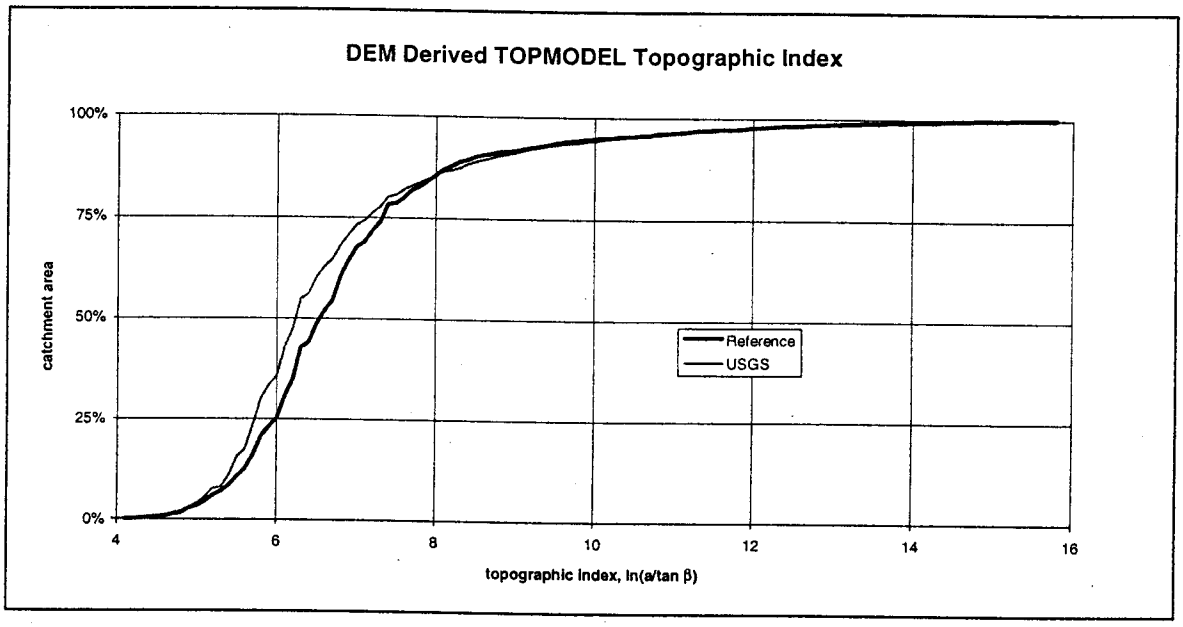

Figure 15. Cumulative distribution of topographic index

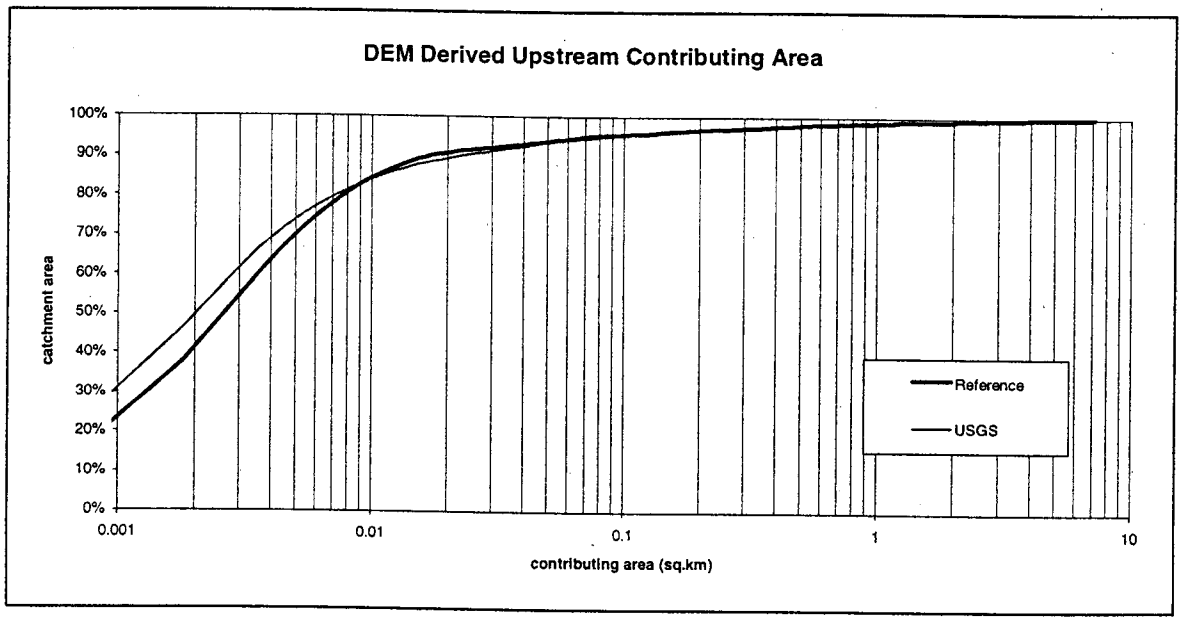

Figure 16. Cumulative distribution of contributing area

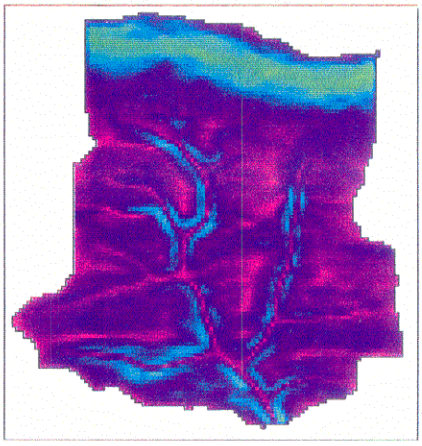

Reference Slope

maximum slope = 25.6 degrees

average slope = 7.7 degrees

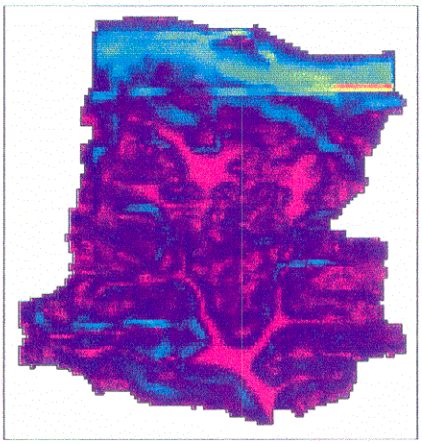

USGS Slope

maximum slope = 38.2 degrees

average slope = 7.5 degrees

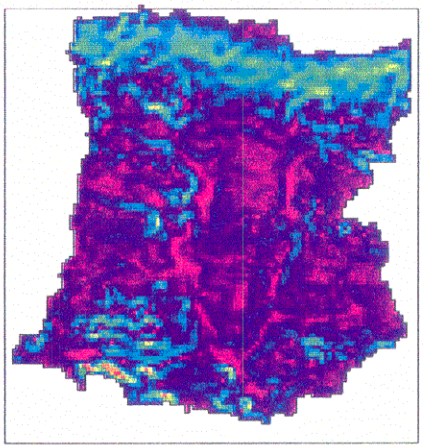

SIR-C Slope

maximum slope = 39.2 degrees

average slope = 8.9 degrees

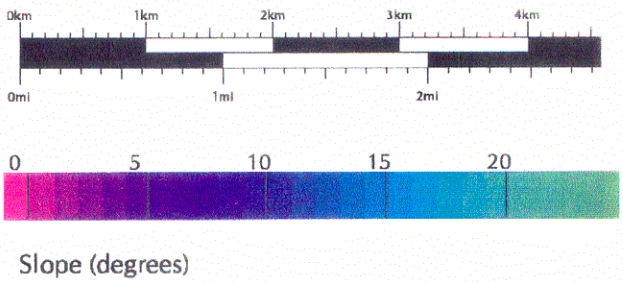

Figure 17. Spatial distribution of slope

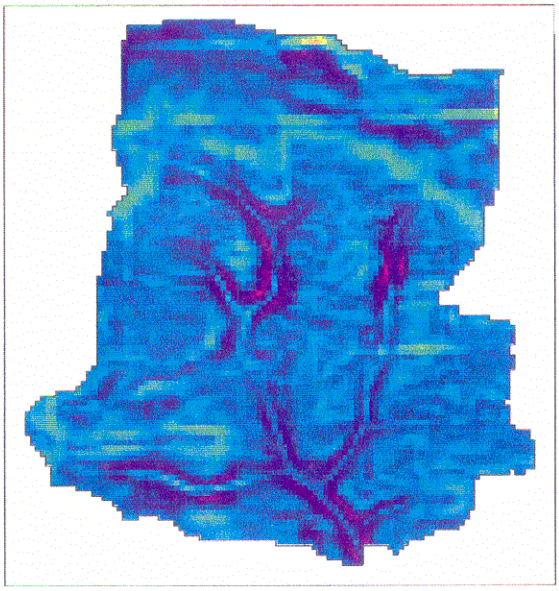

USGS slope - Reference slope

average difference = -0.3 deg

maximum difference = +22.1 deg

minimum difference = -16.1 deg

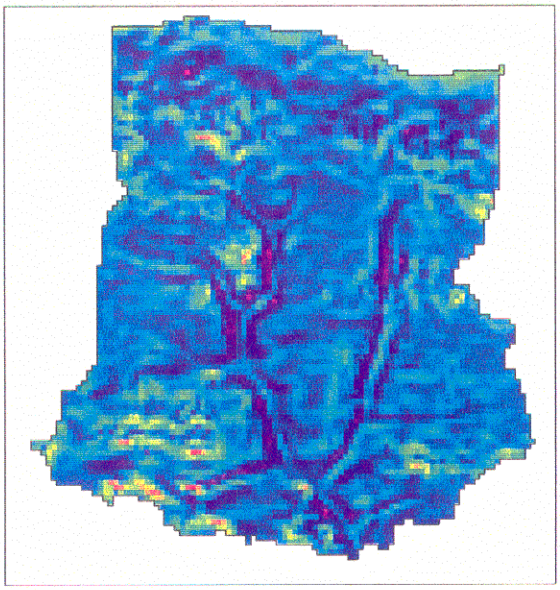

SIR-C slope - Reference slope

average difference = +0.9

maximum difference = +30.4 deg

minimum difference = -18.0 deg

Slope Difference (degrees)

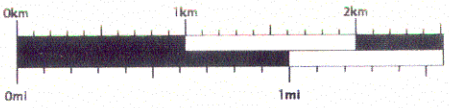

Figure 18. **Spatial distribution of differences in slope**

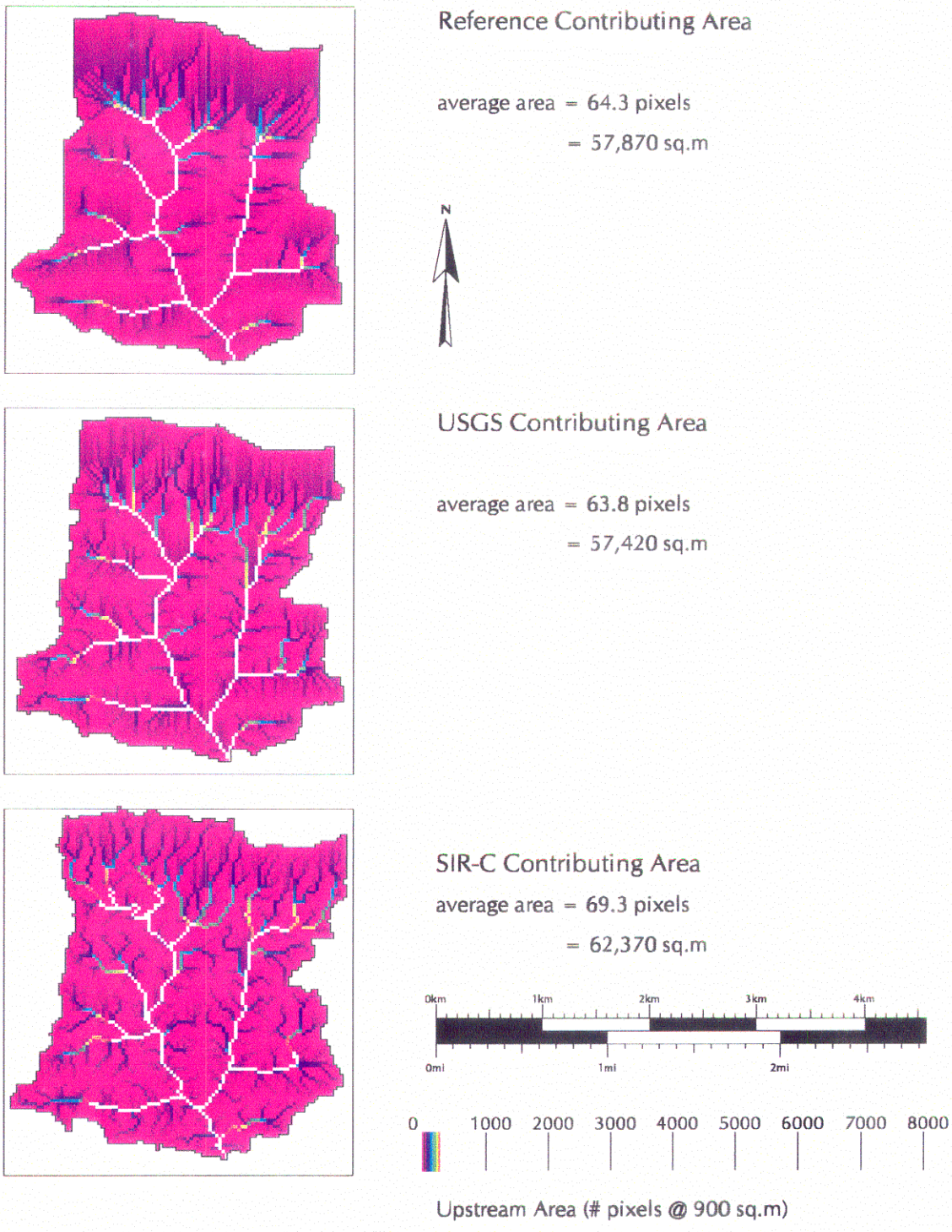

Figure 19. Spatial distribution of contributing area

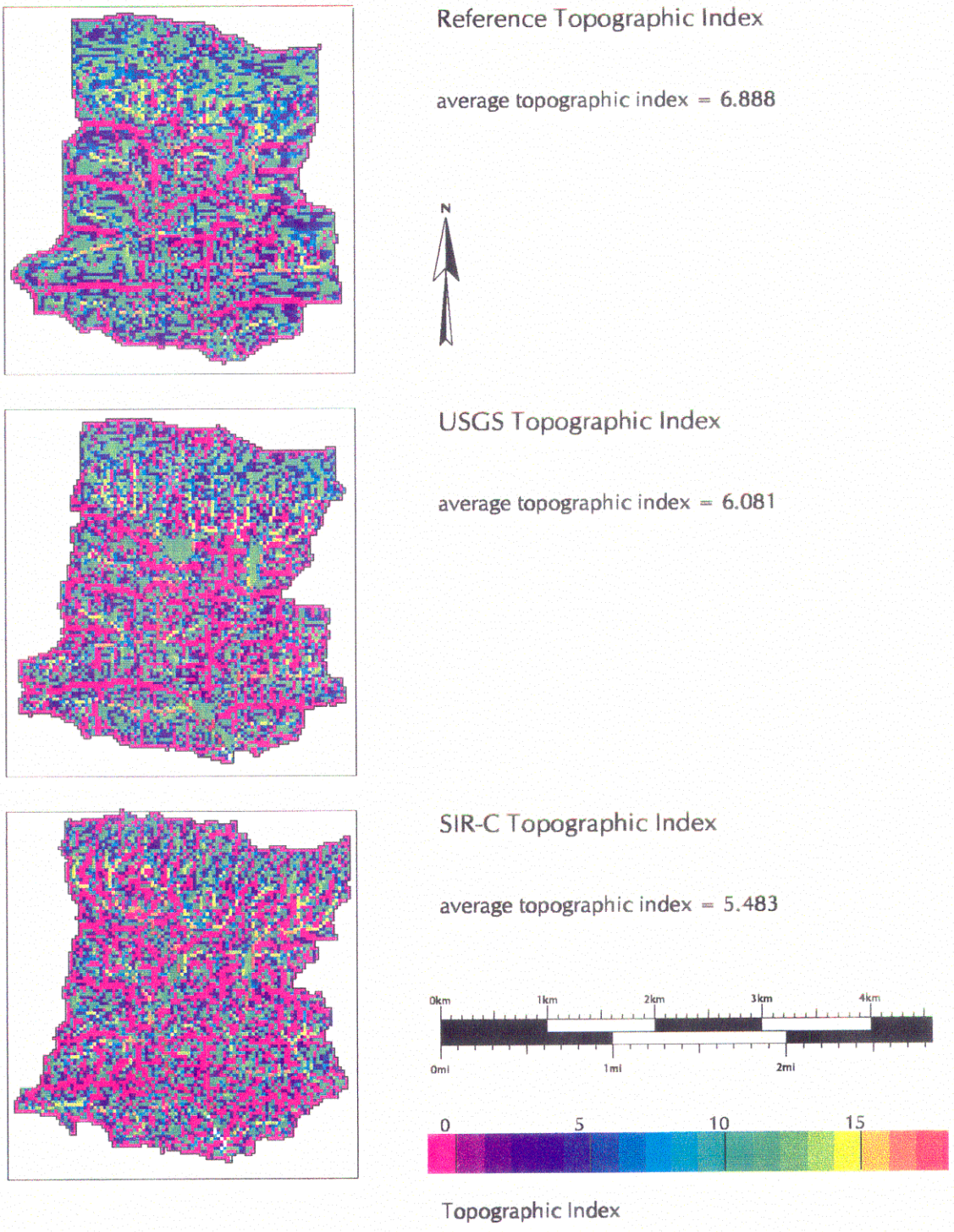

Figure 20. Spatial distribution of topographic index

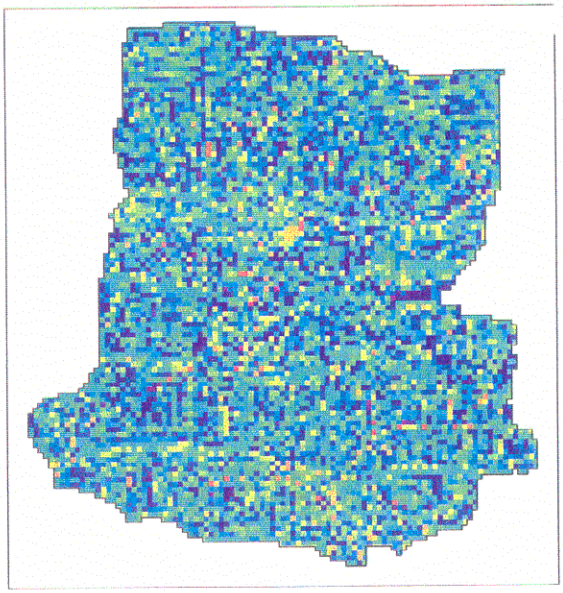

USGS Topographic Index -
Reference Topographic Index

average difference = -0.3

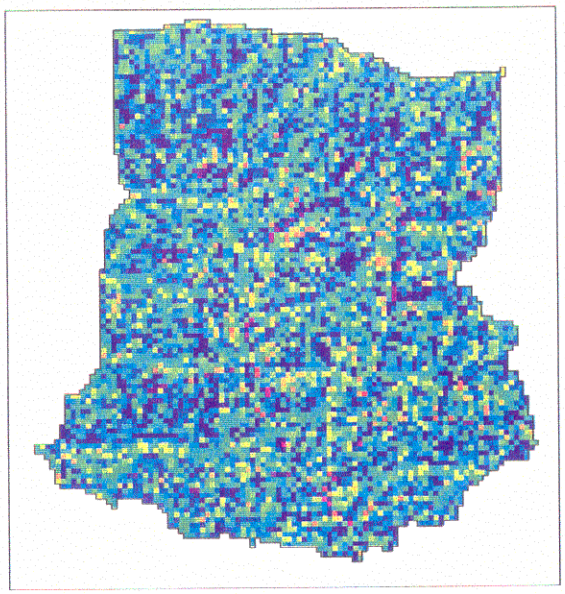

SIR-C Topographic Index -
Reference Topograhic Index

average difference = +0.9

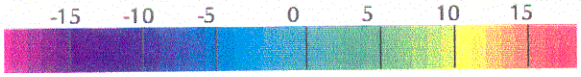

Topographic Index Difference

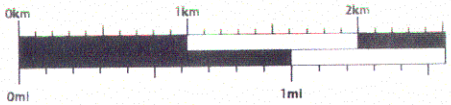

Figure 21. **Spatial distribution of differences in topographic index**

5. Error Structure of the USGS DEM

The USGS DEM displayed two types of discernible elevation differences from the reference DEM: a systematic grid-type error; and a pattern reminiscent of the basin topography (Figure 22). The possible source of these errors was examined and an error detection and correction algorithm was tested in an attempt to remove some of the errors.

5.1 Systematic errors

Abrupt changes in elevation differences are visible in the spatial difference images along N-S and E-W profiles. This grid-type error has previously been observed by Carter (1989). Carter examined standard USGS 7.5' DEM images and found linear error patterns with a cardinal orientation and artificial nature. These DEMs were derived by automated scanning of National High-Altitude Photography Program (NHAP) imagery using the Gestalt Photo Mapper II (GPM2). This is the same production process as described for the Valley View, PA standard USGS DEM (Section 2.1). Carter attributed errors to a lack of correlation between the edges of adjoining patches. Inspection of the NHAP images revealed areas of sun glint on the photos that would have prevented automatic correlation by the GPM2.

The DEMs studied by Carter were some of the earliest released by the USGS and predate the program of DEM correction that is now employed to remove obvious edge effects. Later DEMs were edge-smoothed to remove this problem. This smoothing process explains why the grid-type errors were not easily visible in the USGS DEM for Mahantango Creek: the smoothing process masks the edge effects by removing discontinuities but does not actually correct the correlation error by realigning the patch. The smoothed elevations are still in error and this error is visible when the DEM is evaluated, e.g. by comparison with a more accurate product.

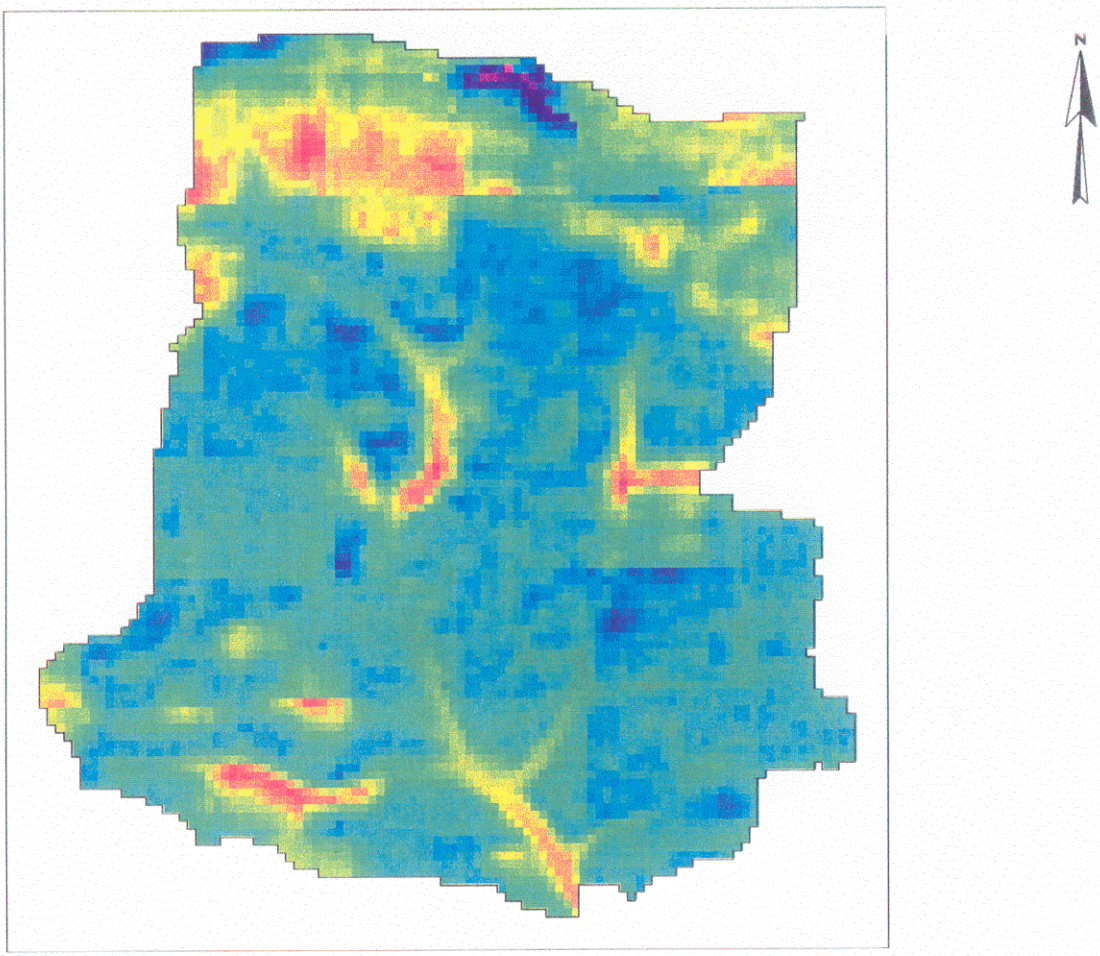

Figure 22. USGS Elevation Differences

5.2 Topographic errors

In addition to the edge error between patches, errors in USGS DEM elevations are also attributable to mismatches during the automatic correlation process of low-contrast images, relief-induced distortions between the images, and the presence of ambiguities due to identical objects or highly periodic textures on the terrain. These error sources can be related to topography. To examine this effect, the correlation between the USGS difference image and the basin topography was investigated by comparing the differences to topographical parameters. Elevations within two pixels of the edges of patches were excluded from this analysis in an attempt to remove the edge effect. No definitive mathematical relationship could be found between the differences and elevation or TOPMODEL topographic index although the data display distinct clusters (Figure 23 and Figure 24).

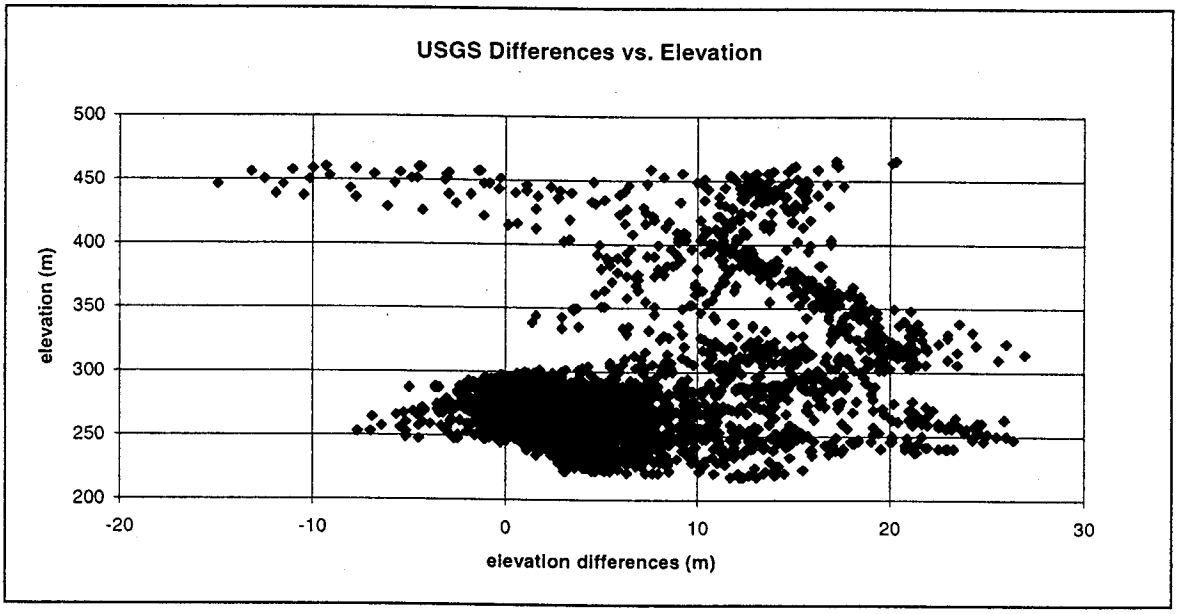

Figure 23. Elevation differences vs. elevation

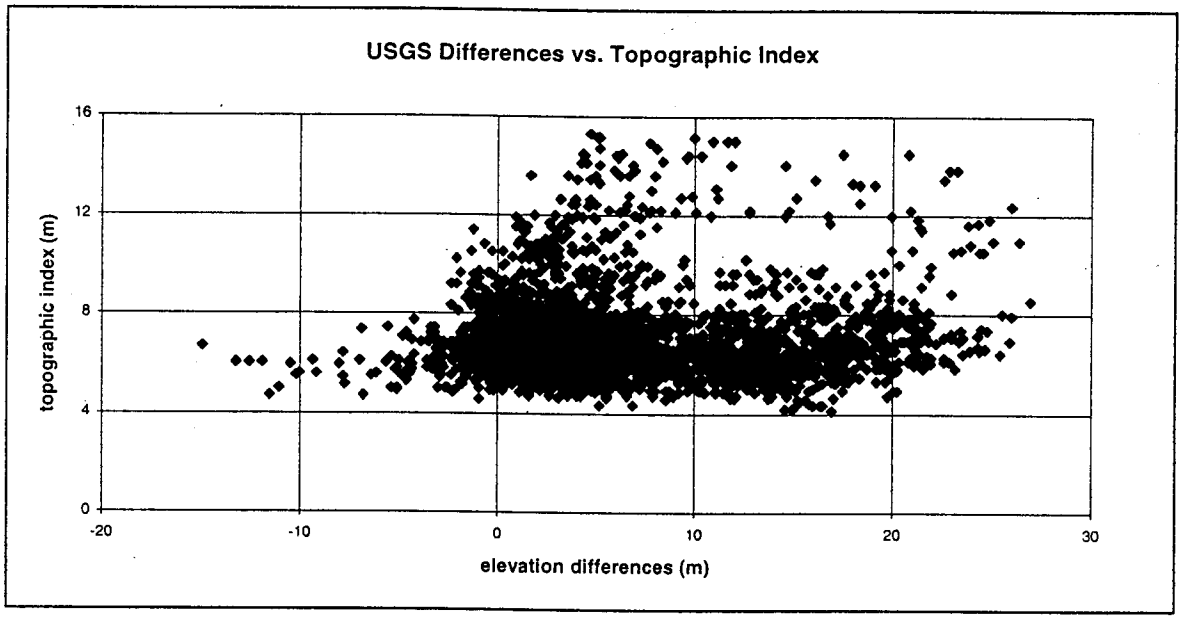

Figure 24. Elevation differences vs. TOPMODEL topographic index

Patches were categorized by terrain type, as either mountain ridge, stream channel or foot hills, in an attempt to separate the data clusters. Topographical parameters were considered separately for each terrain type. Average parameter values for each category are given in Table 6. Elevation differences are noticeably higher in mountainous areas and within the channel network where there are greater elevation variations. Plots of the differences for each category versus the topographic parameters gave different results for each terrain type but did not reveal any clear relationships (Figure 25, Figure 26 and Figure 27).

Table 6. Topographic parameters by terrain type

	Mountainous Area	*Channel network*	*Foot hills*
Average differences	9.66 m	4.88 m	3.95 m
Average elevation	338.46 m	260.34 m	270.41 m
Average contributing area	16,140 m^2	111,854 m^2	14,670 m^2
Average slope	13.56[x1]°	6.96°	7.11°
Average topographic index	6.62	7.12	6.56

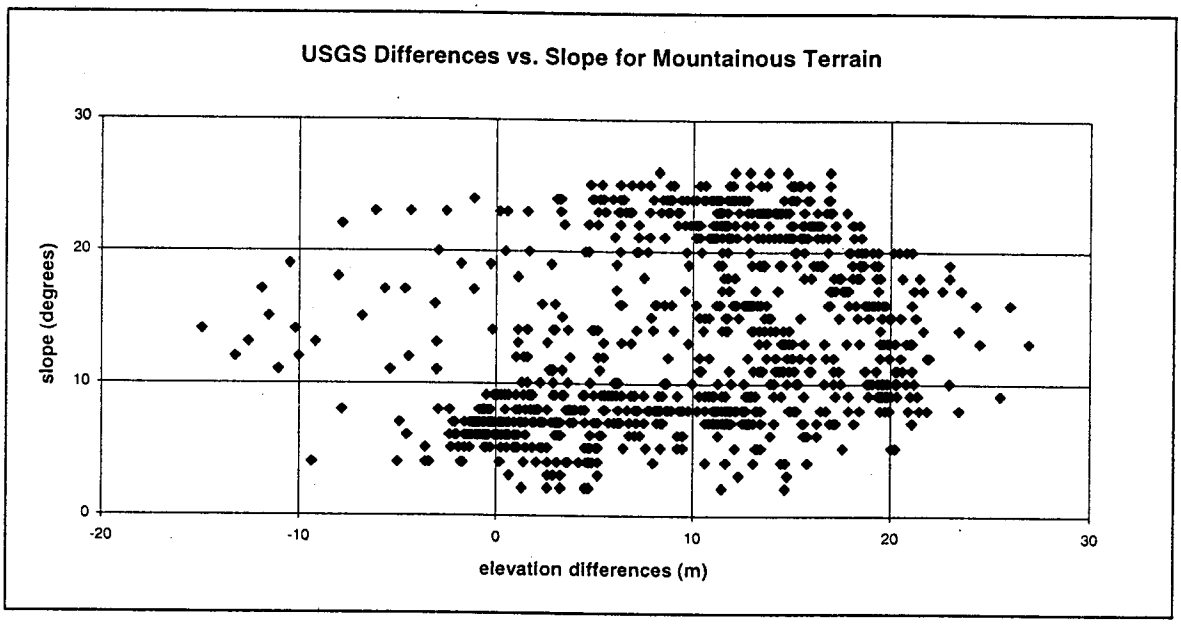

Figure 25. Elevation differences vs. slope for mountainous terrain

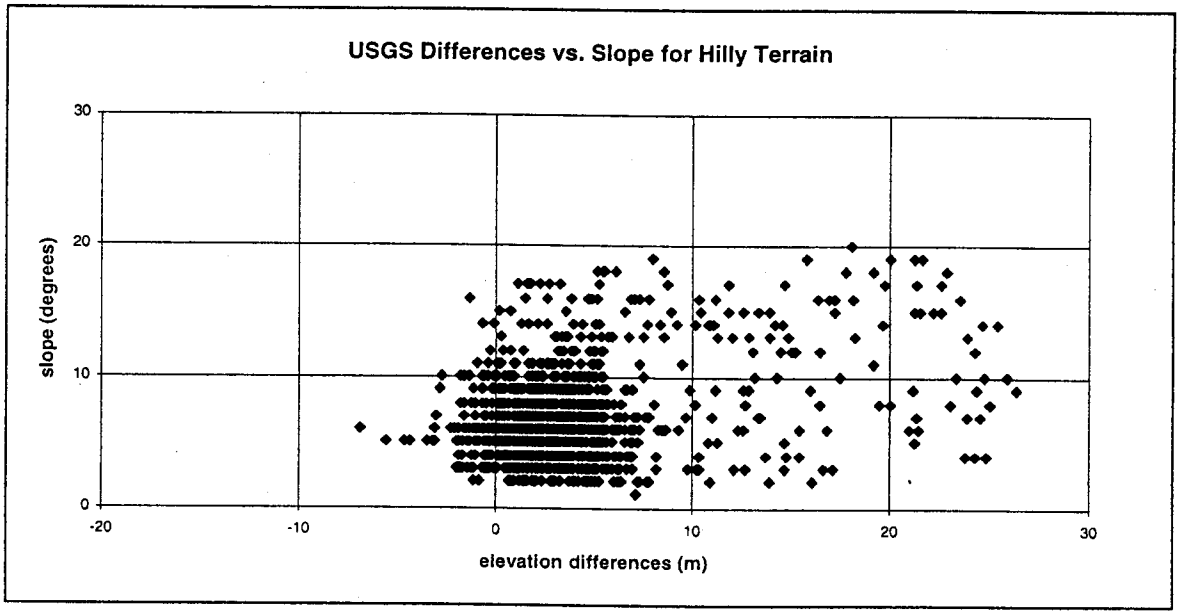

Figure 26. Elevation differences vs. slope for hilly terrain

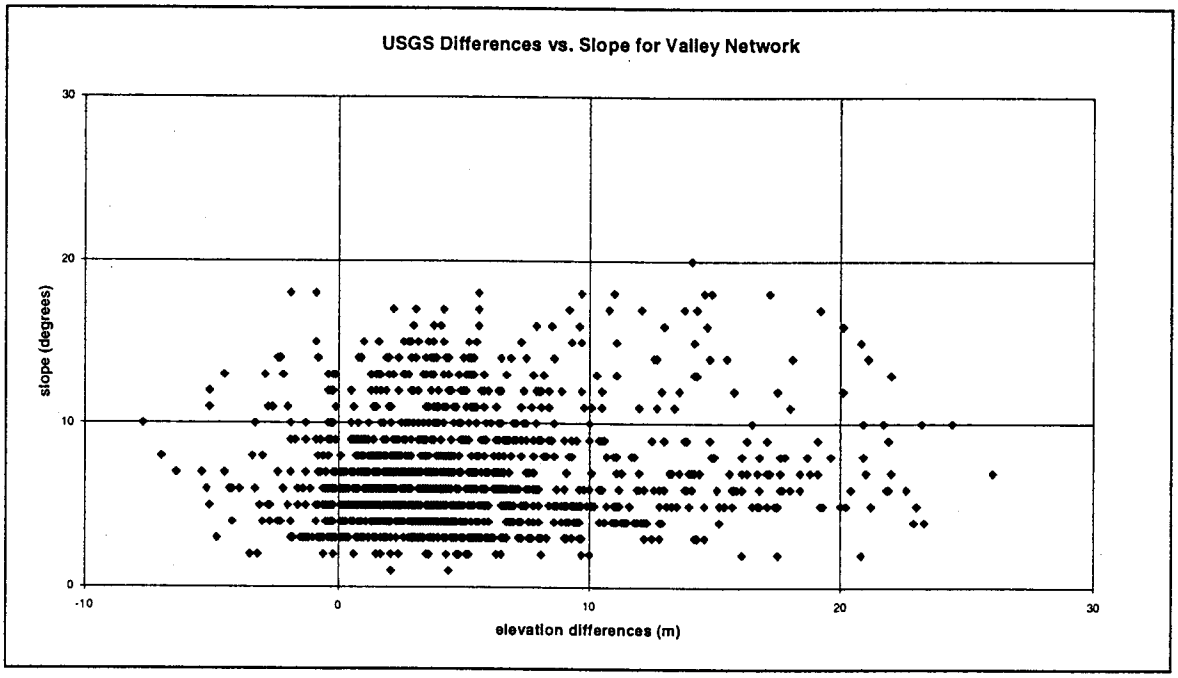

Figure 27. Elevation differences vs. slope for valley network

The mean and standard deviation of the differences varied greatly from patch to patch (Figure 28). The differences did display some correlation between topographic parameters and the elevation differences when examined separately. The nature of the relationship differed from patch to patch due to the different causes for local errors.

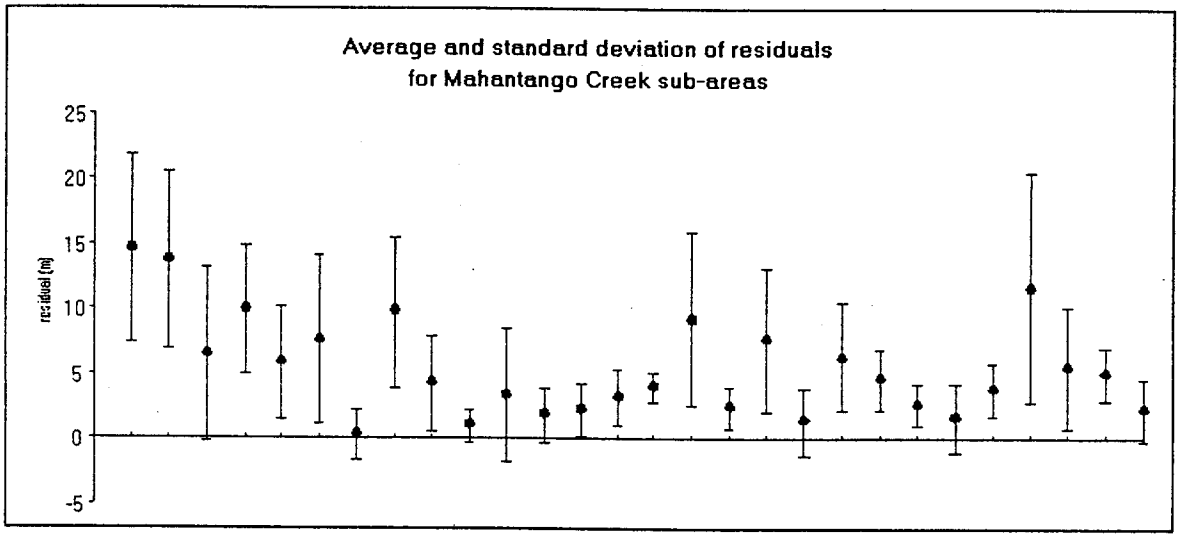

Figure 28. Mean and standard deviation of differences by patch

Along the ridges, differences were inversely related to elevations (Figure 29). This results from the proximity of lower elevation data to the top and bottom of the patch where the edge effect is most prominent. Elevation differences are much lower along the ridge, which is well-defined by the DEM.

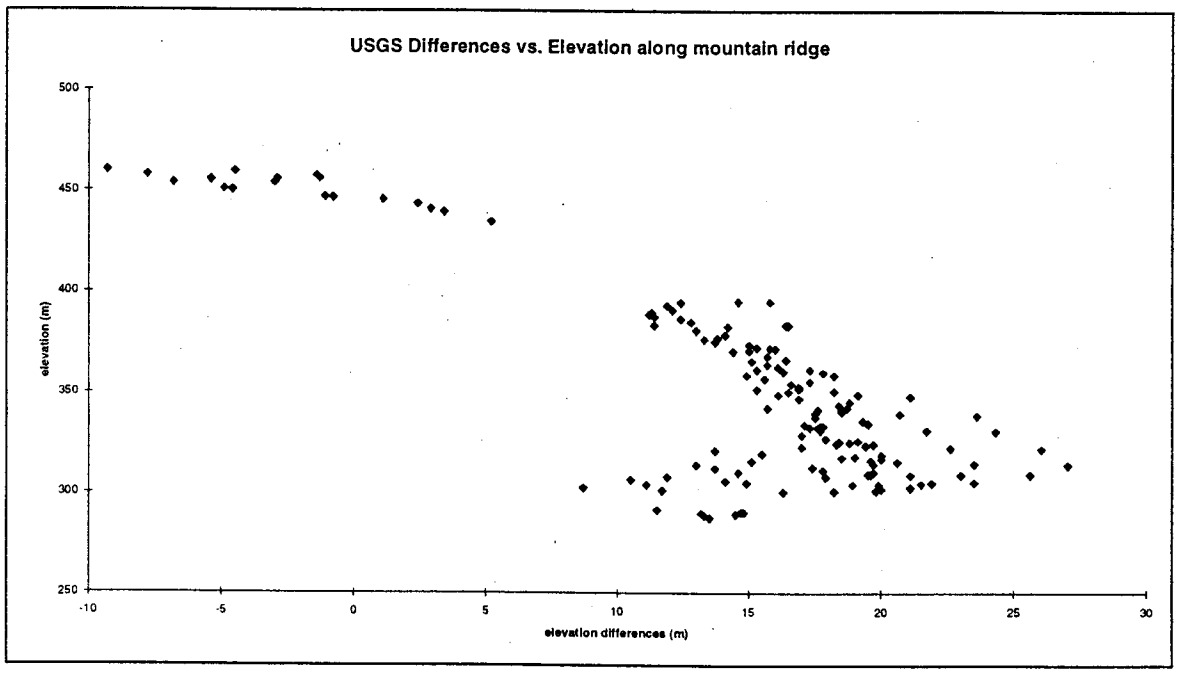

Figure 29. Residual vs. elevation in sub-area along mountain ridge

Differences in a patch in the lowlands in the south of the Mahantango Creek catchment were found to be inversely related to elevation and directly related to contributing area (Figure 30). This sub-area exhibited large differences in the area of the stream tributary where the USGS DEM failed to capture this topographic feature, which could be due to sun glint on the stream channel in the aerial photography.

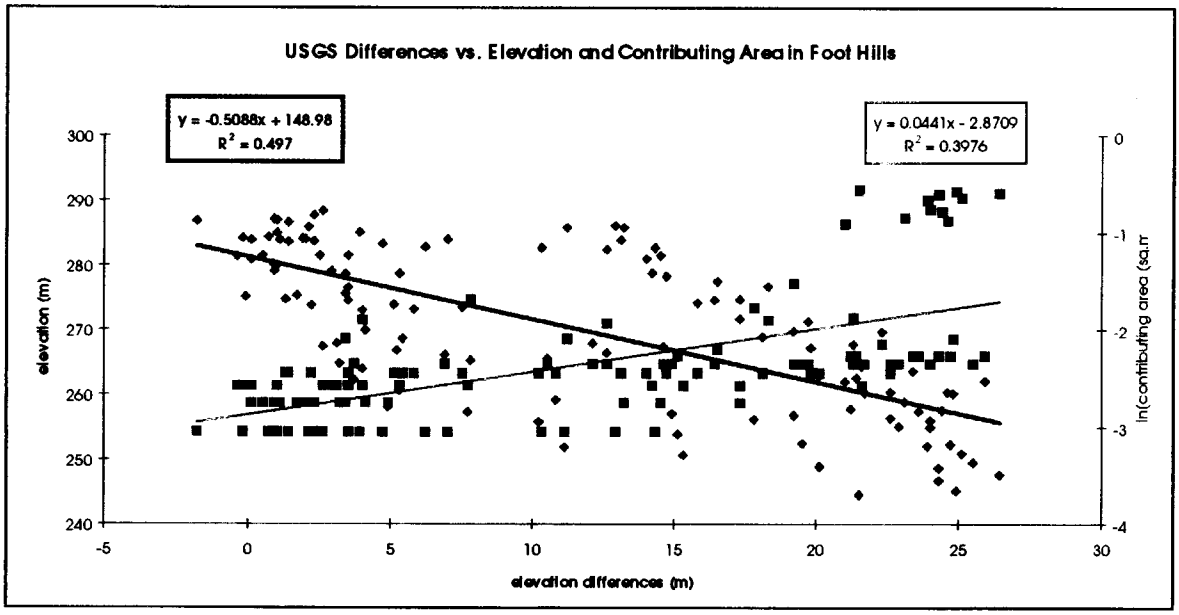

Figure 30. **Elevation differences vs. elevation and contributing area in sub-area in foothills**

5.3 Error detection and correction

Previous research on the detection and correction of local errors in digital elevation models has focused on the development of algorithms to check a model systematically for obvious errors. These methods are based on the assumption that topographic data are derived from a continuous surface which varies smoothly in elevation. Any data causing sharp discontinuities in the elevations or sudden changes in the surface slope are likely to be in error.

Hannah (1981) developed three sets of slope tests to detect error. The *slope constraining test* checks if the slope to any of the eight surrounding pixels exceeds a specified maximum. *The local neighbor slope test* checks the four pairs of slope crossing a point against a set maximum. *The distant neighbor slope consistency test* checks the pair of slopes approaching a point across each of the eight neighbors for consistency. A correctness indicator ranging from 0.0 (probably in error) to 1.0 (probably correct) is assigned to each elevation point based on the slope tests. Pixels with low correctness indicators are assumed to be erroneous and are replaced with the average of the elevations of the surrounding cells weighted by their respective correctness indicators. This correction process is repeated in an iterative fashion until changes are no longer significant.

Hannah's and similar tests are problematic in that they require the definition of threshold values for the slope or any other parameters used to detect errors. Felicisimo (1994) suggested a parametric test based on elevation differences that would not require threshold values. This method determines the difference between the elevation at a point and the elevation estimated for the point based on the neighboring cells. Bilinear interpolation of the elevations of the four cardinal neighbors is suggested to estimate the pixel elevation but more sophisticated techniques such as kriging can also be used. The mean and standard deviation of the differences are calculated and the Student *t* test is used to determine if each difference is within the population. Points outside of the population are assumed to be in error and are replaced with an interpolated elevation calculated from the neighboring cells.

Error detection methods which check a DEM for errors based solely on the DEM itself are used during the post-processing of DEMs to detect and correct errors that may have occurred in the correlation process. These tests are preferred for the detection of local errors over global techniques, such as curve fitting, which do not exclude points suspected to be in error from the final DEM.

Felicisimo's parametric test was used to determine if errors in the raw, unfilled USGS DEM could be identified and corrected. The Student *t* test was applied to every point as:

$$t_{i,j} = \frac{\delta_{i,j} - \delta}{s_\delta} \tag{3}$$

where $\delta_{i,j}$ is the difference between the elevation at a point and the elevation estimated from an average of the four cardinal neighbors. δ and s_δ are the mean and standard deviation of all the differences, respectively.

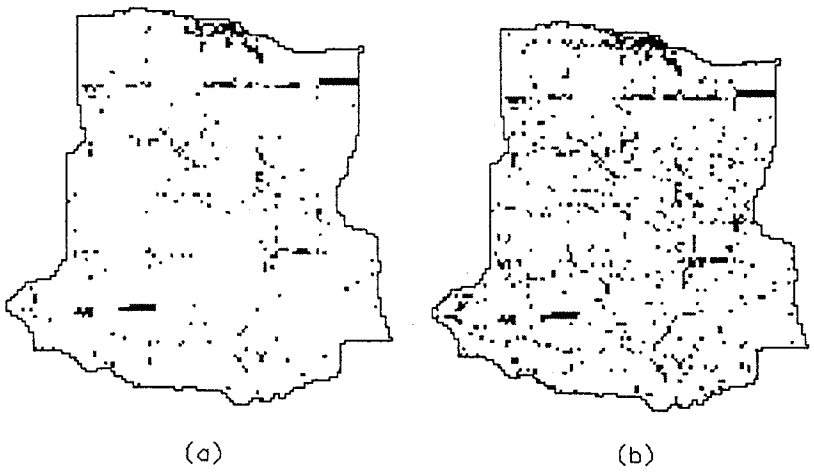

Figure 31. Rejected data points at (a) 90% and (b) 80% confidence level

The rejected points at 90% ($t_{i,j} > 1.645$) and 80% ($t_{i,j} > 1.282$) confidence levels are shown in Figure 31. 4.2% of the elevations were rejected at the 90% confidence level and 8.8% were rejected at the 80% level. The spatial distribution of the *t* statistic identifies some of the error patterns seen in the differences but the test was not able to completely identify either the systematic production errors or the

errors related to basin topography. Other elevation estimators, averaging the four diagonal neighbors or a weighted average of all eight neighbors, were tested for their ability to detect the errors and were found to perform in a similar fashion.

Rejected points were replaced with a bi-linear interpolation of the elevations of the four cardinal neighbors. This correction algorithm was not effective at resolving differences between the USGS DEM and the reference product. The corrected spatial difference image displays the same error patterns and results in a higher mean and standard deviation of errors (Table 7).

Table 7. Elevation differences between USGS and reference DEMs

USGS DEM	*Minimum Difference*	*Maximum Difference*	*Average Difference*	*Standard Deviation*
Original	-24.3 m	27.0 m	7.45 m	11.30 m
Corrected	-19.3 m	34.3 m	8.57 m	11.42 m

It was not surprising that the edge effects could not be completely eliminated by the parametric error detection. This method relies on comparisons between the pixel elevation and an estimate of the neighboring grid cell elevation. Smoothed data which have been averaged over a group of cells will not be found to be in error. To correct the edge effect properly, the patches should be repositioned based on a more accurate correlation with neighbors. This repositioning may require lifting, lowering or tilting of the patch with respect to surrounding areas.

6. Hydrological Model of the WE-38 Watershed

The Distributed Soil-Hydrology-Vegetation Model (DHSVM) was used to simulate streamflows and hydrologic fluxes on a 3-hour timestep for a continuous four year period starting October 1, 1983. Simulations were run using each of the three DEMs.

6.1 Input data

DHSVM requires specification of vegetation and soils information, as well as meteorological forcing data and the initial hydrological state variables for each pixel. In addition, a number of model parameters must be specified.

6.1.1 Vegetation types

Multi-polarization C-band (5.8cm wave length) and L-band (23.5cm wavelength) SIR-C images were taken over the Mahantango Creek watershed from space shuttle Endeavor on April 14, 1994. Niko Verhoerst (previously at Princeton University) derived land cover classifications from these data. A classifier program, based on work by Pierce et al (1994), was used to designate the vegetation class of each pixel (12.9 m azimuth by 13.3 m range) as urban, tall vegetation, short vegetation, or bare surfaces (Figure 32). The tall vegetation class defines areas of deciduous hardwood forest, short vegetation refers to cropland and bare surface is pasture land. Overstory and understory properties were defined for each vegetation class as reported in Appendix B. The areas of each terrain type differ from a previous descriptions of the basin land coverage by Pionke and Kunishi (1992) who reported larger cropland area and less forested areas (Table 8).

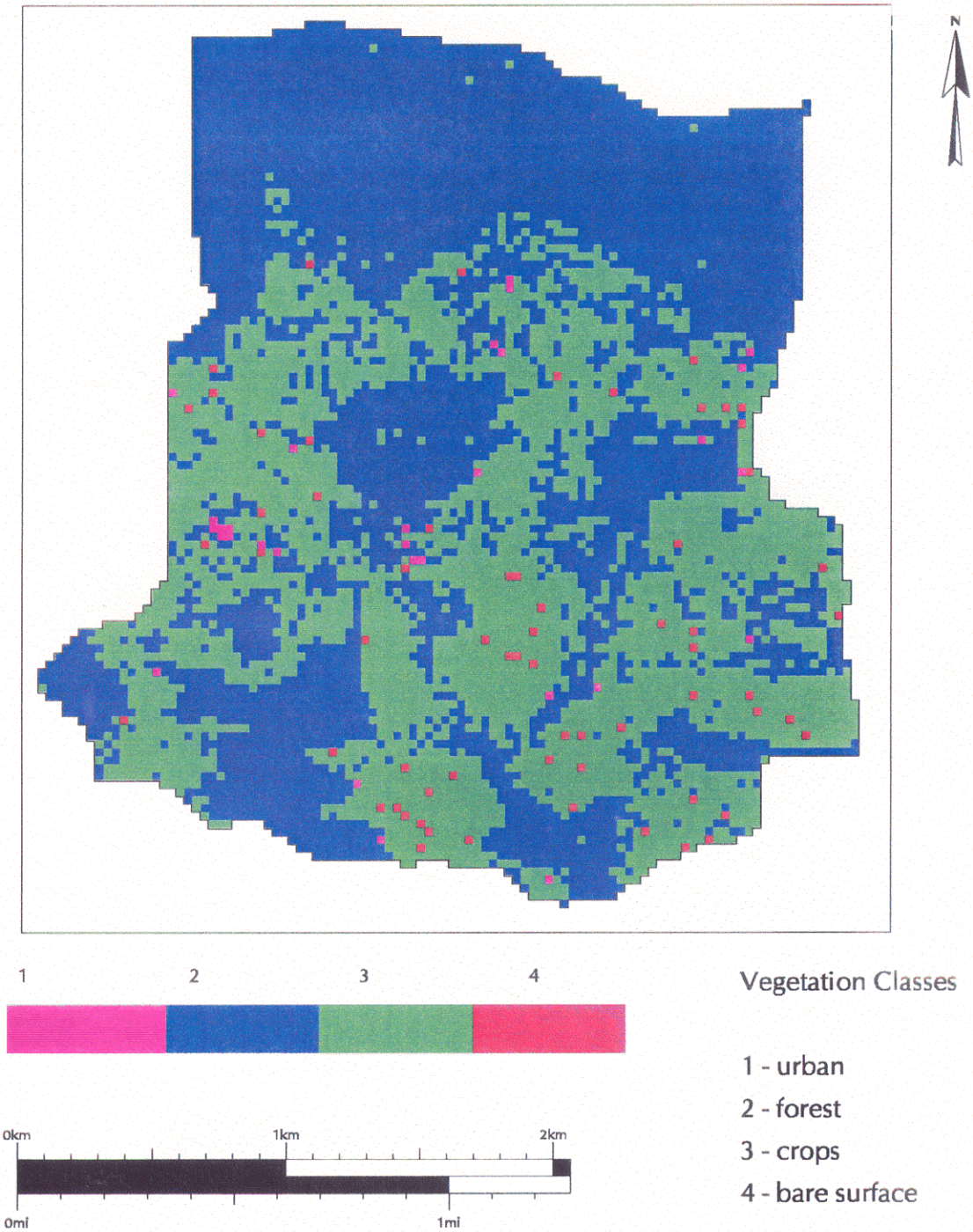

Figure 32. Mahantango Basin vegetation types

Table 8. Vegetation classifications

Vegetation class	*Description*	*SIR-C defined area*[5]		*Literature Description*[6]
1	urban	0.03 km^2	0.4%	-
2	tall vegetation	4.01 km^2	55.6%	35%
3	short vegetation	3.11 km^2	43.1%	57%
4	bare surfaces	0.06 km^2	0.8%	8%

6.1.2 Soil types

Distributed soil classifications for the Mahantango Creek research watershed were developed by Peter Troch (Ghent University) based on the USDA Soil Conservation Service (SCS) county soil surveys (Figure 33). 15 soil types were identified over the basin (Table 9). The majority of the soils are silt loam. Soil parameters were provided by the SCS for each soil type as reported in Appendix B.

[5] Determined by Niko Verhoerst using a classifications based on interferometric SAR images

[6] Pioke and Kunishi, 1992.

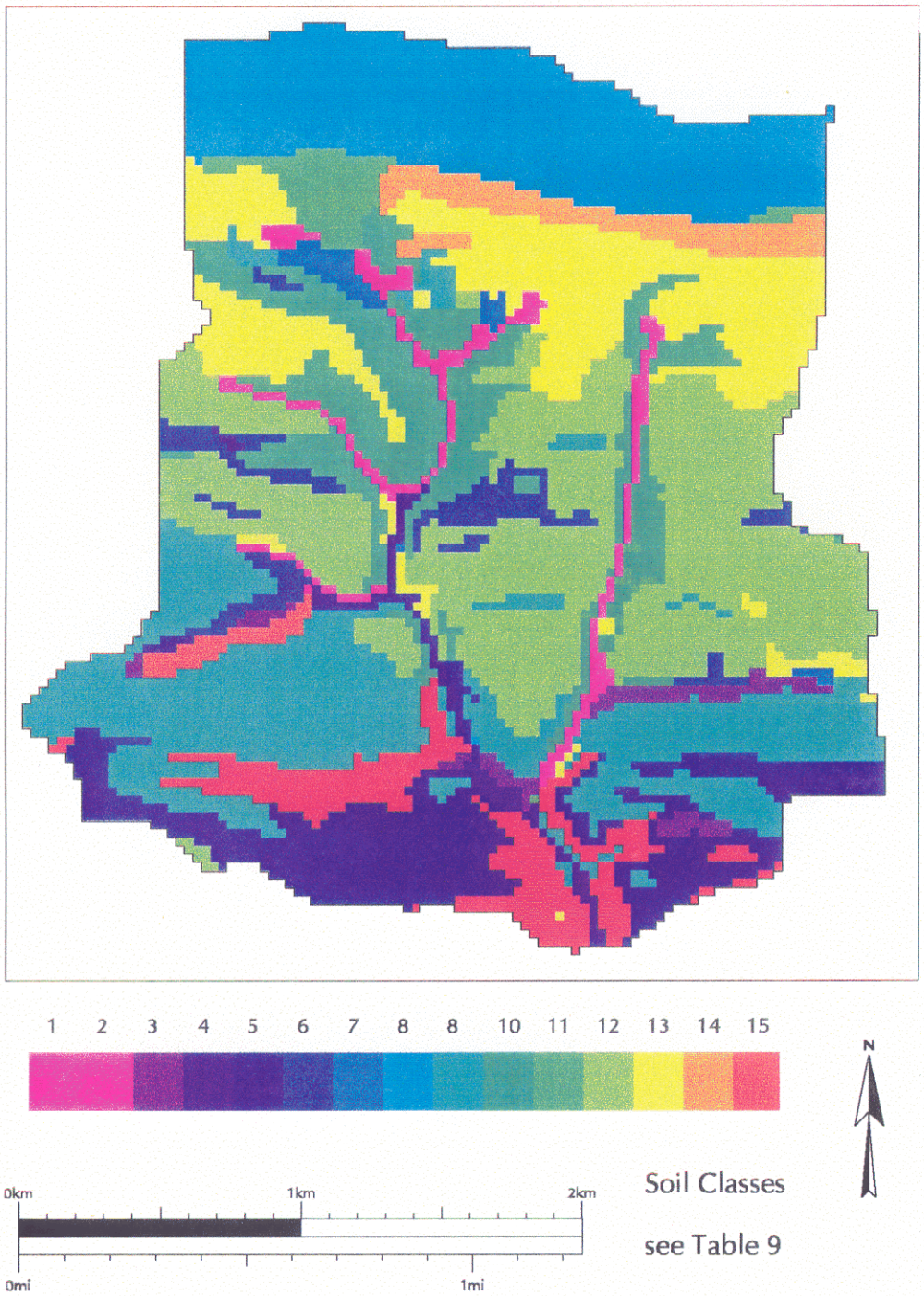

Figure 33. Mahantango Basin soil types

Table 9. Soil classifications

USDA Soil Classification	*Soil name*	*Description*	*Area (km^2)*
1	Albright	silt loam	0.20
2	Alvira	silt loam	0.10
3	Basher	silt loam	0.10
4	Berkes	silt loam	0.64
5	Calvin	silt loam	0.21
6	Conyngham	silt loam	0.06
7	Dekalb	sandy loam	0.97
8	Harleton	silt loam	1.19
9	Klinesville	silt loam	0.69
10	Laidig	gravel loam	0.14
11	Leck Kill	silt loam	1.47
12	Meckesville	loam	0.84
13	Meckesville	stony loam	0.19
14	Shelmadine	silt loam	0.05
15	Weickert	silt loam	0.36

6.1.3 Meteorological data

Daily records of maximum and minimum temperature, relative humidity and wind speed were taken at the MD-38 meteorological station located at the USDA-ARS Pasture Systems & Watershed Management Research Laboratory in the Mahantango Creek watershed. These data were used to construct 3-hourly records of cloud coverage, relative humidity, wind speed, air temperature, and incoming long wave radiation.

Cloud cover was calculated from estimates of clear sky and net short wave radiation based on the daily maximum and minimum temperature and the elevation of the temperature station using equations from Bras (1990):

$$f = \sqrt{\frac{1}{0.65}} * \sqrt{1 - \frac{I'_s}{I_c}} \tag{4}$$

$$I_c = 0.6 + 2.95 \times 10^{-5} * z \tag{5}$$

$$I'_s = I_c * \left\{ 1 - \exp\left[b * \left(T_{max} - T_{min} \right)^{2.4} \right] \right\} \tag{6}$$

where f is the cloudiness factor, I_s' is the net short wave radiation, I_c is clear sky radiation, z is elevation (244.0 m), T_{max} is daily maximum temperature (°C) and T_{min} is the daily minimum temperature (°C).

Resulting cloudiness factors were normalized from zero to one with zero representing clear sky conditions and one representing completely overcast conditions. Cloud coverage, relative humidity and wind speed are assumed to be constant throughout the day.

Air temperature was calculated as the sum of a fraction of the minimum temperature of the previous day, the current minimum and maximum temperature and the minimum temperature on the following day (Table 10) based on the method of Anderson (1968).

Table 10. Estimation of air temperature

Time	*% Previous Day T_{max}*	*% Current T_{min}*	*% Current T_{max}*	*% Next Day T_{min}*
24:00 - 3:00	19%	81%	-	-
3:00 - 6:00	5%	95%	-	-
6:00 - 9:00	2%	68%	30%	-
9:00 - 12:00	-	40%	60%	-
12:00 - 15:00	-	21.3%	76.3%	2.4%
15:00 - 18:00	-	2.5%	92.5%	5%
18:00 - 21:00	-	1.25%	62.75%	36%
21:00 - 24:00	-	-	33%	67%

Dew point temperature was calculated from the air temperature and the relative humidity using an approximation given by Maidment et al (1993) as:

$$T_d = \frac{237.3}{\left[\frac{17.27}{\ln\left(\frac{e_s}{0.6108}\right)} - 1\right]} \tag{7}$$

$$e_s = \frac{RH}{100} * e \tag{8}$$

$$e = 0.6108 * \exp\left(\frac{17.27 * T}{237.3 + T}\right) \tag{9}$$

where T_d is the dew point temperature(°C), T is the air temperature (°C), RH is the percent relative humidity, e_s is the saturation vapor pressure and e is the actual vapor pressure at the prevailing temperature.

Incoming long wave radiation was calculated from air and dew point temperature and cloud cover based on equations from Maidment et al (1993) as:

$$L_i = (1-f)*\varepsilon'*\sigma*(T+273.3)^4 + f*\sigma*(T_d+273.3)^4 \quad (10)$$

$$\varepsilon' = 0.740 + 0.0049*e_s \quad (11)$$

where L_i is incoming long wave radiation ($MJ/m^2/day$), T_d is the dew point temperature (°C), T is the air temperature (°C), e_s is the saturation vapor pressure, ε' is the net emissivity between the atmosphere and the ground and σ is the Stefan-Boltzmann constant (4.903×10^{-9} $MJ/m^2/sec/°K^4$).

Precipitation records were extracted from the ARS database for two long-term precipitation gages, (see Figure 3). The raw data were recorded in breakpoint format with readings taken each time the cumulative precipitation exceeded 0.1 inch. These data were aggregated to 3-hourly records for the period of interest.

Clear sky solar radiation was estimated for each pixel using the model of Dubayah et al (1990) as coded in Image Processing Workbench (IPW) (Frew, 1990; Longley et al, 1992). The model computes clear sky radiation which is partitioned into direct and diffuse beam components, accounting for the date, time of day, pixel location, slope, aspect and the effects of shading or reflection of radiation from surrounding terrain. Diffuse and direct beam radiation is calculated monthly for each pixel based on the distribution of the solar radiation at the solar midpoint of each month and then discretized into ten equi-probable classes.

6.1.4 Basin parameters

Those parameters which were assumed not to vary spatially are given in Table 11.

Table 11. Basin constant parameters

Parameter	*Value*
K_{sat} saturated horizontal hydraulic conductivity	0.06 m/hr
K_{sat} exponential decay coefficient	30 m
snow roughness length	0.015
wind measurement height	20.0 m
vapor pressure deficit causing stomatal closure	4.0 mb
visible light fraction of total short wave radiation	0.5
meteorological station elevation (md38, me37)	244.0, 284.0 m
temperature lapse rate	0.007 °C/m
dew point lapse rate	0.0055 °C/m
maximum temperature for precipitation as snow	3.3 °C
minimum temperature for precipitation as rain	0 °C
precipitation location adjustment factor	1.37
maximum snow pack surface layer (water equivalent)	0.125 m
depth of soil below the rooting zones	1.0 m

6.1.5 Initial soil moisture

To produce realistic initial conditions, a one-year "warmup" run was made starting with constant initial soil moisture on October 1, 1983. Since DHSVM is a continuous simulation model, the effect of the initial conditions are expected to be insignificant after the first water year (October - September) once the

basin has become saturated during the spring high runoff period. Spatial predictions of depth to saturation and soil moisture in the rooting zones for October 1, 1984 were then used as the initial conditions for the four year simulation which started October 1, 1983, with each DEM. Ideally the warmup year would not have been reused however this procedure was thought to be justified given the relatively short four year period for which coincident meteorological data were available.

6.2 Model testing

As DHSVM is a physically-based model, the surface characteristics data represent physical descriptions of the watershed and should not require calibration. However, some input data are not known with great accuracy (e.g. leaf area index, albedo) and other data are constructed from a coarser timestep (e.g. humidity, wind speed) or from other estimated parameters (i.e. solar radiation, cloud cover). Some of the parameters listed in Table 11 are assumed not to vary spatially for convenience alone (e.g. saturated hydraulic conductivity) and soils and vegetation parameters that must of necessity be assumed constant also introduce errors in model predictions.

Predicted streamflows for the Mahantango WE-38 watershed as defined by the reference DEM were compared to observed records to ensure that DHSVM was able to model the hydrologic processes adequately. As DHSVM is being used for a sensitivity analysis to determine the effects of difference in the DEMs, exact model predictions were not necessary, however, it was required that the model be representative of the hydrologic behavior of the watershed. Results for the 1983/84 water year are reported in Figure 34 and the remaining years are reproduced in Appendix D. Other hydrologic fluxes were also examined to confirm that they were appropriate for the basin climatology and hydrology.

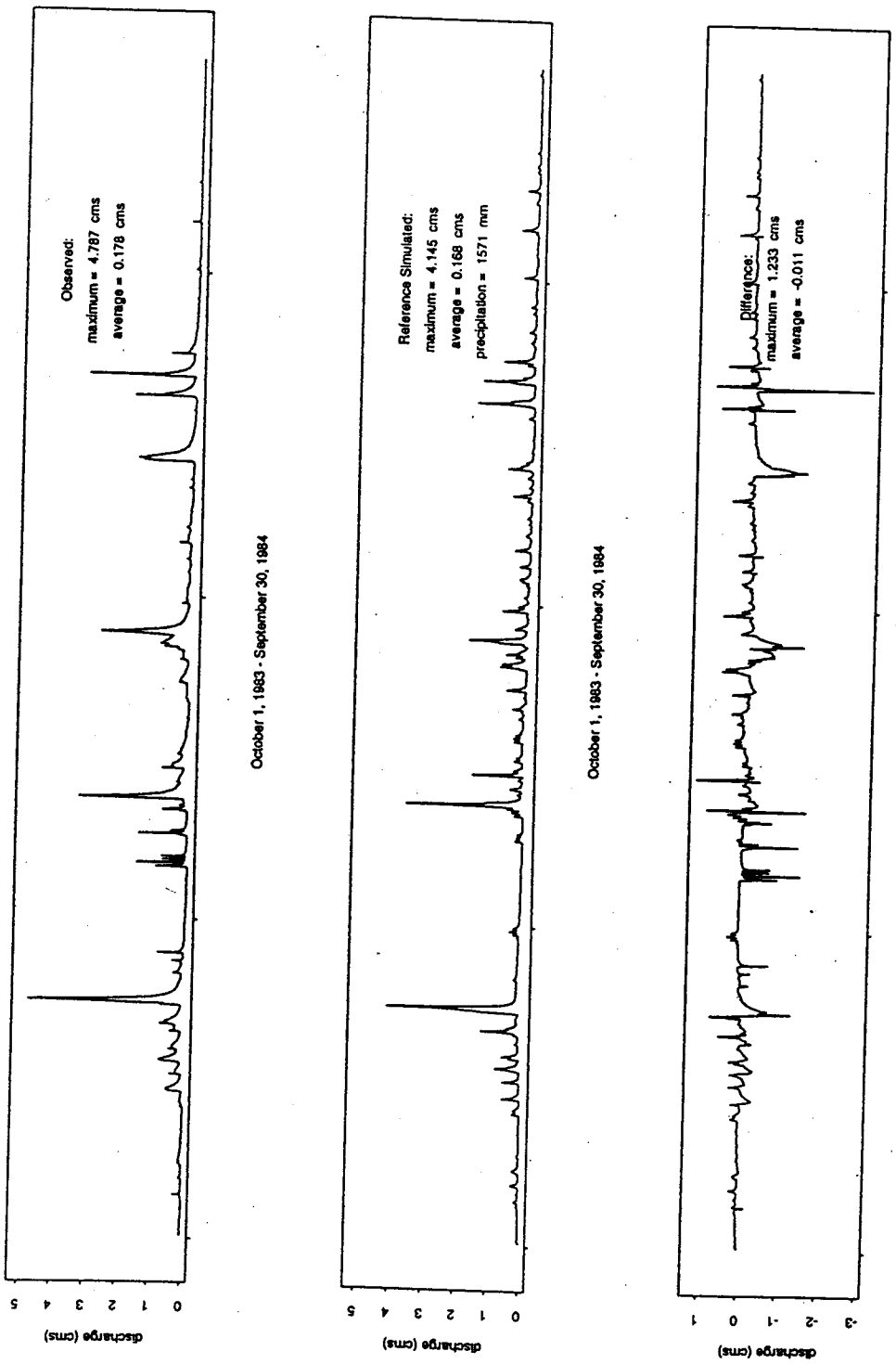

Figure 34. Calibration differences, 1983/84 water year

7. Hydrologic Results

DHSVM computes hydrologic fluxes at each grid cell continuously. This information can be output as a basin-average or single-pixel time series for any time period within the record or as a spatial basin image for a single timestep. For this analysis, spatial distribution of precipitation, depth to saturation and runoff production were examined during both high and low flow periods. Time series predictions of streamflow based on each DEM were compared with observed records at the WE-38 weir.

7.1 Precipitation

Precipitation at each pixel is an input variable for the model. Precipitation observations were available at two meteorological stations on the basin (see Figure 3). Precipitation at each gage was lapsed to the elevation of each pixel using the adjustment shown in Figure 35. As both meteorological stations are located in the lower part of the watershed, observed precipitation was also scaled by a basin-constant factor to avoid a downward bias of runoff predictions.

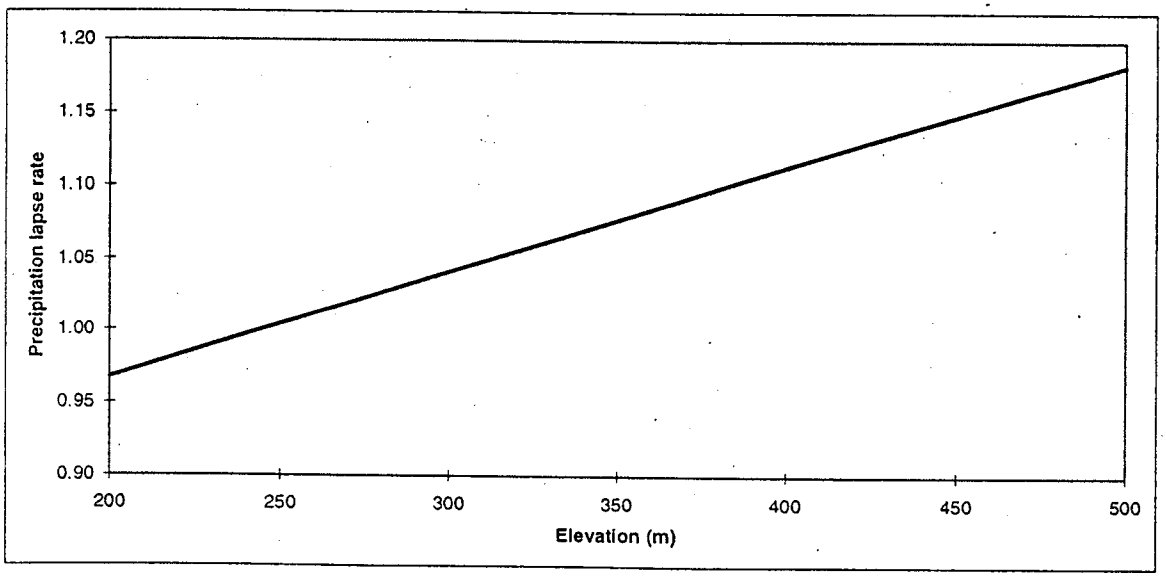

Figure 35. Precipitation adjustment factor

The digital elevation data directly influence the precipitation input when it is lapsed to the pixel elevation for each grid cell. However, because the cumulative elevation distribution functions are similar for each of the DEMs (see Figure 10), the basin mean monthly values are not significantly different (Table 12).

Table 12. Average monthly precipitation (mm)

	Reference DEM	*USGS DEM*	*SIR-C DEM*
October	56.6	56.9	56.9
November	123.6	124.3	124.3
December	86.3	86.8	86.8
January	44.4	44.6	44.6
February	71.7	72.0	72.1
March	73.5	73.9	73.9
April	90.1	90.6	90.6
May	106.6	107.1	107.2
June	144.4	145.1	145.2
July	125.0	125.6	125.7
August	101.8	102.3	102.4
September	119.3	119.9	119.9

7.2 Soil moisture and runoff production

Spatial images of the instantaneous depth to saturation and runoff production on December 14, 1983 are reproduced in Figure 36 and Figure 37. Depth from the surface to the water table during the high flow and low flow events of each year (Table 13), and runoff production during the high flow events are reproduced in Appendix C. DHSVM uses the DEM explicitly and does not require inputs of slope,

contributing area and topographic index. However, the spatial distributions of these topographic parameters were found to be similar to those of depth to saturation and runoff production. This is not surprising as the topographic index, although not used directly in DHSVM, is an indicator of the runoff producing tendency of a cell based on its slope and upstream contributing area. The valley network is more pronounced in spatial predictions of depth to saturation and runoff production based on the reference DEM. The lower resolution DEMs resulted in scattered spatial images of soil moisture and low runoff production. This suggests that model predictions based on the reference DEM are more representative of the physical processes occurring within the basin.

Table 13. Events selected for spatial images of soil moisture

Year	*High flow event*	*Low flow event*
1983-1984	December 14, 1983, 15:00	July 26, 1984, 24:00
1984-1985	February 13, 1985, 15:00	August 30, 1985, 24:00
1985-1986	March 15, 1986, 24:00	January 15 1986, 24:00
1986-1987	September 14, 1987, 24:00	August 5, 1987, 24:00

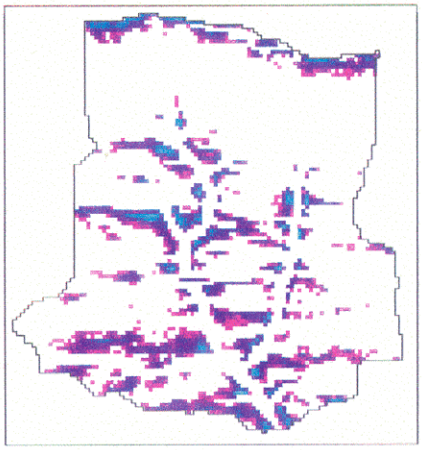

Reference Depth to Saturation

average depth = 134 mm

maximum depth = 514 mm

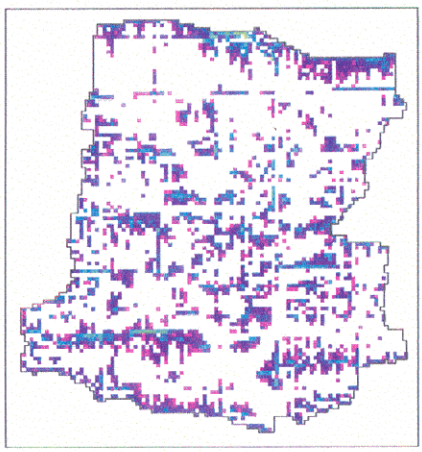

USGS Depth to Saturation

average depth = 175 mm

maximum depth = 674 mm

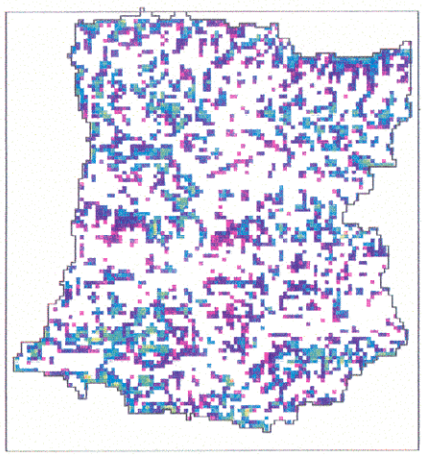

SIR-C Depth to Saturation

average depth = 259 mm

maximum depth = 895 mm

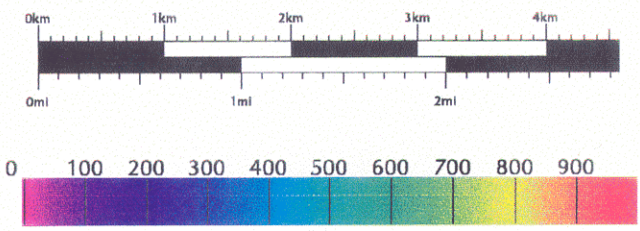

Depth to Saturation (mm) on Dec 14, 1983, 3 pm

Figure 36. **Spatial distribution of depth to saturation, December 14, 1983**

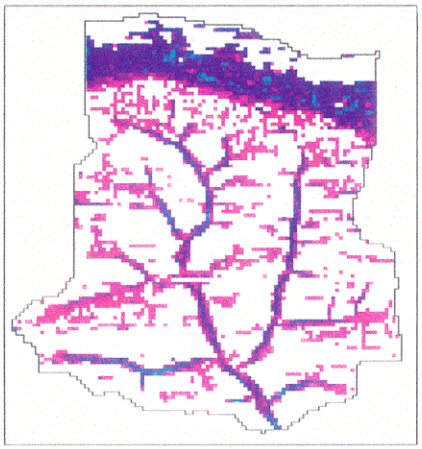

Reference Runoff Production

average runoff depth = 1.1 mm

maximum runoff depth = 6.0 mm

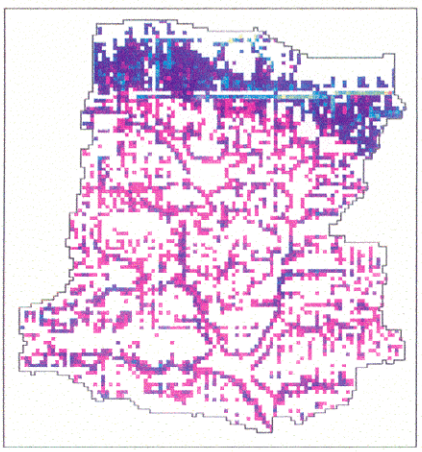

USGS Runoff Production

average runoff depth = 1.3 mm

maximum runoff depth = 12.0 mm

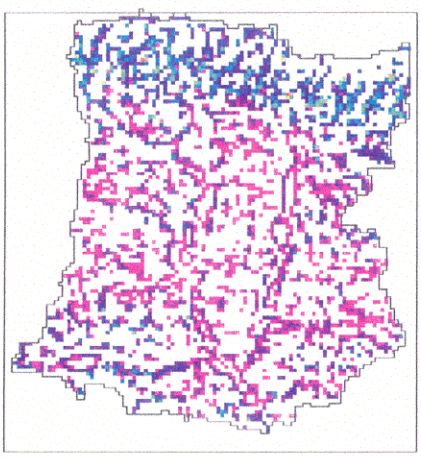

SIR-C Runoff Production

average runoff depth = 1.7 mm

maximum runoff depth = 13.0 mm

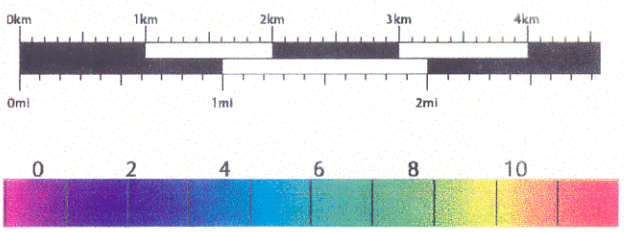

Runoff Production (mm) on Dec 14, 1983, 3 pm

Figure 37. **Spatial distribution of runoff production, December 14, 1983**

7.3 Streamflow

Simulated streamflow volumes were found to vary between the three DEMs in a consistent fashion. Mean runoff volumes were lowest when predicted by the reference DEM. The USGS and SIR-C DEMs predicted average annual flows that were 0.3% and 7.0% larger, respectively (Table 14 and Table 15). The distinct increase in predictions by the SIR-C DEM is attributable to the 3.6% larger basin area and a higher basin average elevation. The basin average elevation is affected by the datum shift selected for the SIR-C DEM which was chosen to adjust the DEM to a consistent basin outlet elevation.

Table 14. Annual summary of flows (cms)

Year	*Observed*	*Reference DEM*	*USGS DEM*	*SIR-C DEM*
1983-1984	0.1802	0.1689	0.1692	0.1790
1984-1985	0.0747	0.0794	0.0781	0.0836
1985-1986	0.1557	0.1508	0.1534	0.1649
1986-1986	0.1150	0.1189	0.1188	0.1266
Average	0.1314	0.1295	0.1299	0.1386

Time series plots were examined for individual events series (Figure 38 - Figure 41) for each water year (Appendix D). These hydrographs showed that the reference simulation had a higher peak and lower recession than flows simulated with the USGS and SIR-C DEMs. These differences could be expected from the differences in the topographic index. The USGS and SIR-C DEMs had higher lower topographic indices which indicates a lower runoff production capacity. The SIR-C DEM is less smooth than the reference DEM with abrupt changes in slope and a meandering channel that could not transport water to saturated pixels as efficiently as the reference DEM. Surface flow was reduced by the lack of defined channel network. The USGS DEM had a smaller average contributing area which resulted in shorter travel times to the outlet and lower peak flows.

Table 15. Monthly summary of flows during four simulation years (cms)

	Observed	*Reference DEM*	*USGS DEM*	*SIR-C DEM*
October	0.0318	0.0672	0.0615	0.0649
November	0.1556	0.1352	0.1324	0.1339
December	0.2073	0.2204	0.2300	0.2596
January	0.0726	0.1243	0.1271	0.1293
February	0.2388	0.1923	0.1928	0.1950
March	0.1803	0.1791	0.1819	0.1955
April	0.2267	0.1685	0.1708	0.1865
May	0.1246	0.0909	0.0890	0.0926
June	0.1025	0.0958	0.0949	0.1037
July	0.0595	0.0787	0.0775	0.0798
August	0.1032	0.0912	0.0911	0.1015
September	0.0739	0.1101	0.1098	0.1204
Average	0.1314	0.1295	0.1299	0.1386

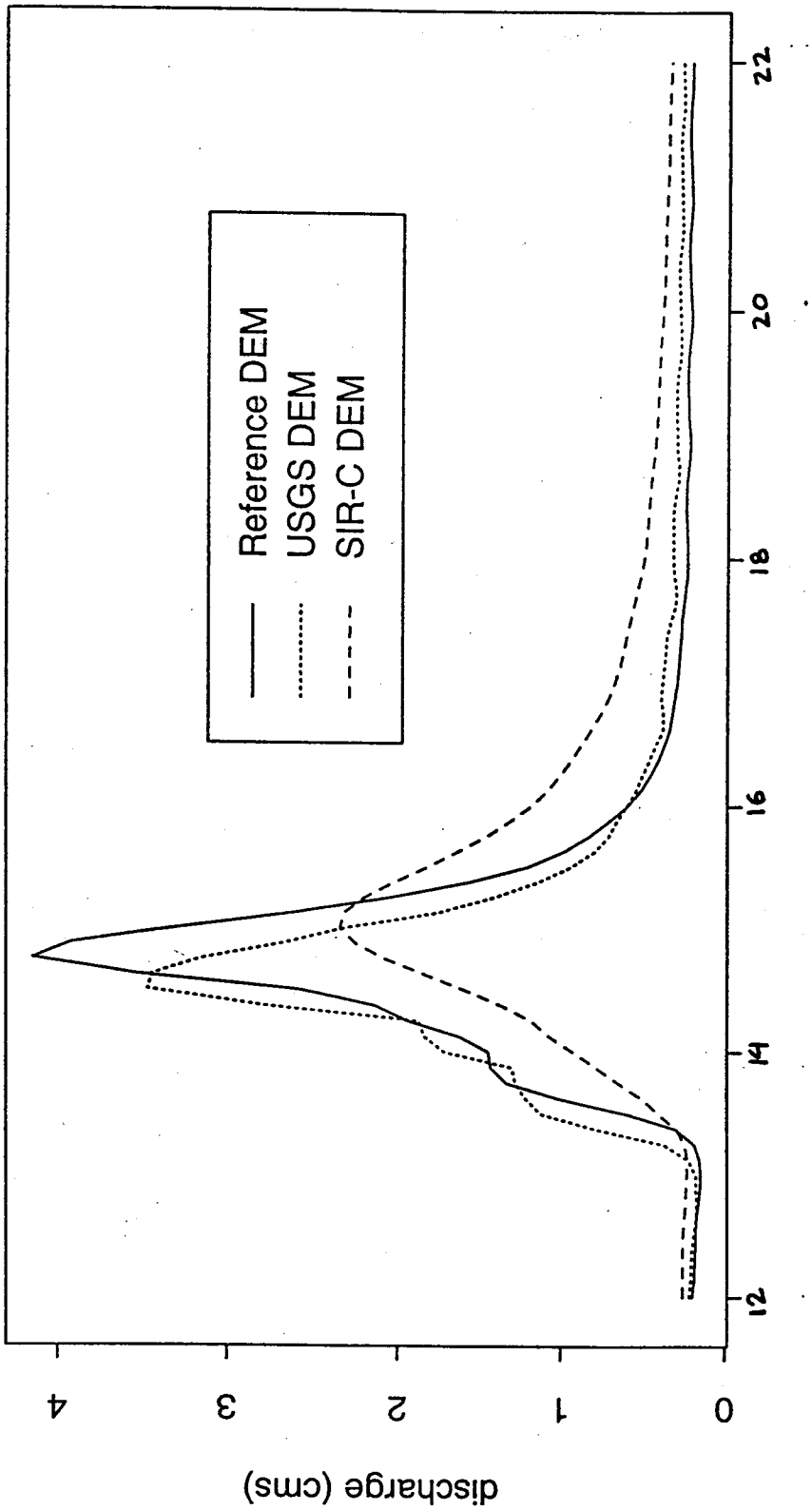

Figure 38. Simulated high flow event, December 14, 1983

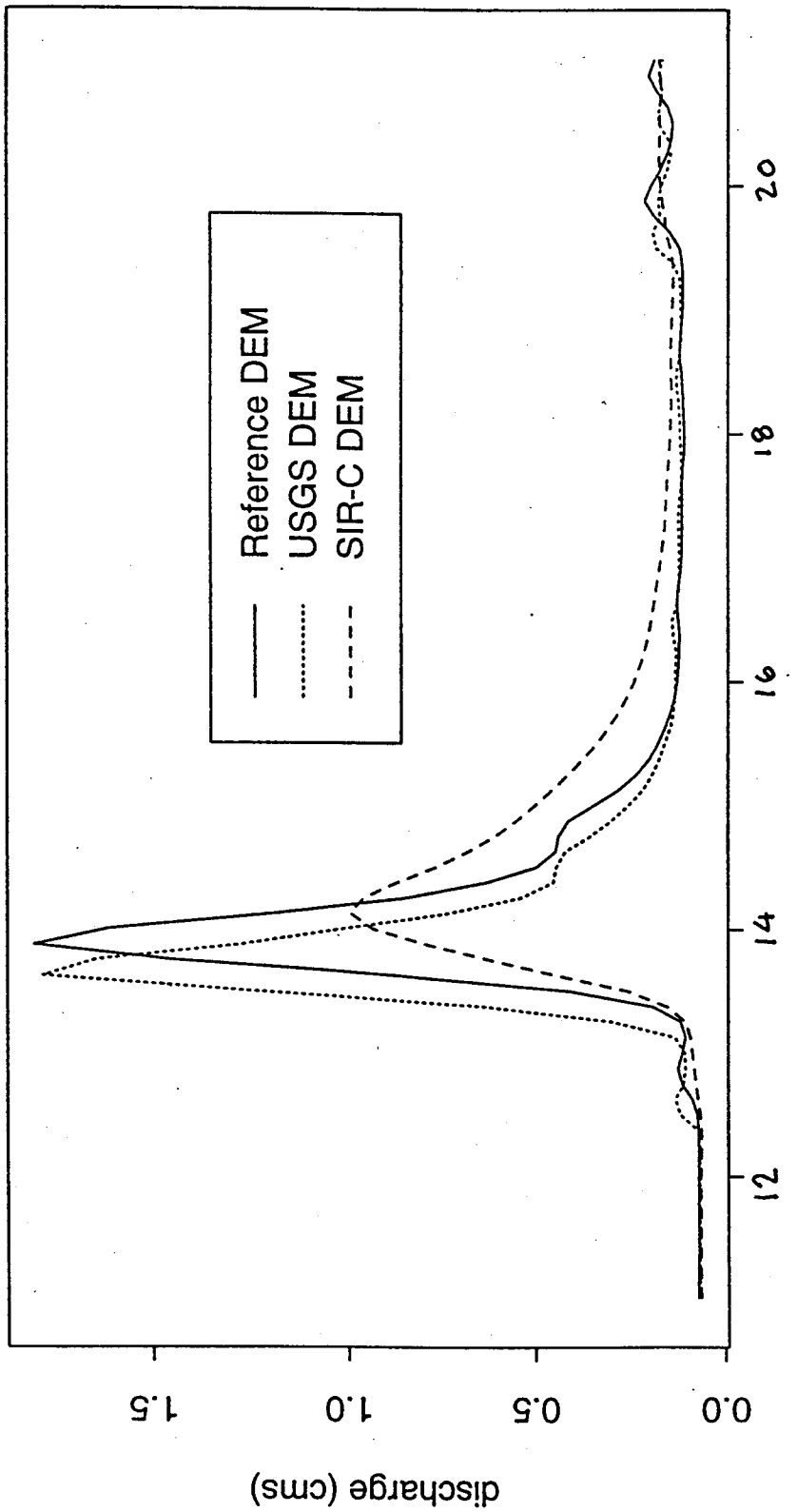

Figure 39. Simulated high flow event, February 13, 1985

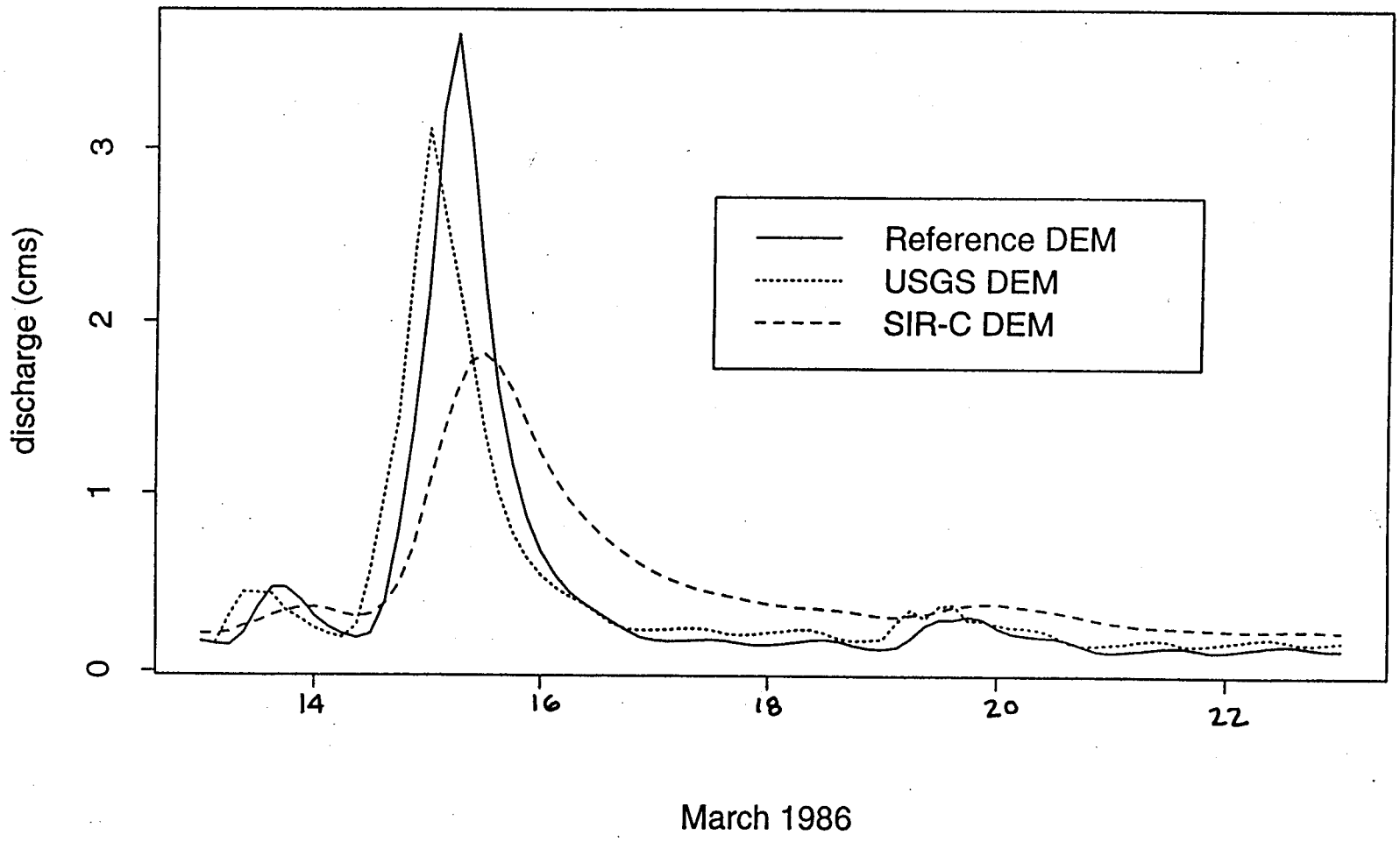

Figure 40. Simulated high flow event, March 15, 1986

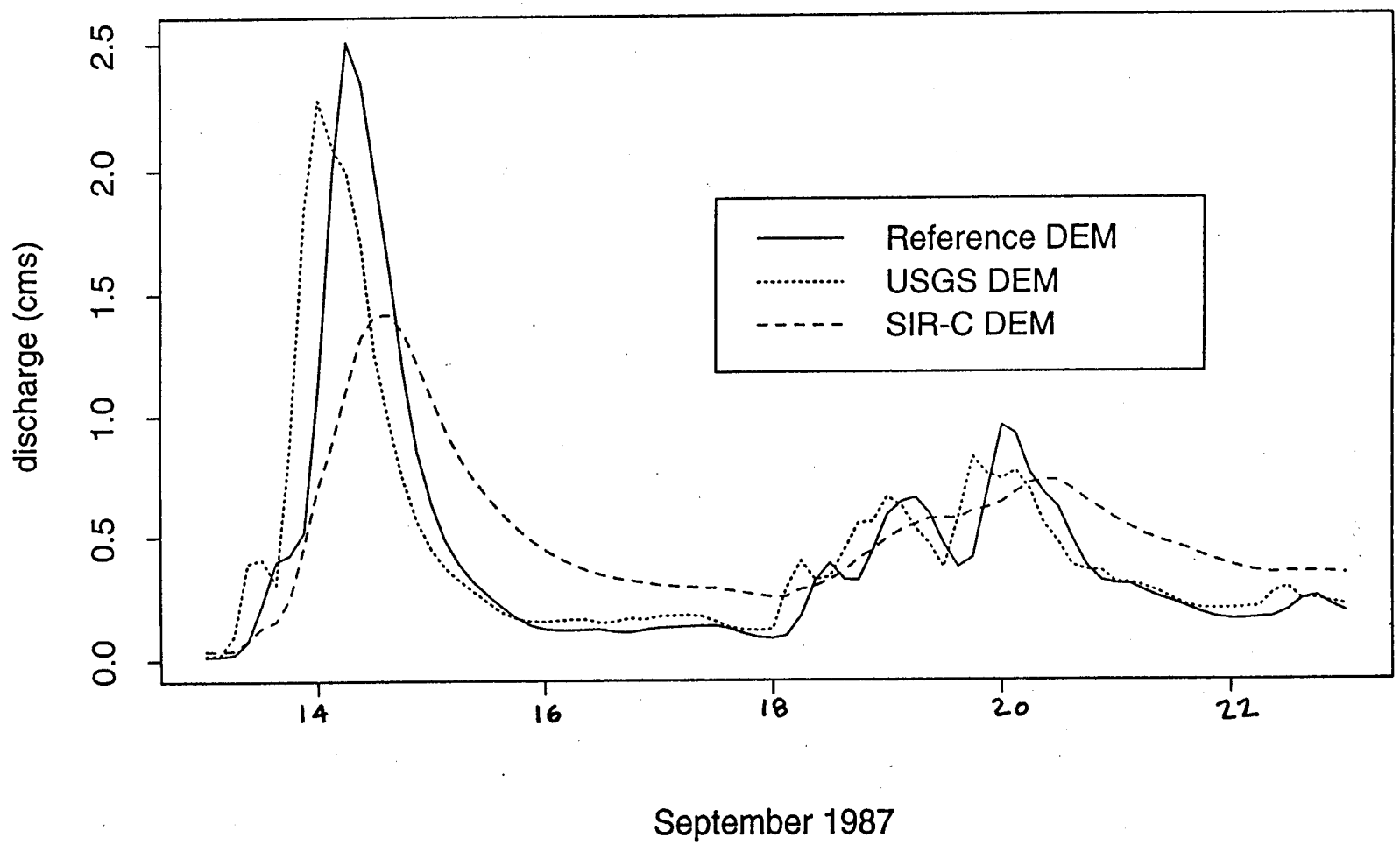

Figure 41. Simulated high flow event, September 14, 1987

8. Conclusions and Recommendations for Further Research

8.1 Summary

A high resolution 5 m DEM was derived from low altitude aerial photography of the USDS-ARS experimental watershed in the Mahantango basin. This DEM was aggregated to a 30 m resolution using code provided by Barros and Bindlish (1996) based on their modified fractal interpolation scheme and used as a reference DEM. The reference DEM was compared to the standard 30 m USGS 7.5' DEM and a third DEM produced by NASA/JPL using interferometric processing of SIR-C images.

ARC/INFO algorithms were used to delineate the watershed boundaries using each DEM and to calculated basin area and outlet elevation. Elevation differences between the reference product and the USGS and SIR-C DEMs were calculated and analyzed spatially and statistically. Nine check points on the watershed were compared to the elevations reported in each DEM. The basin topographic attributes of slope, contributing area and topographic index were calculated from each DEM and compared spatially and statistically.

Differences between the USGS and reference DEMs were studied to determine the source of the errors and any correlation between the elevation differences and the topographic parameters. Correction algorithms were applied in an attempt to correct the systemic errors observed in the USGS DEM.

DHSVM was calibrated with the reference product for the Mahantango Basin. Flow and moisture fluxes were predicted using each of the 30 m DEMs for a four year period beginning October 1, 1983. Spatial images of the instantaneous depth to saturation and runoff production were examined and compared to the spatial distribution of parameters derived directly from the DEMs. Predicted runoff volumes were compared on an annual and monthly basis and individual events were analyzed to determine the dependence of the shape and timing of the runoff hydrograph to the DEM used for the hydrologic simulation.

8.2 Results and Discussion

Significant elevation differences were found between the reference DEM derived from high resolution aerial photography and the DEMs derived by standard USGS methods and SIR-C interferometry.

The standard USGS DEM displayed two distinct errors: a systemic grid-type error due to the edge effect introduced during the automated scanning of the NHAP photographs in small patches; and a error pattern which reflected the basin topography attributable to a lack of correlation between the two photographs. Neither error could be eliminated using Felicimo's parametric test because the errors were not strictly local but instead were consistent over a patch or topographic area. Linear relationships were found between the USGS elevation differences and topographic parameters for some individual patches a clear error structure could not be determined for the entire watershed or by different terrain area because of the wide range of error sources.

The watershed boundaries delineated from the USGS DEM were more irregular than those determined with the reference product although the basin drainage areas agreed to 0.04%. The USGS DEM contained more sink pixels than the reference DEM (110 and 5 sink pixels, respectively) and was higher on average (+7.5 m) and at the outlet (+22.1 m). The valley network was visible on the USGS DEM and in spatial images of topographic parameters although it was less distinct than in the reference product. This is due in part to error in the USGS DEM within the valley bottoms and the edge matching error which resulted in a misalignment of the drainage network.

The SIR-C DEM differed visibly from the reference, particularly in areas of high slopes. The spatial image has a scattered appearance with rough boundaries. The watershed area delineated from the SIR-C DEM was 3.6% larger than the reference area, 4.5% of its pixels did not drain and required filling, and the elevations were consistently lower (-50.5 m at the outlet). The difference in elevation was attributed to a datum error and the DEM was uniformly elevated by 50.5 m . The resulting average elevation was 8.1 meters higher than the reference product, indicating that the error was not consistent

across the basin. Comparison of the spatial distribution of topographic parameters confirmed that reference DEM better represented the physical attributes of the watershed. The valleys defined by the SIR-C DEM were more meandering with more higher order tributaries.

DHSVM was used to simulate runoff production in the Mahantango Basin for the four year period beginning October 1, 1983, using each of the DEMs. Differences in predictions were always more significant between the SIR-C and references DEMs than between the USGS and reference DEMs, which is consistent with the direct comparisons of these products. The USGS standard and SIR-C DEMs predicted average annual flows that were 0.3% and 7.0% larger those predicted by the reference DEM, respectively. The small increase using the USGS DEM for predictions is attributable to the higher basin average elevation while the higher predictions using the SIR-C DEM are caused by the higher basin average elevation combined with a larger drainage area.

Differences in the DHSVM spatial predictions of depth to saturation and runoff production reflected the differences seen in the spatial images of topographic parameters. This is because the runoff producing tendency of a cell is related to slope and contributing area, although these parameters are not used explicitly in DHSVM which works directly from the elevation.

The shape and timing of simulated runoff hydrographs for individual events also differed for the three DEMs. The USGS DEM predicted lower peaks that rose sooner which reflects the small contributing area seen in the USGS DEM. The SIR-C DEM resulted in the lowest peaks with higher base as a result of increased subsurface flow due to irregular slopes and a poorly defined stream channel. The version of DHSVM used in this study simulates saturated flow from each pixel to the basin outlet separately using a convolution algorithm and combines these responses to determine basin outflow. The latest version of DHSVM, which includes an imposed channel network and allows reinfiltration of surface water, will be more sensitive to the errors observed in the low accuracy DEMs.

8.3 Conclusions

The DEM data currently available from radar and satellite imaging were found to be inappropriate for prediction of individual storm hydrographs but they could be applicable to large scale models or for bulk runoff volume predictions. The total predicted runoff volume depended on the average elevation and basin area of the DEM. This implies that the model calibration is dependent on the DEM. The spatial distribution of moisture fluxes and the predicted storm hydrographs for single events indicated that the SIR-C DEM could not properly represent the hydrologic behavior of the watershed.

The type of errors present in the SIR-C DEM did not indicate any particular source of error to be addressed, however the quantity of the errors necessitates higher resolution products to correctly simulate the hydrologic response of a basin to individual storm events or when peak flow volumes are of interest.

8.4 Recommendations for further research

On-going research for this project by others will compare TOPMODEL predictions with digital elevation data for a different study site. This will help to determine whether the results of the current study are independent of basin size, topography, vegetation and soil type. An investigation of prediction differences in areas of different climate would also be of interest. Topographic influences on estimations of solar radiation and snowmelt could be examined in a basin that develops a more significant snowpack.

Additional research on this topic could further investigate the expected vertical accuracy of DEMs. The standard USGS DEM used for this study was the lowest accuracy product available. Standard USGS DEMs of different classifications could be compared to give an indication of the reliability of the newer products. The SIR-C DEM used in this study was a preliminary product developed specifically for this project. The image processing should be finalized and compared to the preliminary product to assess any improvements in accuracy. A smoothing algorithm could be used to reduce the abrupt changes in

slope that are present in the preliminary DEM. The 50.5 m datum error in DEM should also be resolved to give a true indication of the basin elevations.

Improvements could also be made to the DHSVM representation of the surface flow in the Mahantango Basin. An explicit channel routing scheme would provide a more accurate definition of hydrologic processes on the watershed and would be more sensitive to differences in digital elevation data.

List of References

Anderson, E.A., Development and testing of snowpack energy balance equations, *Water Resources Research*, 4(1), 19-37, 1968.

Arola, A. and D.P. Lettenmaier, Effects of subgrid spatial heterogeneity on GCM-scale land surface energy and moisture fluxes, *Journal of Climate*, in press, 1996.

Beven, K.J. and M.J. Kirkby, A physically based, variable contributing area model of basin hydrology, *Hydrological Sciences Bulletin*, 24(1), 43-69, 1979.

Blair, J.B. and D.J. Harding, Scanning Lidar Imager of Canopies by Echo Recovery (SLICER), Three-dimensional Canopy Structure: Measurement by Laser Altimeter Waveforms, *http://ltpwww.gsfc.nasa.gov/eib/slicer.html*, 1996.

Bindlish, R. and A.P. Barros, Aggregation of digital terrain data using a modified fractal interpolation scheme, *Computers & Geosciences*, 22(3), 907-917,1996.

Bowling, L.C., D.P. Lettenmaier, Wigmosta, M.S. and W.A. Perkins, Predicting the effects of forest roads on streamflow using a distributed hydrologic model, *EOS Transactions AGU*, 77(46) Fall Meeting Supplement H22A, 1996.

Bras, R.L., *Hydrology: An introduction to hydrologic science*, Addison-Wesley Publishing Company, Inc., Reading, MA, 1990.

Carter, J.R., Relative errors identified in USGS gridded DEMs, *Auto-Carto 9: Ninth International Symposium on Computer Assisted Cartography*, 255-263, 1989.

Costa-Cabral, M.C. and S.J. Burges, Digital elevation model networks (DEMON): A model of flow over hillslopes for computation of contributing and dispersal areas, *Water Resources Research*, 30(6), 1681-1692, 1994.

Cox, B.L. and J.S.Y. Wang, Fractal surfaces: Measurement and applications in the earth sciences, *Fractals*, 1(1), 87-115, 1993.

Delft Institution for Earth-Oriented Research (DEOS), Delft University of Technology, The ERS Satellites, *http://dutlru8.lr.tudelft.nl/ers1/*,1996.

Dubayah, R., J. Dozier and F.W. Davis, Topographic distribution of clear-sky radiation over the Konza Prarie, Kansas, *Water Resources Research*, 26(4), 679-690, 1990.

Felicisimo, A.M., Parametric statistical method for error detection in digital elevation models, *ISPRS Journal of Photogrammetry and Remote Sensing*, 49(4), 29-33, 1994.

Frew, J.E., *The image processing workbench*, Ph.D. thesis, Department of Geography, University of California, Santa Barbara, 1990.

Gyasi-Agyei, Y., G. Willgoose and F.P. De Troch, Effects of vertical resolution and map scale of digital elevation models on geomorphological parameters used in hydrology, *Hydrological Processes*, 9, 363-382, 1995.

Hannah, M.J., Error detection and correction in digital terrain models, *Photogrammetric Engineering and Remote Sensing*, 47(1), 63-69, 1981.

Huang, J. and D.L. Turcotte, Fractal mapping of digitized images: application to the topography of Arizona and comparisons with synthetic images, *Journal of Geophysical Research*, 94(B6), 7491-7495, 1989.

Hutchinson, M.F, A new procedure for gridding elevation and streamline data with automatic removal of spurious pits, *Journal of Hydrology*, 106, 211-232, 1989.

Kelly, R.E., P.R.H. McConnell and S.J. Mildenberger, The gestalt photomapping system, *Photogrammetric Engineering and Remote Sensing*, 43(11), 1407-1471, 1977.

Lam, N.S. and L. De Cola, *Fractals in Geography*, PTR Prentice Hall, Inc., New Jersey, 1993.

Longley, K., D. Jacobsen and D. Marks, *Supplement to the image processing workbench (IPW)*, report, Environmental Research Lab, U.S. Environmental Protection Agency, Corvallis, Oregon, 1992.

Leung, L.R. and S.J. Ghan, A subgrid parameterization of orographic precipitation, *Theoretical and Applied Climatology*, 52, 95-118, 1995.

Leung, L.R., M.S. Wigmosta, S.J. Ghan, D.J. Epstein and L.W. Vail, Application of a subgrid orographic precipitation/surface hydrology scheme to a mountain watershed, *Journal of Geophysical Research*, 101, 12,803-12,817, 1996.

Maidment, D.R., *Handbook of Hydrology*, McGraw-Hill, Inc., New York, 1993.

Mark, D.M. and P.B. Aronson, Scale-dependent fractal dimensions of topographic surfaces: An empirical investigation, with applications in geomorphology and computer mapping, *Mathematical Geology*, 16(7), 671-683, 1984.

Mandelbrot, B.B., How long is the coast of Britain? Statistical self-similarity and fractional dimension, *Science*, 156, 636-638, 1967.

Mandelbrot, B.B., *The Fractal Geometry of Nature*, W.H. Freeman and Company, New York, 1982.

Miller, J.R. and G.L. Russell, The impact of global warming on river runoff, *Journal of Geophysical Research*, 97(D3), 2757-2764, 1992.

Moore, I.D., R.B. Grayson and A.R. Ladson, Digital terrain modeling: A review of hydrological, geomorphological, and biological applications, *Hydrological Processes*, 5, 3-30, 1991.

Moore, I.D. and M.F. Hutchinson, Spatial Extension of hydrologic process modeling, *International Hydrology & Water Resources Symposium*, 803-808, 1991.

Nijssen, B., D.P. Lettenmaier, Wigmosta, M.S. and W.A. Perkins, Testing an imposed channel network algorithm for hydrograph prediction with a distributed model, *EOS Transactions AGU*, 77(46) Fall Meeting Supplement H22A, 1996.

Nijssen, B., I. Haddeland, and D.P. Lettenmaier, Point evaluation of a surface hydrology model for BOREAS, *Water Resources Research*, in press, 1996.

O'Loughlin, E.M., Prediction of surface saturation zones in natural catchments by topographic analysis, *Water Resources Research*, 22(5), 794-804, 1986.

Palacios-Velez, O.L. and B. Cuevas-Renaud, Automated river-course, ridge and basin delineation from digital elevation data, *Journal of Hydrology*, 86, 299-314, 1986.

Perkins, W.A., Wigmosta, M.S. and B. Nijssen., Development and testing of road and stream drainage simulation within a distributed model, *EOS Transactions AGU*, 77(46) Fall Meeting Supplement H22A, 1996.

Pierce, L.E., F.T. Ulaby, K. Sarabandi and M.C. Dobson, Knowledge-based classification of polarimetric SAR images, *IEEE Transactions on Geoscience and Remote Sensing*, 32(5), 1081-1086, 1994.

Pionke, H.B., J.R. Hoover, R.R. Schnabel, W.J. Gburek, J.B. Urban, and A.S. Rogowski, Chemical-hydrologic interactions in the near-stream zone, *Water Resources Research*, 24(7), 1101-1110, 1988.

Pionke, H.B. and H.M. Kunishi, Phosphorous status and content of suspended sediment in a Pennsylvania watershed, *Soil Science*, 153(6), 452-462, 1992.

Quinn, P.F., K.J. Beven, P. Chevallier and O. Planchon, The prediction of hillslope flow paths for distributed hydrological modeling using digital terrain models, *Hydrological Processes*, 5, 59-79, 1991.

Quinn, P.F., K.J. Beven and R. Lamb, The $\ln(a/\tan\beta)$ index: How to calculate it and how to use it within the TOPMODEL framework, *Hydrological Processes*, 9, 161-182, 1995.

Rao, K.S., Y.S. Rao and R. Gurusamy, Frequency dependence of polarization phase difference and polarization index for vegetation covered fields using polarimetric AIRSAR data, *IGARRS '93*, 13(1), 37-39, 1993.

Roy, A.G., G. Gravel and C. Gauthier, Measuring the dimension of surfaces: A review and appraisal of different methods, *Auto-Carto 7*, 69-77, 1987.

Smith, C.B., M.N. Lakhtakia, W.J. Capehart and T.N. Carlson, Initialization of soil-water content in regional-scale atmospheric prediction models, *Bulletin of the American Meteorological Society*, 75(4), 585-593, 1994.

Storck, P., D.P. Lettenmaier, B.A. Connelly, and T.W. Cundy, *Implications of forest practices on downstream flooding*, Phase II report to Water Forest Protection Association, King County Surface Water Management Division, Weyerhauser Co., and U.S. Forest Service, University of Washington, 1985.

Turcotte, D.L., *Fractals and chaos in geology and geophysics*, Cambridge University Press, Cambridge, 1992.

U.S. Geological Survey (USGS), National Geospatial Data Clearinghouse, Digital chart of the world derived DEM Data, *http://edcwww.cr.usgs.gov/landdaac/30asdcwdem/30asdcwdem.html*, 1996a.

U.S. Geological Survey (USGS), Eros Data Center, SPOT High Résolution Visible Data, *http://edcwww.cr.usgs.gov/glis/hyper/guide/spot*, 1996b.

U.S. Geological Survey (USGS), Digital elevation models, *Data users guide 5*, National Mapping Program, 1993.

Wetherbee, P. and D.P. Lettenmaier, *Application of the distributed hydrology-soil-vegetation model (DHSVM) to the Little Naches Basin in the context of watershed analysis*, report to Plum Creek Timber Company and NCASI, University of Washington, 1996.

Wallace, J.M., S. Tibaldi and A.J. Simmons, Reduction of systematic forecast errors in the ECMWF model through the introduction of an envelope orography, *Quarterly Journal of the Royal Meteorological Society*, 109(462), 683-717, 1983.

Warner, E. and T. Troutman, unpublished data, Office for Remote Sensing of Earth Resources, Environmental Resources, Research Institute, Pennsylvania State University, 1996.

White, R.A., Pennsylvania State EOS Database, Pennsylvania State University, *http://eoswww.essc.psu.edu/eosdb.html*, 1996.

Wigmosta, M.S., L.W. Vail and D.P. Lettenmaier, A distributed hydrology-vegetation model for complex terrain, *Water Resources Research*, 30(6), 1665-1679, 1994.

Wolock, D.M. and C.V. Price, Effects of digital elevation model map scale and data resolution on a topography-based watershed model, *Water Resources Research*, 30(11), 3041-3052, 1994.

Zebker, H.A., S.N. Madsen, J. Martin, K.B. Wheeler, T. Miller, Y. Lou, G. Alberti, S. Vetrella, and A. Cucci, The TOPSAR interferometric radar topographic mapping instrument, *IEEE Transactions on Geoscience and Remote Sensing*, 30(5), 933-940, 1992.

Zhang, W. and D.R. Montgomery, Digital elevation model grid size, landscape representation and hydrologic simulations, *Water Resources Research*, 30(4), 1019-1028, 1994.

Appendix A Fractal Dimension

The length of a coastline, measured by a rod of a specified length, varies with rod length according to a power law. The power of this relationship determines the fractal dimension of the coastline. Mandelbrot (1967) introduced the concept of a fractal based on this premise.

A.1 Definitions

The *fractal dimension*, D, is defined as:

$$N(x) = Lx^{-D} \tag{A.1}$$

where L is a distance along a surface or line which is measured in N discrete steps of length x. The value of D characterizes the intricacy or jaggedness of an entity where D = 1 defines a straight line, D = 2 defines a plane, and D = 3 is the dimension of independent random heights or spatial "white noise". Mandelbrot (1977) used the term *fractal* to refer to any geometric phenomenon with a fractal dimension greater than its topographic dimension and *fractional Brownian surface* to describe a class of single-valued fractal surfaces with $2 < D < 3$.

In a *self-similar fractal*, the phenomenon being measured is isotropic and results are independent of the orientation of the coordinate axes. In two-dimensional xy-space, a self-similar fractal f(rx,ry) is statistically similar to f(x,y) where r is a scaling factor. The fractal dimension of a self-similar fractal is constant. Topography is often self-similar in the horizontal dimension.

A *self-affine fractal* is anisotropic and the coordinates are scaled by different factors. Topographic elevation is an example of self-affinity, the vertical coordinate is statistically related to the horizontal coordinate but has a systematically smaller magnitude. In two-dimensional space, $f(rx, r^H y)$ is

statistically similar to f(x,y) where H is the Hausdorff measure (Turcotte, 1992). The expected difference of the squared elevation difference between two points is given by:

$$E\left[\left(Z_p - Z_q\right)^2\right] \sim \left(d_{pq}\right)^{2H} \qquad (A.2)$$

where Z_p and Z_q are the elevations of the surface at points p and q, d_{pq} is the horizontal distance between the points p and q, and H= (2 - D) in 1 dimension and $(3 - D_{2D})$ in two dimensions (Mark and Aronson, 1984).

A.2 Measurement techniques

A variety of methods have been suggested to calculate the fractal dimension of a surface. In a fractal and self-similar surface, the value of D should theoretically be in agreement regardless of the method used (Roy et al, 1987). In reality, natural surfaces depart from strict self-affinity and the differences among the algorithmic approaches and assumptions of the different methods of determining D are often so significant that comparisons of D values derived by different techniques are not valid (Lam and De Cola, 1993).

The ruler method or structured walk technique is the original method of measuring D and involves measurement of the number of steps corresponding to a given ruler length for a range of ruler lengths. D is then one minus the slope of a log-log plot of curve length (number of steps times ruler length) versus the ruler length (x-axis). For a two-dimensional surface, a series of profiles along the surface are measured and all data are plotted on one graph to determine D as two minus the slope.

The box method uses boxes to measure the curve and D is defined as the slope of the log-log plot of the number of boxes versus the inverse of the box size (x-axis). Surfaces are represented as profiles and

D is then one plus the slope. This method may be applied to non-isotropic surfaces by converting the squares to rectangles where the aspect ratio represents the ratio of the anisotropic scaling factor (Cox and Wang, 1993).

A.3 Variogram analysis

Mark and Aronson (1984) presented a variogram method to calculate the fractal dimension, D, of a topographic surface. The variogram is a measure of the spatial correlation of a regionalized variable. For this application, elevation was chosen as the regionalized variable. The variogram is then a function that describes the relationship between the mean-square difference of the elevations, z_p and z_q, and their intervening horizontal separation distance, d_{pq}.

The variogram, $2\gamma(h)$, and the semi-variogram, $\gamma(h)$, is mathematically defined by:

$$\gamma(h) = \frac{1}{2}\sum_{i=1}^{n}\left[z_p - z_q\right]^2 \qquad (A.3)$$

where h is equivalent to d_{pq} in all directions.

The method assumes that the image can be modeled as a fractional Brownian motion such that there is a distinct relationship between the distance between two pixels and the variance of the difference in the pixel values as described in Equation A.2. The variogram is the average variance of elevation versus the separation distance. On a log-log plot, the slope of the variogram, b, is equal to 2H. The fractal dimension, D_{2D}, is calculated as 3-(b/2).

The raw variogram for the Mahantango Creek research watershed was determined directly from the digital elevation data by calculating the separation distance and variance between elevation pairs within the basin. The watershed is defined by 8000 30 m pixels; the number of possible pairs is (8000)(7999)/2 = 3.20 x 10^7. Instead of using all 8000 points, 200 points were randomly sampled selected from the data set. The separation distance and variance were computed between each combination

and the average variance was calculated for 10 separation ranges. This process was repeated 100 times, resulting in 100 average variance values for each range.

During the application of this technique, it was found that D changes with scale which suggests that self-affinity was only approached over restricted scale ranges and that an appropriate range of analysis should be selected.

A.4 Spectral analysis

Topographic data, z_{xy}, can be converted to the frequency domain in terms of its amplitude, h_{st}, at different frequencies, Z_{uv}, by a Fourier transform. Two dimensional analysis may be based on Fourier transforms along profiles or on a two-dimensional discrete Fourier transform over the surface as suggested by Turcotte (1992). Using a 2D Fourier transform, the amplitudes in the frequency domain are defined as:

$$H_{uv} = \left(\frac{L}{N}\right)^2 \sum_{x=0}^{N-1} \sum_{y=0}^{N-1} z_{xy} e^{\left[-\frac{2\pi i}{N}(ux+vy)\right]} \tag{A.4}$$

where u represents the transform in the x-direction (u = 0, 1, 2, ..., N-1), v represents the transform in the y-direction, (v = 0, 1, 2, ..., N-1), and N is the order of the equally spaced two dimensional square grid of linear size L. Each transform amplitude, H_{uv}, is assigned a radial wave number, k, as:

$$k = \frac{2\pi}{\sqrt{u^2 + v^2}} \tag{A.5}$$

and the two dimensional power spectral density, S_{2j}, for each radial wave number k_j is defined as:

$$S_{2j} = \frac{1}{L^2 N_j} \sum_{1}^{N_j} |H_{uv}|^2 \tag{A.6}$$

where N_j is the number of coefficients that satisfy the condition $j < (2\pi/k) < j + 1$ and the summation is carried out over all the coefficients H_{uv} in this range.

The dependence of the mean power spectral density on the radial wave number for a fractal distribution is:

$$S_{2j} \sim k_j^{-\beta-1} \tag{A.7}$$

Equating the powers of Equations A.2 and A.7 yields $(-\beta-1) = 2H$ where $H = 3-D_{2D}$. The fractal dimension is determined from the slope of the log-log plot of the power spectral density function of power spectral density, S, versus the radial wave number, k as:

$$D = \frac{7-\beta}{2} \tag{A.8}$$

The log-log spectral plots are not as linear as the plots derived using other methods and the slope is dependant on the selected range of the linear portion of the curve.

A.5 Fractal Dimension

The fractal dimensions of the standard and high resolution DEMs were determined using variogram analysis as discussed in Section A.3 and are displayed in Table A.1. The variogram for the 5 m high resolution DEM is displayed in Figure A.1. D of the fractally aggregated 30 m high resolution is higher than the D of the DEM aggregated by simple averaging. This is expected, as averaging acts as a low pass filter which will result in smoother the elevation data and a lower D. The D values are very similar for all the DEMs, differences are less than the expected accuracy of the variogram method.

Table A.1 Fractal dimension of DEMs

DEM	*grid size*	*aggregation method*	*D*
high resolution	5 m	n/a	2.385
high resolution	30 m	fractal interpolation	2.391
high resolution	30 m	simple averaging	2.390
standard USGS	30 m	n/a	2.399

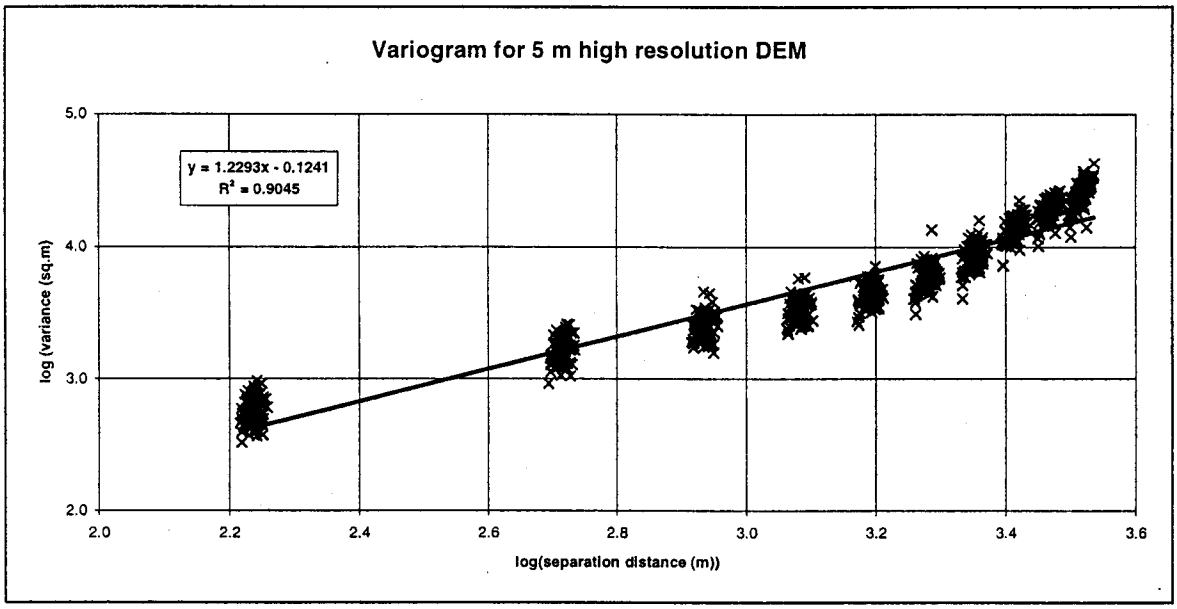

Figure A.1. Variogram for 5 m high resolution DEM

Appendix B Soil and Vegetation Classes

Table B.1 Overstory parameters

	urban	*tall vegetation*	*short vegetation*	*bare surfaces*
canopy attenuation coefficient	0.5	0.5	0.5	0.5
summer overstory leaf area index (LAI)	8.0	8.0	8.0	8.0
winter overstory LAI	2.0	2.0	2.0	2.0
overstory albedo	0.18	0.18	0.18	0.18
maximum overstory height (m)	15.0	15.0	15.0	15.0
exponential windspeed decay coefficient	1.5	1.5	1.5	1.5
displacement height ratio (d/h)	0.63	0.63	0.63	0.63
roughness length ratio (z/h)	0.13	0.13	0.13	0.13
max overstory fractional coverage	0.05	0.9	0.05	0.05
overstory maximum stomatatal comductance (m/hr)	10.8	10.8	10.8	10.8
overstory minimum stomatatal comductance (m/hr)	3.6	3.6	3.6	3.6
critical soil moisture content for overconductance	0.33	0.33	0.33	0.33
overstory light level	0.108	0.108	0.108	0.108
fraction of overstory roots in rooting zone 1	0.5	0.5	0.5	0.5

Table B.2 Understory parameters

	urban	*tall vegetation*	*short vegetation*	*bare surfaces*
summer understory LAI	1.0	1.0	2.5	1.0
winter understory LAI	0.1	0.1	0.1	0.1
understory albedo	0.1	0.2	0.23	0.1
maximum understory height (m)	0.1	0.1	1.5	0.1
vapor pressure deficit adjustment coefficient	1.0	1.0	1.0	1.0
understory max stomatatal comductance (m/hr)	14.4	14.4	14.4	14.4
understory min stomatatal comductance (m/hr)	0.72	0.72	0.72	0.72
critical soil moisture content for overconductance	0.13	0.13	0.13	0.13
understory light level	0.108	0.108	0.108	0.108
bare ground albedo	0.1	0.1	0.1	0.1
ground roughness length (z/h)	0.01	0.01	0.01	0.01
snow albedo	0.7	0.7	0.7	0.7

Table B.3 Soil Classes

soil class	*depth_1*	*depth_2*	*sat*	*conduct_exp*	*s_air*	*sk*	*field_cap*	*sm_wiltp*
1	0.25	0.25	0.501	0.19	0.21	0.03591	0.25	0.08
2	0.25	0.25	0.501	0.19	0.21	0.03591	0.25	0.08
3	0.25	0.25	0.501	0.19	0.21	0.03591	0.25	0.08
4	0.25	0.25	0.501	0.19	0.21	0.07315	0.25	0.08
5	0.25	0.25	0.501	0.19	0.21	0.05680	0.25	0.08
6	0.25	0.25	0.501	0.19	0.21	0.03591	0.25	0.08
7	0.25	0.25	0.453	0.19	0.15	0.08961	0.25	0.12
8	0.25	0.25	0.501	0.19	0.21	0.05680	0.25	0.08
9	0.25	0.25	0.501	0.19	0.21	0.08961	0.25	0.08
10	0.25	0.25	0.463	0.19	0.11	0.08961	0.25	0.12
11	0.25	0.25	0.501	0.19	0.21	0.05680	0.25	0.08
12	0.25	0.25	0.501	0.19	0.21	0.03591	0.25	0.12
13	0.25	0.25	0.501	0.19	0.21	0.08961	0.25	0.08
14	0.25	0.25	0.501	0.19	0.21	0.03591	0.25	0.08
15	0.25	0.25	0.501	0.19	0.21	0.07315	0.25	0.08

Soil parameters are defined as:

vpd_g_coef: vapor pressure deficit adjustment for the ground

depth_1: depth of rooting zone 1 (m)

depth_2: depth of rooting zone 2 (m)

sat: saturated water holding capacity or porosity

conduct_exp: m coefficient in Brooks-Corey (1/b from Campbell)

s_air: bubbling pressure of the soil (m of H2O)

sk: vertical saturated hydraulic conductivity of the soil (m/hr)

field_cap: field capacity of the soil

sm_wiltp: wilting point of the soil

Appendix C DHSVM Spatial Predictions of Soil Moisture

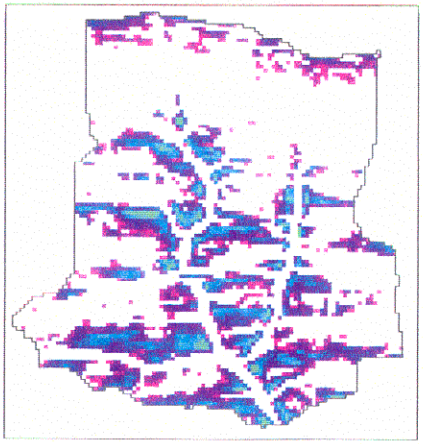

Reference Depth to Saturation

average depth = 200 mm

maximum depth = 626 mm

USGS Depth to Saturation

average depth = 234 mm

maximum depth = 677 mm

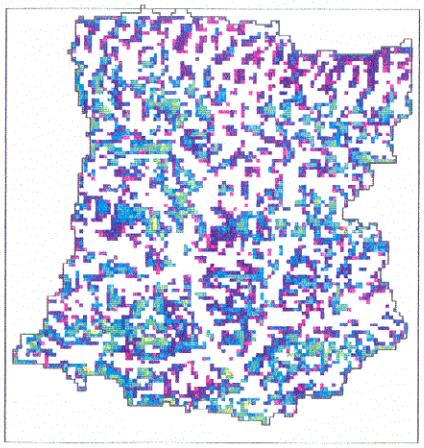

SIR-C Depth to Saturation

average depth = 298 mm

maximum depth = 894 mm

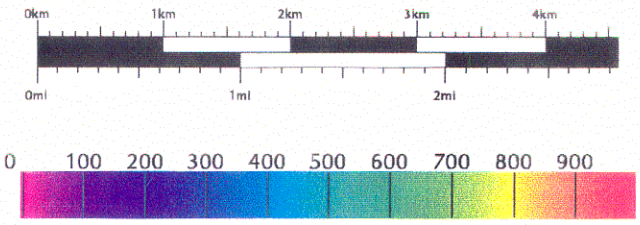

Depth to Saturation (mm) on Mar 15, 1986, 12 am

Figure C2. Depth to saturation during high flow event of 1985/86 water year

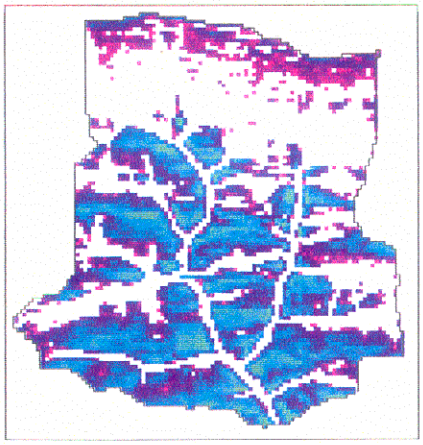

Reference Depth to Saturation

average depth = 266 mm

maximum depth = 585 mm

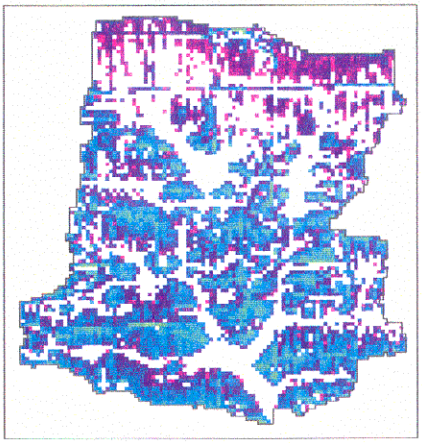

USGS Depth to Saturation

average depth = 288 mm

maximum depth = 674 mm

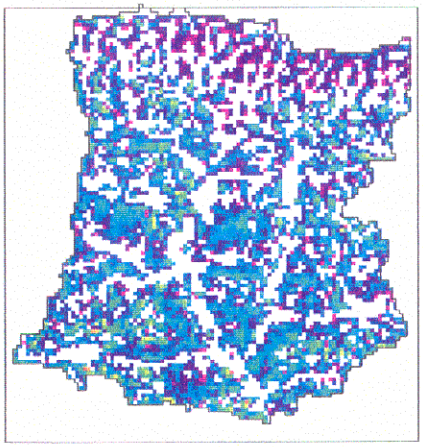

SIR-C Depth to Saturation

average depth = 331 mm

maximum depth = 951 mm

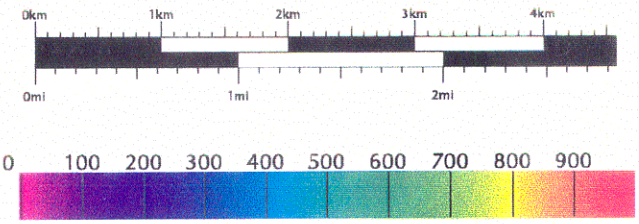

Depth to Saturation (mm) on Sep 14, 1987, 12 am

Figure C3. Depth to saturation during high flow event of 1986/87 water year

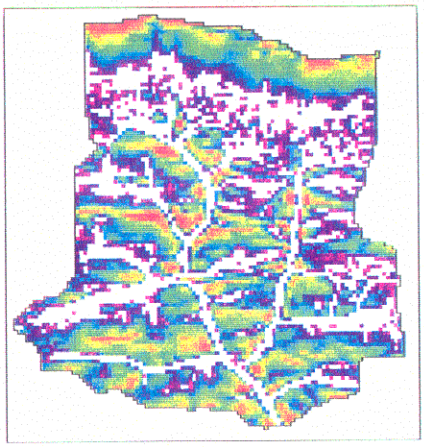

Reference Depth to Saturation

average depth = 447 mm

maximum depth = 984 mm

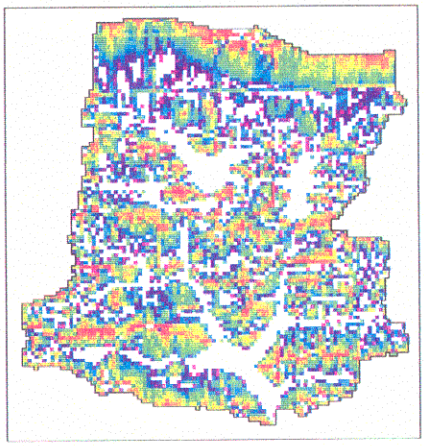

USGS Depth to Saturation

average depth = 538 mm

maximum depth = 999 mm

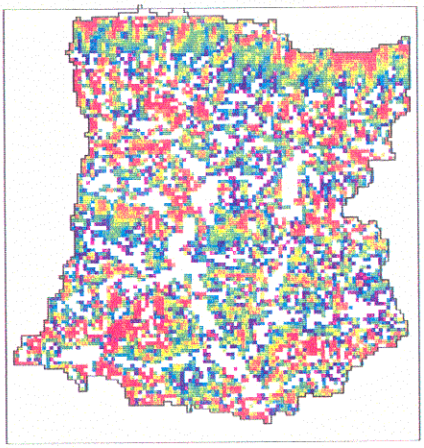

SIR-C Depth to Saturation

average depth = 628 mm

maximum depth = 1000 mm

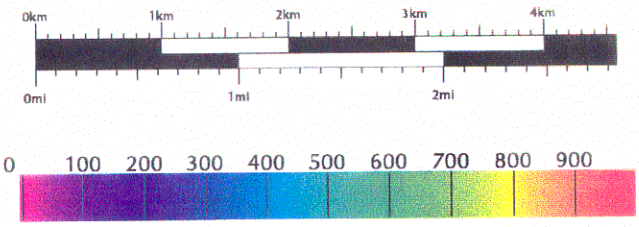

Depth to Saturation (mm) on Jul 26, 1984, 12 am

Figure C4. **Depth to saturation during low flow event of 1983/84 water year**

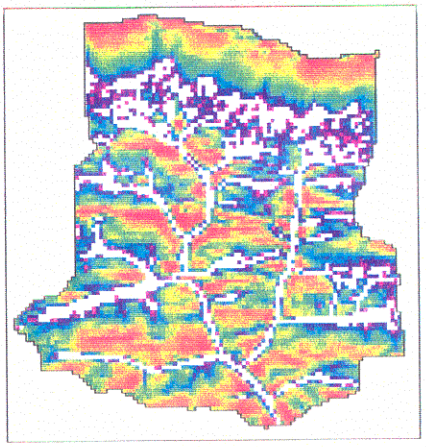

Reference Depth to Saturation

average depth = 597 mm

maximum depth = 192 mm

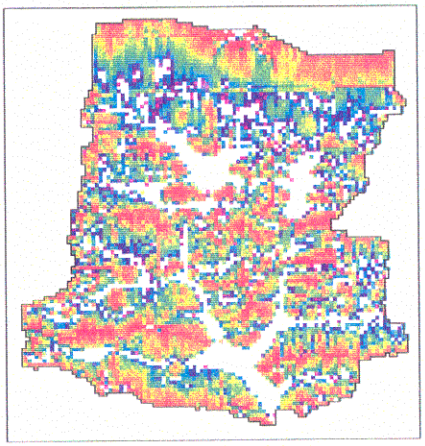

USGS Depth to Saturation

average depth = 664 mm

maximum depth = 999 mm

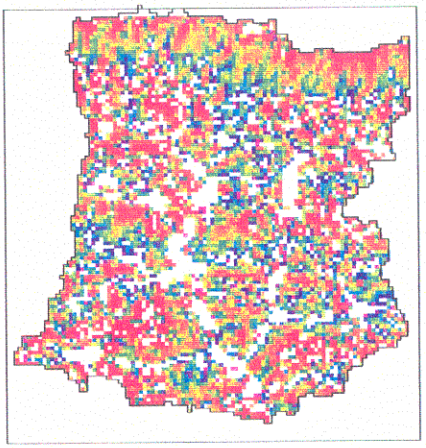

SIR-C Depth to Saturation

average depth = 725 mm

maximum depth = 1000 mm

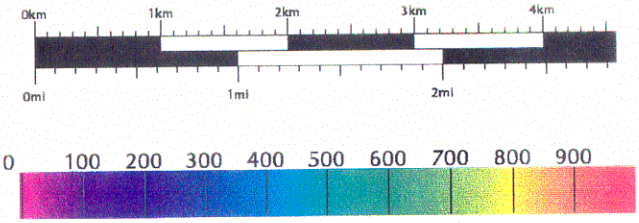

Depth to Saturation (mm) on Aug 30, 1985, 12 am

Figure C5. Depth to saturation during low flow event of 1984/85 water year

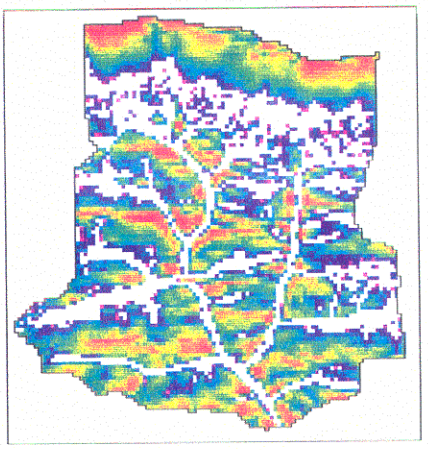

Reference Depth to Saturation

average depth = 549 mm

maximum depth = 988 mm

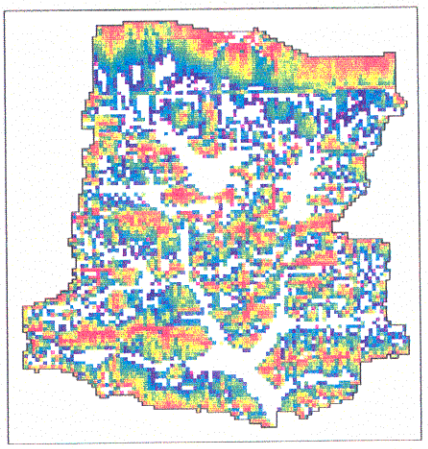

USGS Depth to Saturation

average depth = 615 mm

maximum depth = 999 mm

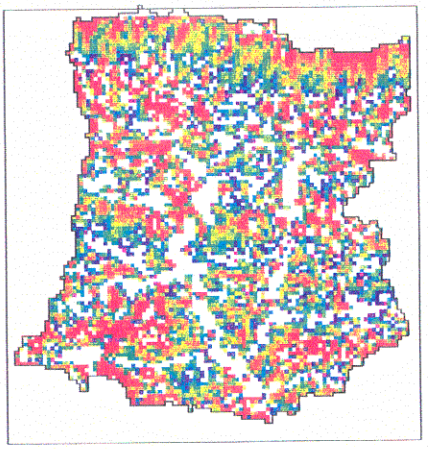

SIR-C Depth to Saturation

average depth = 697 mm

maximum depth = 999 mm

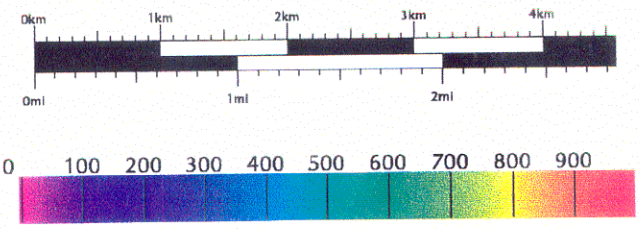

Depth to Saturation (mm) on Jan 15, 1986, 12 am

Figure C6. Depth to saturation during low flow event of 1985/86 water year

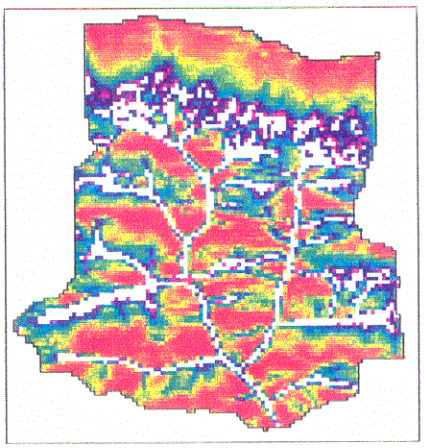

Reference Depth to Saturation

average depth = 672 mm

maximum depth = 997 mm

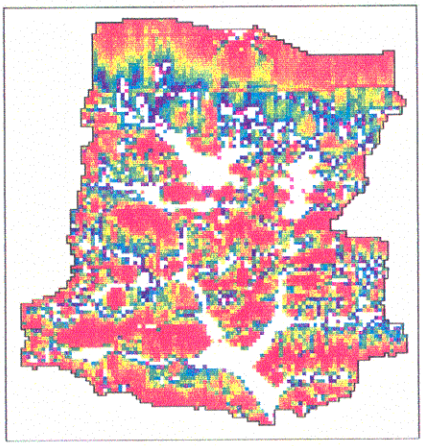

USGS Depth to Saturation

average depth = 741 mm

maximum depth = 999 mm

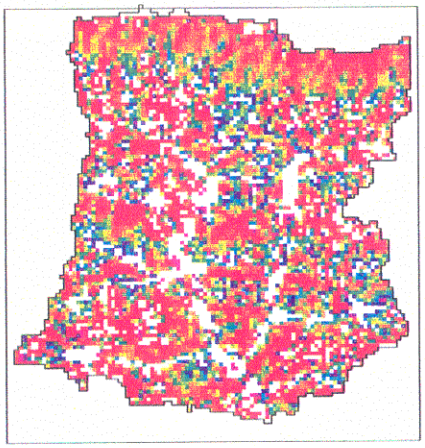

SIR-C Depth to Saturation

average depth = 789 mm

maximum depth = 254 mm

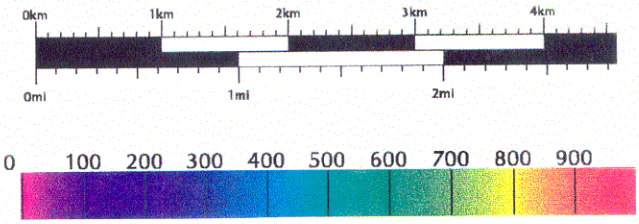

Depth to Saturation (mm) on Aug 5, 1987, 12 am

Figure C7. **Depth to saturation during low flow event of 1986/87 water year**

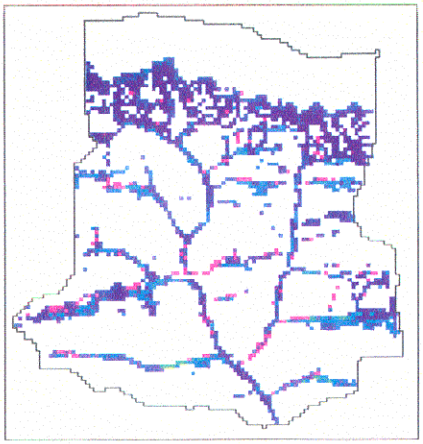

Reference Runoff Production

average runoff depth = 3.2 mm

maximum runoff depth = 8.0 mm

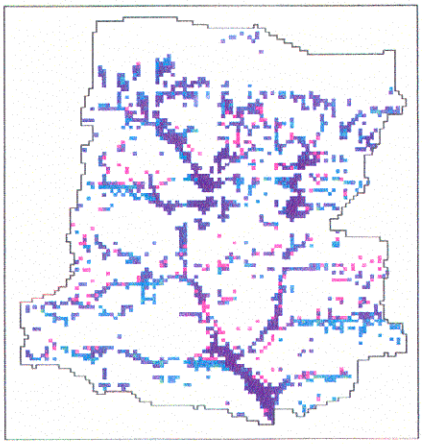

USGS Runoff Production

average runoff depth = 3.2 mm

maximum runoff depth = 8.0 mm

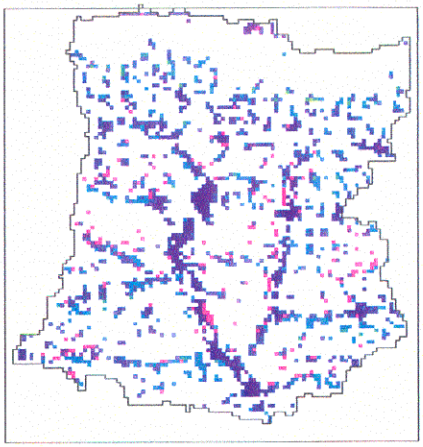

SIR-C Runoff Production

average runoff depth = 3.2 mm

maximum runoff depth = 9.0 mm

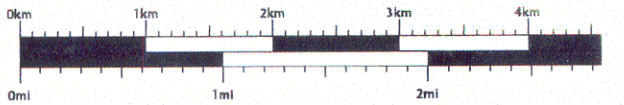

Runoff Production (mm) on Feb 13, 1985, 3 pm

Figure C9. Runoff production during high flow event of 1984/85 water year

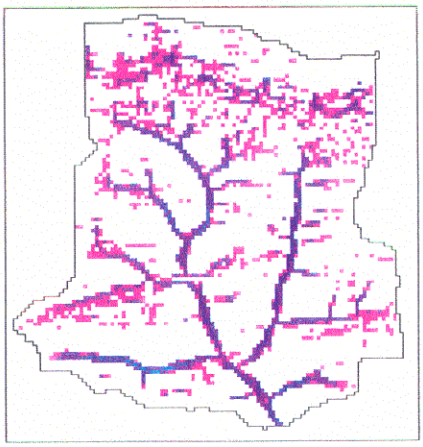

Reference Runoff Production

average runoff depth = 0.7 mm

maximum runoff depth = 6.0 mm

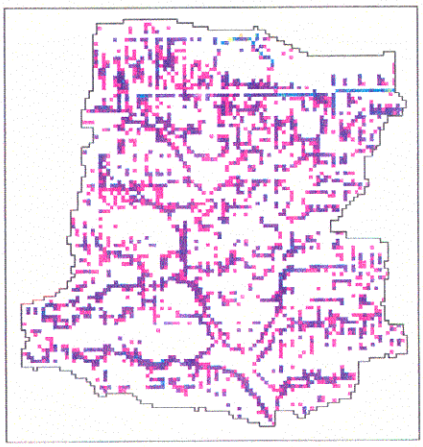

USGS Runoff Production

average runoff depth = 0.9 mm

maximum runoff depth = 11.0 mm

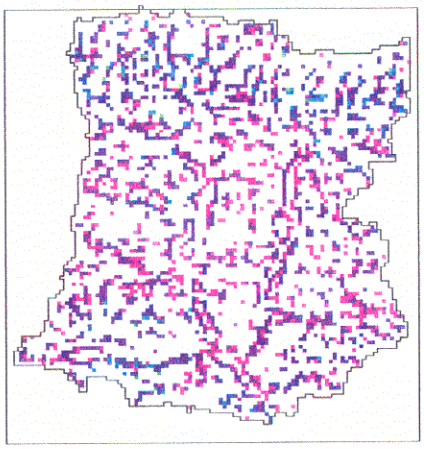

SIR-C Runoff Production

average runoff depth = 1.3 mm

maximum runoff depth = 9.0 mm

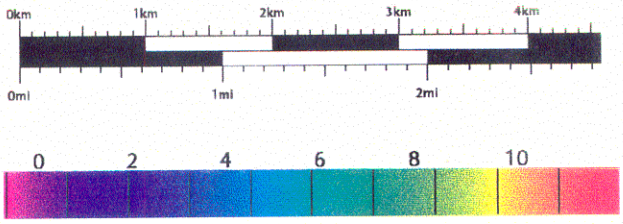

Runoff Production (mm) on Mar 15, 1986, 12 am

Figure C10. Runoff production during high flow event of 1985/86 water year

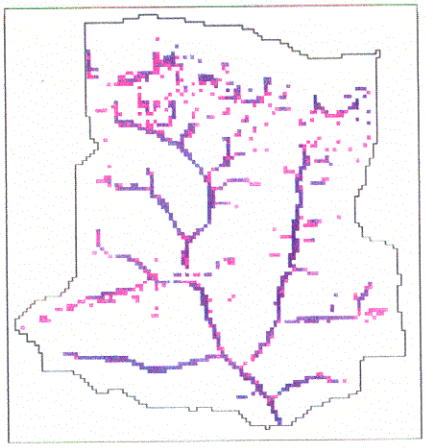

Reference Runoff Production

average runoff depth = 0.9 mm

maximum runoff depth = 4.0 mm

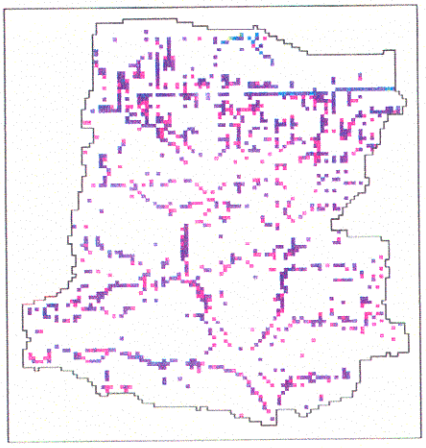

USGS Runoff Production

average runoff depth = 1.1 mm

maximum runoff depth = 9.0 mm

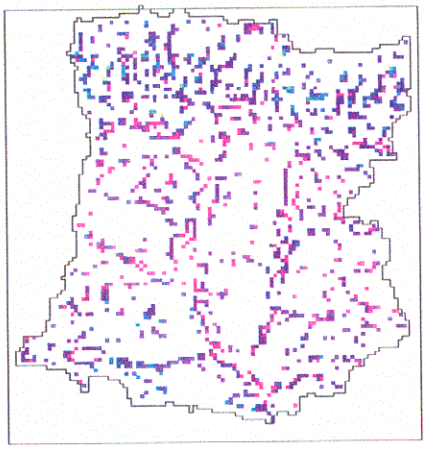

SIR-C Runoff Production

average runoff depth = 1.6 mm

maximum runoff depth = 10.0 mm

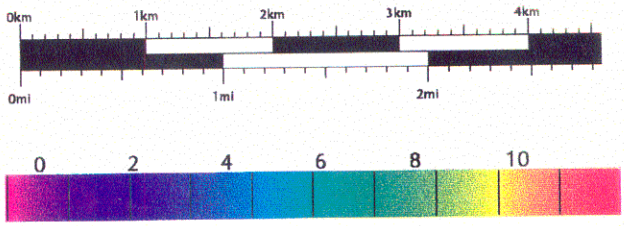

Runoff Production (mm) on Sep 14, 1987, 12 am

Figure C11. Runoff production during high flow event of 1986/87 water year

Appendix D DHSVM Time Series Predictions of Runoff

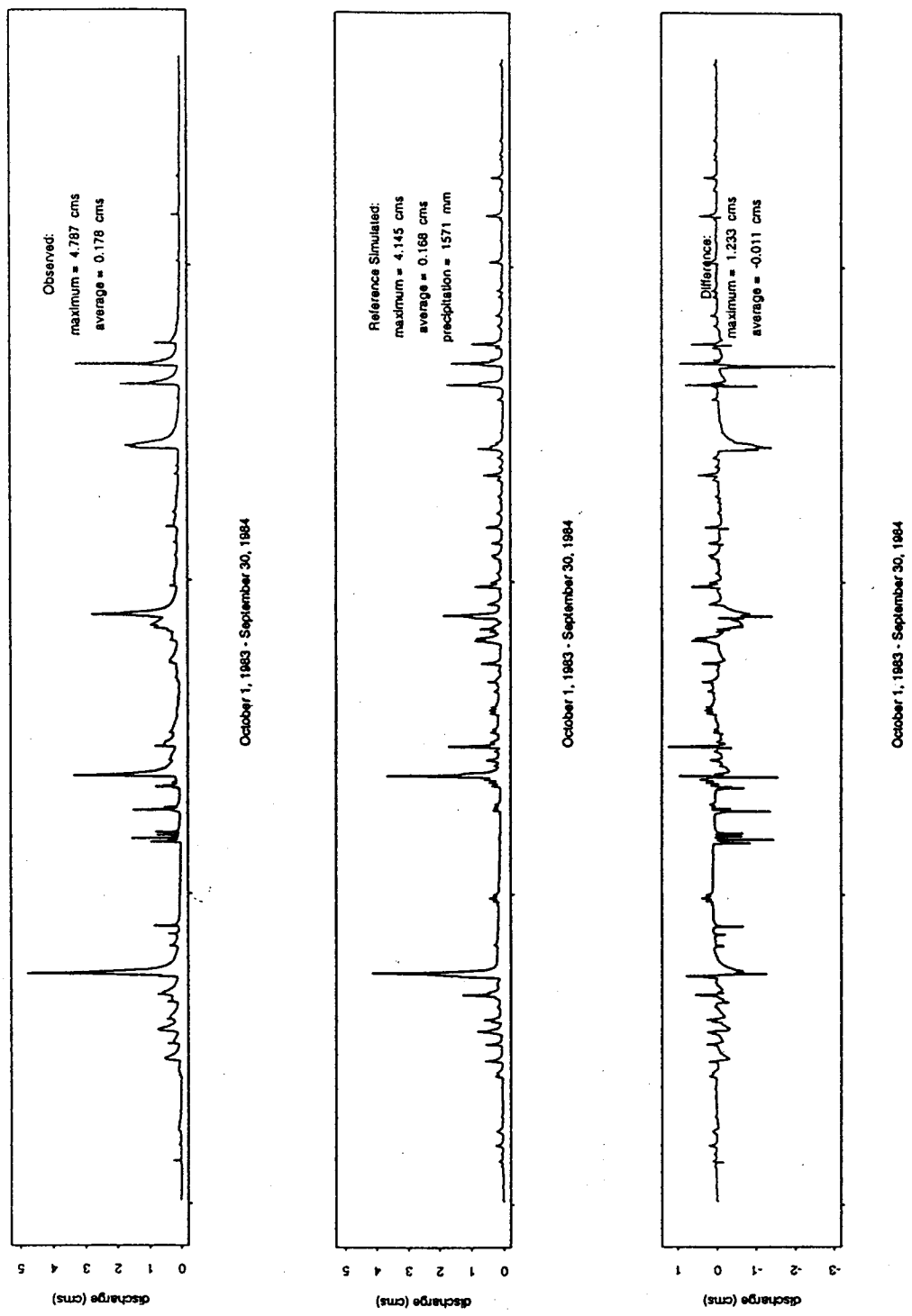

Figure D1. Calibration differences, 1983/84 water year

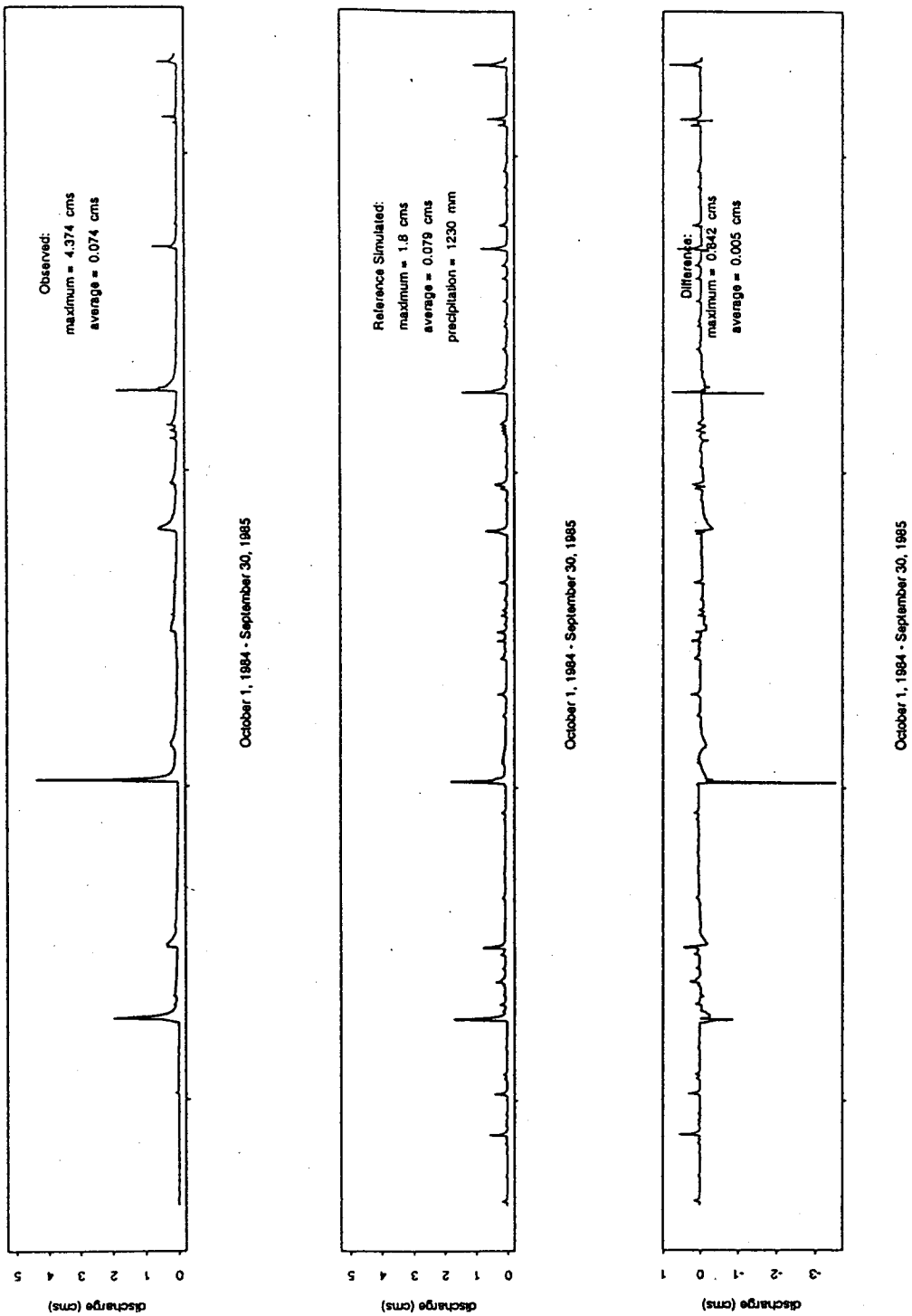

Figure D2. Calibration differences, 1984/85 water year

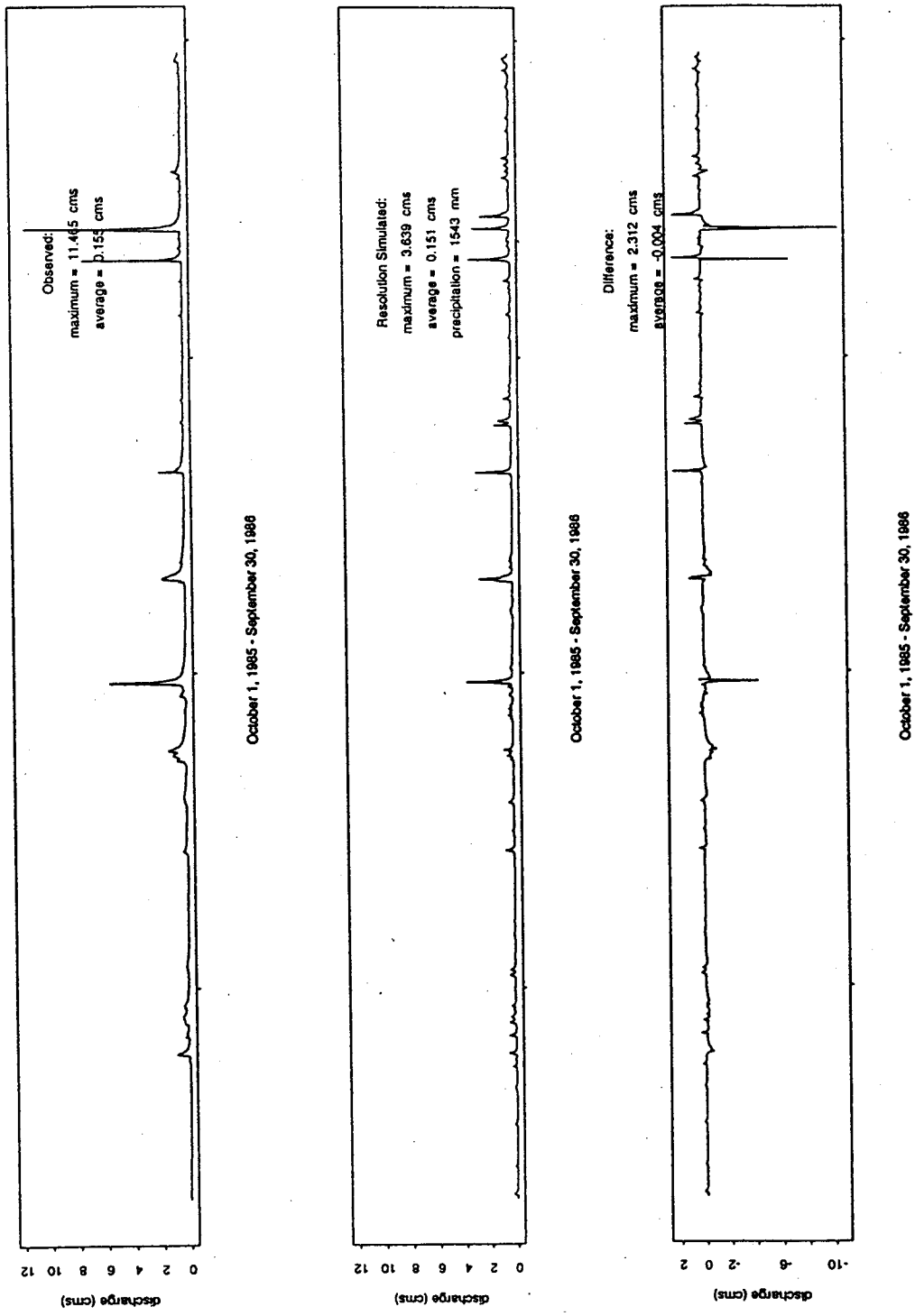

Figure D3. Calibration differences, 1985/86 water year

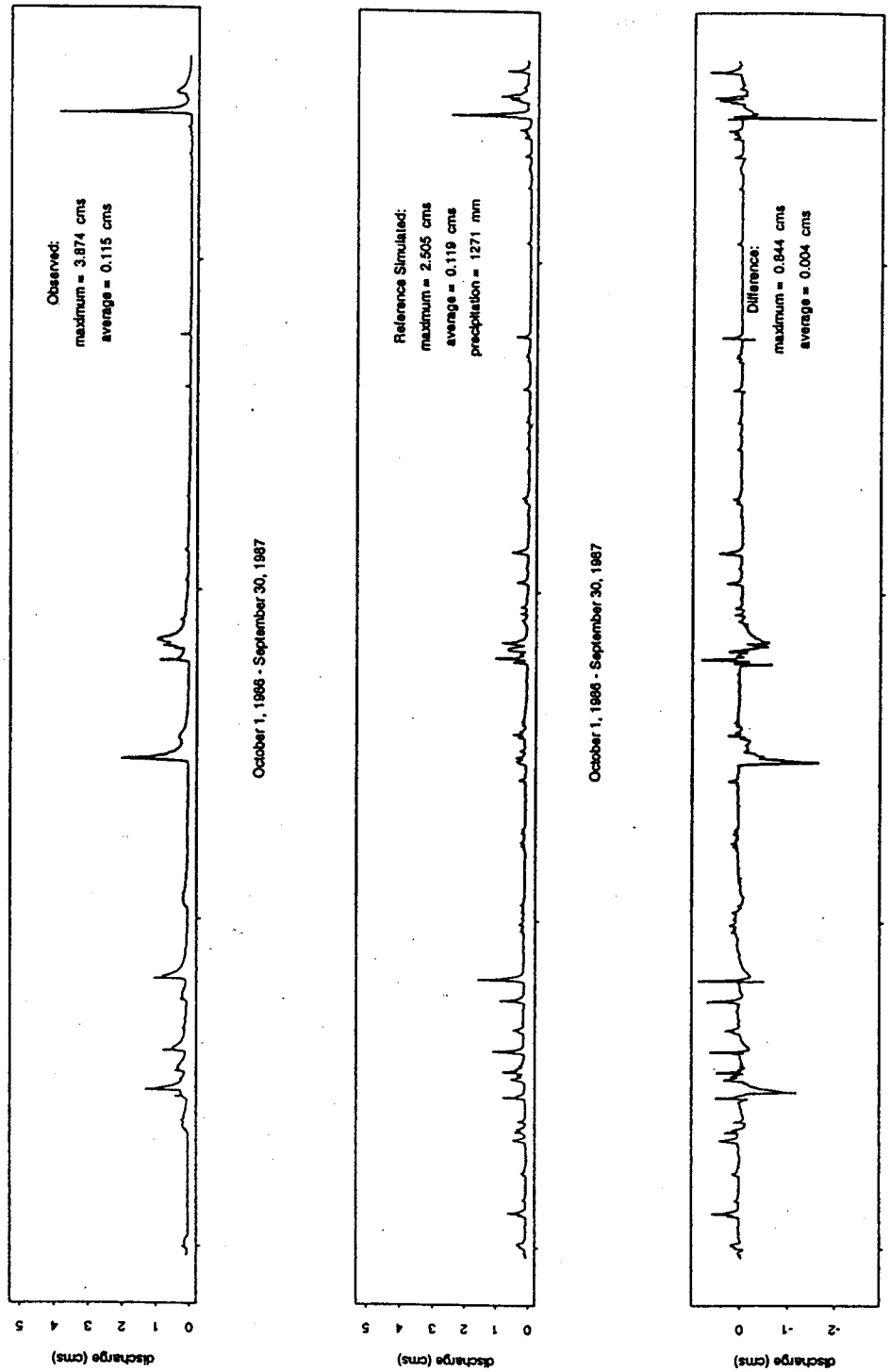

Figure D4. Calibration differences, 1986/87 water year

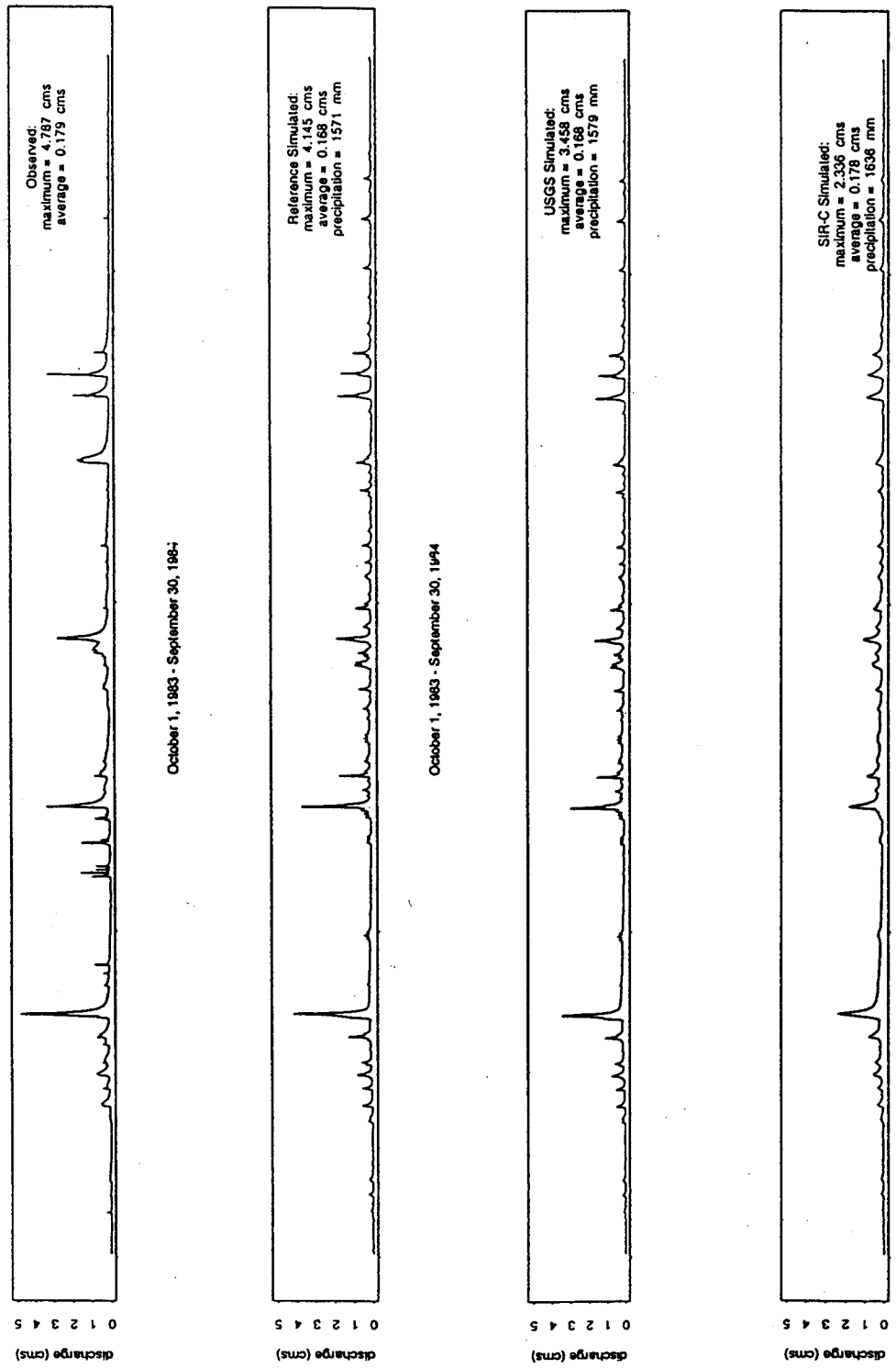

Figure D5. Predicted Runoff, 1983/84 water year

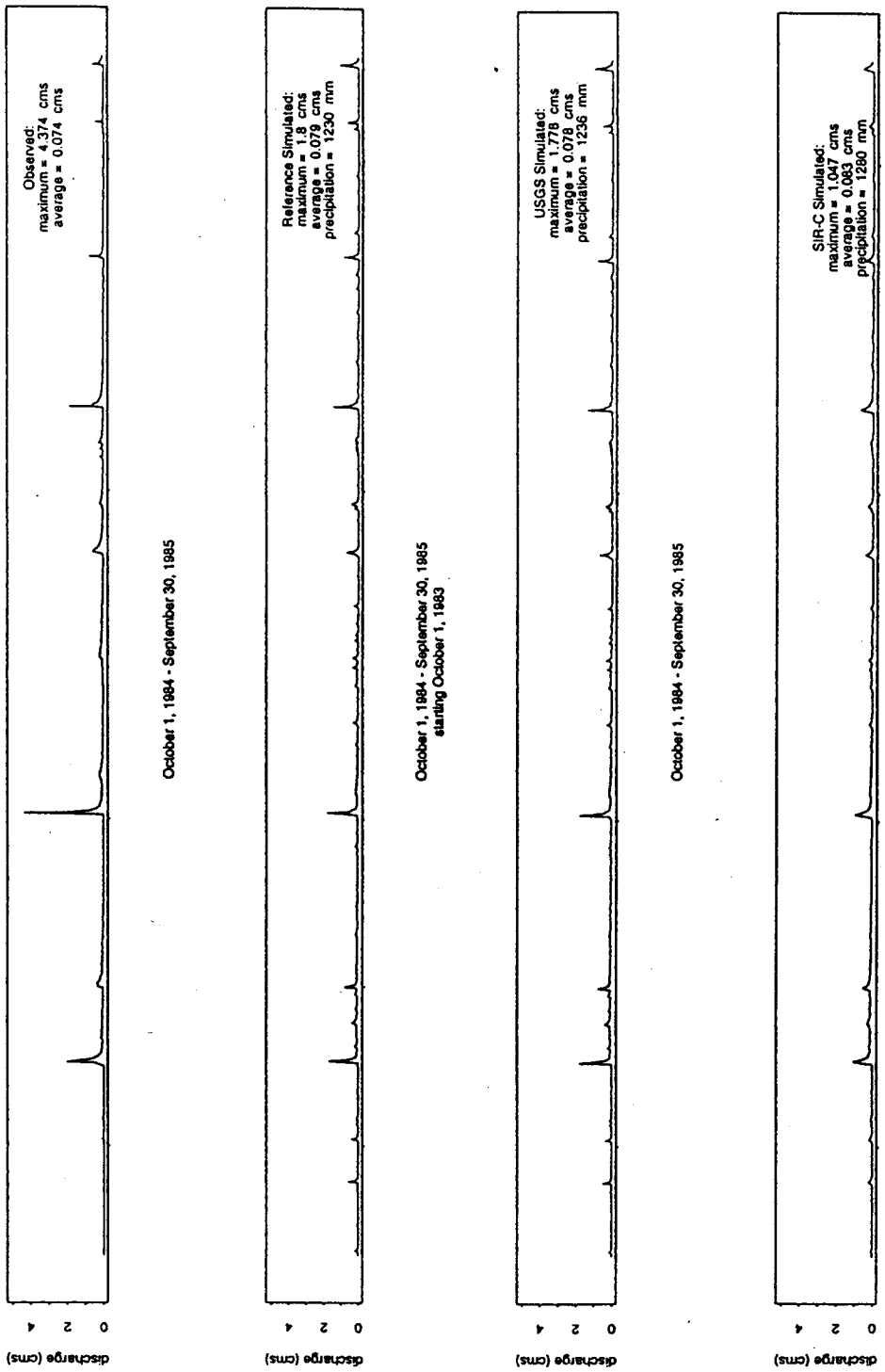

Figure D6. Predicted Runoff, 1984/85 water year

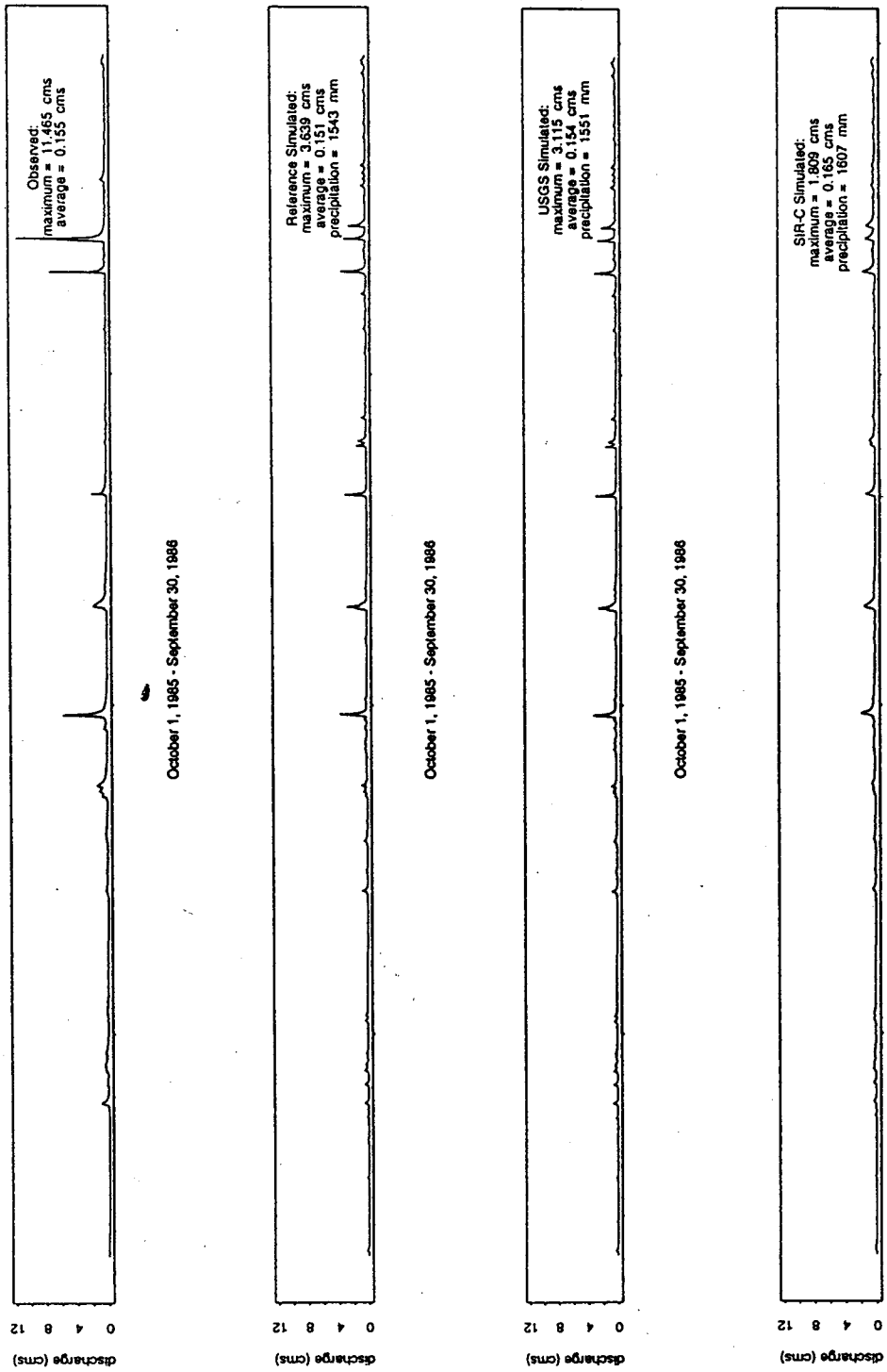

Figure D7. Predicted Runoff, 1985/86 water year

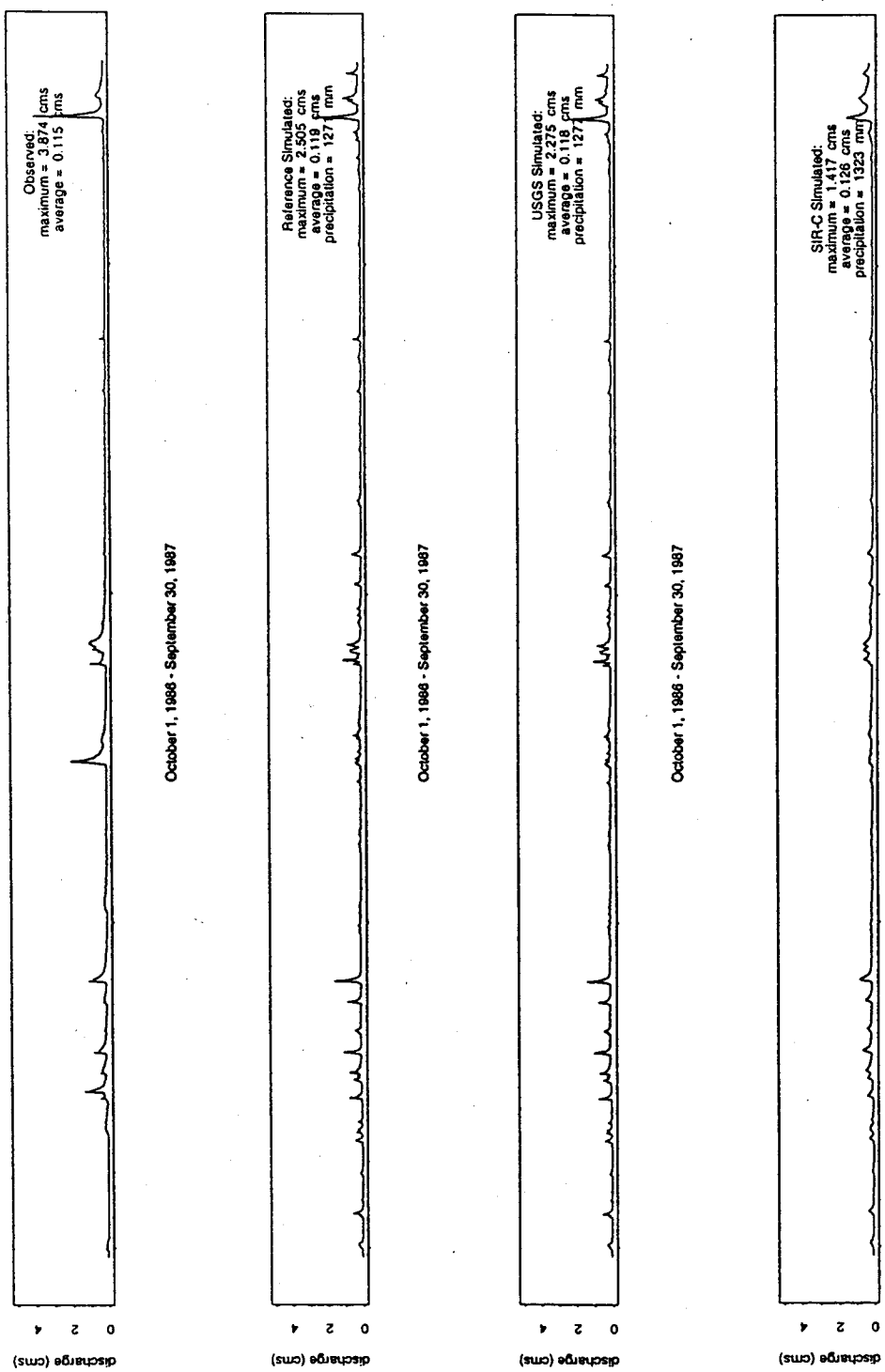

Figure D8. Predicted Runoff, 1986/87 water year